



8-2018

Synthesis, Characterization, and Device Applications of Two-Dimensional Materials

Ali Mohsin

University of Tennessee, amohsin1@vols.utk.edu

Recommended Citation

Mohsin, Ali, "Synthesis, Characterization, and Device Applications of Two-Dimensional Materials. " PhD diss., University of Tennessee, 2018.

https://trace.tennessee.edu/utk_graddiss/5050

This Dissertation is brought to you for free and open access by the Graduate School at Trace: Tennessee Research and Creative Exchange. It has been accepted for inclusion in Doctoral Dissertations by an authorized administrator of Trace: Tennessee Research and Creative Exchange. For more information, please contact trace@utk.edu.

To the Graduate Council:

I am submitting herewith a dissertation written by Ali Mohsin entitled "Synthesis, Characterization, and Device Applications of Two-Dimensional Materials." I have examined the final electronic copy of this dissertation for form and content and recommend that it be accepted in partial fulfillment of the requirements for the degree of Doctor of Philosophy, with a major in Electrical Engineering.

Gong Gu, Major Professor

We have read this dissertation and recommend its acceptance:

Gerd J. Duscher, Aly E. Fathy, Garrett S. Rose

Accepted for the Council:

Dixie L. Thompson

Vice Provost and Dean of the Graduate School

(Original signatures are on file with official student records.)

Synthesis, Characterization, and Device Applications of Two-Dimensional Materials

A Dissertation Presented for the
Doctor of Philosophy
Degree
The University of Tennessee, Knoxville

Ali Mohsin
August 2018

DEDICATION

This dissertation is dedicated to my parents, Sheikh Akhtar Hussain and Almas Akhtar, my wife, Ammara Akhtar, my brother and sister, Ali Naqi and Madiha Naseem for their endless love and support.

ACKNOWLEDGEMENTS

I am deeply thankful to my advisor, Prof. Gong Gu for giving me an opportunity to do an experimental research in the exciting field of two-dimensional materials. His expertise in the device research and experimental nanoscience has added a lot to my academic experience, to which I am deeply grateful. I am especially thankful to him not only for his constant support and encouragement but also for his critical comments and pointing out the fine details that had an important influence on my overall research experience. I would also like to especially thank Profs. Aly Fathy, Garrett S. Rose and Gerd Duscher for agreeing to serve on my Ph.D. thesis defense committee.

I am also grateful to my collaborators from whom I learned a lot about specific techniques. Specifically, I would like to thank our electron microscopy collaborators i.e. Dr. Peizhi Liu, Dr. Guoliang Li, Nicholas Cross and Prof. Gerd Duscher for doing excellent electron microscopy on some of the samples that I prepared. Also, I am grateful to Dr. Lifeng Wang for doing HRTEM and EELS studies on some of my samples. I would like to thank Dr. Xin Zhang for agreeing to do STM study on some of my samples as well. I would like to thank our LEEM/LEED collaborators as well, i.e. Dr. David A Siegel, Dr. Kevin F. McCarty, Dr. Patrick Mende, Prof. Randall Feenstra, and Dr. Alexei Zakharov for doing LEEM/LEED studies on some of my samples. Also, I would also like to thank Dr. Ilia Ivanov for training me on Raman spectroscopy system. Also, I am grateful to Dr. Ivan Kravchenko for training me on cleanroom device fabrication. I would like to thank Dr. John Dunlap and Mr. Greg Jones on training me on the electron microscopes.

I am also grateful to Dr. Lei Liu from whom I learned a lot about the chemical vapor deposition during the early days of my research. Also, I would like to thank my colleagues Dr. Wan Deng for doing AFM and Raman on my samples, and Vineet Khullar for training me on the aligned transfer set up in Dr. Gu's lab. I would also like to acknowledge my recent colleagues Dr. Jing Li and Dr. Hao Wang, with whom I enjoyed discussions about solving problems, related to other projects in Dr. Gu's lab.

In the end, I would like to thank my entire family for their constant support and encouragement.

ABSTRACT

Two-dimensional (2D) materials have attracted tremendous research interest, as they offer novel physics, facile visualization by electron and scanning probe microscopy, and the potential to become next-generation electronic materials, all due to reduced dimensionality. Large-area 2D single crystals are needed for both fundamental scientific experiments and electronic device applications. New methods need to be developed to exploit state-of-the-art microscopy in the scientific investigation of 2D materials. Mechanisms behind the behavior of 2D-material based devices need to be resolved and new device concepts and applications need to be explored. This dissertation addresses these three aspects of 2D materials research.

Using chemical vapor deposition growth of graphene on copper as a platform, the first part of my research in this thesis demonstrates a facile method involving a simple in-situ treatment of the copper catalytic substrate right before the growth that results in mm-sized graphene single crystals, elucidating the key factors of achieving large-area 2D single crystals.

The second part of this work developed experimental methods to resolve important issues in 2D materials research by employing modern transmission electron microscopy. Here, a method has been developed to determine the edge orientation and termination without imaging the edge down to the atomic scale of monolayer hexagonal boron nitride (h-BN), enabling a direct comparison to theoretical predictions. Another important issue in 2D materials research is the determination of the layer count and its lateral spatial uniformity. In this work, a method is developed to map the layer count of a 2D material at nanometer-scale lateral resolution over

extended areas, utilizing a combination of mass-thickness mapping offered by STEM and element-specific quantization afforded by electron energy loss spectrum (EELS) mapping.

The last part of this thesis work unravels the multiple mechanisms behind the behavior of field effect transistors (FETs) based on PdSe₂. The change in device behavior in early reports from ambipolar to n channel was puzzling. As commonly encountered in device research, many factors, including channel material properties, defects, contaminants, and contact effects, are almost always entangled. Here, I use multiple control devices to unravel various mechanisms and provide consistent explanations for device behavior variations.

TABLE OF CONTENTS

| | |
|--|----|
| CHAPTER 1. INTRODUCTION | 1 |
| 1.1 Brief history of two-dimensional materials..... | 2 |
| 1.2 Graphene | 3 |
| 1.3 Hexagonal boron nitride | 5 |
| 1.4 Research motivation and goals | 8 |
| 1.5 Outline of the dissertation | 10 |
| 1.6 References | 11 |
| CHAPTER 2. SURVEY OF THE EXPERIMENTAL TECHNIQUES..... | 16 |
| 2.1 Material synthesis..... | 17 |
| 2.1.1 Chemical vapor deposition..... | 17 |
| 2.2 Characterization techniques | 22 |
| 2.2.1 Scanning electron microscope | 22 |
| 2.2.2 Atomic force microscopy | 25 |
| 2.2.3 Transmission electron microscope | 28 |
| 2.2.4 Z-Contrast scanning transmission electron microscope | 30 |
| 2.2.5 Raman spectroscopy | 35 |

| | |
|---|----|
| 2.3 References | 45 |
| CHAPTER 3. SYNTHESIS OF MILLIMETER-SIZE HEXAGON-SHAPED GRAPHENE | |
| SINGLE CRYSTALS ON RESOLIDIFIED COPPER | 48 |
| 3.1 Abstract | 49 |
| 3.2 Introduction | 50 |
| 3.3 Results and discussion..... | 52 |
| 3.4 Conclusion | 71 |
| 3.5 Experimental methods | 72 |
| 3.5.1 Graphene synthesis | 72 |
| 3.5.2 Characterization | 73 |
| 3.6 References | 74 |
| CHAPTER 4. EXPERIMENTALLY DETERMINED EDGE ORIENTATION OF | |
| TRIANGULAR CRYSTALS OF HEXAGONAL BORON NITRIDE | 79 |
| 4.1 Abstract | 80 |
| 4.2 Introduction | 81 |
| 4.3 Results and discussion..... | 85 |
| 4.4 Conclusion | 93 |
| 4.5 Experimental methods | 93 |

| | |
|--|-----|
| 4.5.1 Growth of triangular h-BN crystals | 93 |
| 4.5.2 Transfer of h-BN crystals on TEM grids | 94 |
| 4.5.3 Microscopy characterization | 95 |
| 4.6 References | 96 |
| CHAPTER 5. MAPPING THE LAYER COUNT OF FEW-LAYER HEXAGONAL BORON | |
| NITRIDE AT HIGH LATERAL SPATIAL RESOLUTIONS | |
| 5.1 Abstract | 103 |
| 5.2 Introduction | 104 |
| 5.3 Results and discussion..... | 107 |
| 5.4 Conclusion | 123 |
| 5.5 Experimental methods | 125 |
| 5.5.1 CVD growth of h-BN films | 125 |
| 5.5.2 Transfer of h-BN films onto TEM grids | 126 |
| 5.5.3 Microscopy and microanalysis | 127 |
| 5.5.4 EELS data analysis | 128 |
| 5.6 References | 129 |
| CHAPTER 6. STUDY OF THE INTRINSIC BEHAVIOR OF PALLADIUM DISELENIDE | |
| FIELD-EFFECT TRANSISTORS | |
| | 134 |

| | |
|---|-----|
| 6.1 Abstract | 135 |
| 6.2 Introduction | 135 |
| 6.3 Results and discussion..... | 137 |
| 6.4 Conclusion | 160 |
| 6.5 Experimental methods | 160 |
| 6.5.1 FET device fabrication and characterization | 160 |
| 6.6 References | 162 |
| CHAPTER 7. SUMMARY AND FUTURE WORK | 167 |
| 7.1 Summary | 168 |
| 7.2 Future work | 169 |
| 7.3 References | 172 |
| VITA | 174 |

LIST OF TABLES

| | |
|---|-----|
| Table 5-1. Layer count statistics | 122 |
| Table 6-1. Summary of the device characteristics..... | 159 |

LIST OF FIGURES

| | |
|---|----|
| Figure 1-1. Graphene lattice in real and reciprocal space. (a) Honeycomb lattice in real space. The dashed rhombus shows the unit cell of hexagonal Bravais lattice consisting of two carbon atoms “A” and “B” (b) Reciprocal space lattice corresponding to the hexagonal Bravais lattice in (a). The solid contour shows the first Brillouin zone, while the crystallographic letters Γ , K , K' and M signify high symmetry points..... | 4 |
| Figure 1-2. Complete bandstructure of graphene in 3D. The energy bands meet at the corners of the first Brillouin zone, i.e., K and K' . Zoom-in of the band structure near the vicinity of corner point K reveals that the energy bands are linear, at low energies. Reprinted with permission from ref. 18. Copyrights 2009 American Physical Society | 6 |
| Figure 1-3. Real space lattice of monolayer h-BN. The two sub-lattices in monolayer h-BN are occupied by alternating boron and nitrogen atoms. Dashed rhombus shows the unit cell of the hexagonal Bravais lattice containing boron and nitrogen atoms | 7 |
| Figure 2-1. Chemical Vapor Deposition. A schematic diagram showing a process of CVD. A carrier gas transports precursor gases or vapor into a reactor, where they diffuse to a substrate. As a result of a chemical reaction that takes place at the surface of the substrate, a thin film of material gets deposited. The by-products are carried away by a carrier gas | 18 |
| Figure 2-2. Photograph of a hot-wall CVD system used for the growth of graphene and h-BN. The reactor is essentially a long quartz tube that is heated externally by a furnace. | 19 |
| Figure 2-3. A photograph showing the downstream end of the CVD furnace. The downstream of the CVD system can be switched between the exhaust or the roughing pump. The liquid nitrogen | |

cold-trap is inserted between the downstream-end and the roughing pump, to prevent any condensation of the vapor inside the pump-oil as well as the backstreaming of pump-oil into the quartz tube.....21

Figure 2-4. Interaction volume in SEM. The electron beam-sample interaction results in the emission of a variety of electrons, from a tear-shaped volume of a specimen, known as interaction volume. Each of these electrons contains valuable information about the sample. Reprinted with permission from ref. 8.....23

Figure 2-5. Operating principle of an AFM. A sharp tip attached to a cantilever scans across a sample surface, while a laser beam is guided to the cantilever head. The reflected laser is intercepted by a four-quadrant photodiode that detects horizontal and vertical deflections of the cantilever, as a result of tip-sample interactions. The feedback loop translates the vertical movement of the cantilever to generate images of surface topography. Reprinted with permission from ref. 14.26

Figure 2-6. An electron column of a typical TEM. A bright and coherent electron beam produced by an electron source is condensed by condenser lenses, to define an illumination area on the sample. Objective lenses are used to focus and magnify an image of the sample that is further magnified by intermediate and projector lenses and is finally displayed on the fluorescent screen. Reproduced with permission from ref. 17..29

Figure 2-7. Two common operating modes of TEM. (a) In a diffraction mode, an intermediate lens is focused onto the diffraction pattern produced by the objective lens in the back-focal plane. (b) In a real-space imaging mode, an intermediate lens is focused onto the real-space image produced by the objective lens in the imaging plane. In both cases, projection lens serves to

further magnify the image produced by the intermediate lens and displays it on the screen.

Reproduced with permission from ref. 1731

Figure 2-8. Diffraction contrast imaging in TEM. (a) In a bright-field imaging mode, an objective aperture is inserted in the imaging plane of an objective lens to block diffracted electron-beams, and only allows directly transmitted beam through the sample for image formation. (b) In a dark-field imaging mode, an objective aperture is inserted to intercept directly transmitted electron-beam, while allowing only one of the diffracted beams for image formation.

Reproduced with permission from ref. 1732

Figure 2-9. Incoherent Rutherford scattering and Z-contrast STEM. (a) A high energy incident electron is scattered by a large angle θ_2 , due to the strong Coulomb attraction force exerted by a nucleus of an isolated atom. (b) In a Z-contrast STEM, electrons that are scattered at large angles by the atoms in the specimen are collected by a large annular detector. These scattered electrons naturally contain elemental Z-contrast. Typical values of β_1 and β_2 are ~ 50 mrad and ~ 200 mrad, respectively. Reproduced with permission from ref. 19.....34

Figure 2-10. Rayleigh vs Raman scattering. In Rayleigh scattering, a molecule excited to a virtual high energy state by an incident photon returns to a ground state, and a scattered photon is released having same energy and wavelength as the incident photon. In a Stokes Raman scattering, an incident photon excites a molecule to a virtual high energy state which later returns to a vibrational lower energy state, by releasing a scattering photon of longer wavelength than the incident photon. In an Anti-Stokes scattering, an incident photon brings a molecule already in a vibrational energy state to a ground state, by releasing a scattered photon having a shorter wavelength than the incident photon. Reprinted with permission from ref. 21.....36

Figure 2-11. Raman spectrum of monolayer graphene. (a) Raman spectrum of pristine (top panel) and defective (bottom panel) monolayer graphene. (b) In-plane and opposite motions of carbon atoms belonging to different sub-lattices are responsible for the G peak in graphene (c) Breathing motion of carbon atoms in the ring is responsible for the observation of D peak. Reprinted with permission from ref. 23. Copyrights 2013 Macmillan Publishers Limited38

Figure 2-12. Raman scattering processes responsible for different peaks in monolayer graphene. Blue arrows represent electron-hole pair generation facilitated by an incident laser photon of a given energy. Red arrows represent electron-hole pair recombination along with a release of resulting photon. Black dashed arrows represent intermediate transitions of electrons or holes facilitated by phonons or defects. (a) First order Raman scattering process for G peak involving phonons with wave vector $\mathbf{q} \approx \mathbf{0}$. (b-g,j,k) Double resonance process responsible for D', D, 2D and D+D'' peaks. (h,i,l) Triple resonance process responsible for 2D', 2D, D+D'' and D+D' peaks. Orange labels indicate the contributions of those processes to the corresponding peaks are small. Pink regions represent filled energy states. Reprinted with permission from ref. 23. Copyrights 2013 Macmillan Publishers Limited40.

Figure 3-1 (a) A simple method to grow millimeter-size graphene single crystals on melted and resolidified copper. (b) Photograph of the synthesized domains. (c) SEM image of an area identified in (b).53

Figure 3-2. Comparison of graphene nucleation density on different copper surfaces. SEM images of (a) thermally annealed solid copper; (b) electro-polished foil; (c) melted and resolidified copper. (d-f) Higher magnification images of the areas identified in (a-c)55

Figure 3-3. Graphene crystallites grown on thermally annealed solid copper over a short time

duration (10 minutes). (a) Graphene domains preferentially nucleate along the surface irregularities, as they follow the pattern of underlying rolling marks on copper surface. Higher magnification images of the dashed (b) and the solid (c) boxes in (a)..56

Figure 3-4. AFM topographical images of various copper surfaces. (a) As-received, (b) Thermally annealed, (c) Electro-polished, and (d) Melted and resolidified. (e) AFM line profiles corresponding to the white dashed lines marked in a-d.....58

Figure 3-5. AFM and tilted SEM images of tungsten foils and re-solidified copper (a, b, c) AFM topographic images of (a) as-received, (b) annealed tungsten foils. And (c) melted and re-solidified copper (d, e) SEM images of (a) as-received and (b) annealed tungsten foil at a tilt angle of 75°.59

Figure 3-6. SEM images of various copper surfaces at a tilt angle of 75°. (a) As-received foil; (b) Thermally annealed solid copper; (c) Electro-polished foil; (d) Melted and resolidified copper. 61

Figure 3-7. Dependence of graphene nucleation density on thermal pretreatment and growth temperature. (a, b) SEM images of graphene on copper foil annealed/melted for 30 min at (a) 1080°C and (b) 1100°C. Growth temperature (1075°C) and growth time (30 min) were kept constant. (c, d) SEM images of the graphene grown at (c) 1050°C and (d) 1075°C. Melting temperature (1100°C) and growth time (30 min) were fixed. Scale bars are 0.2 mm63

Figure 3-8. Dependence of nucleation density on hydrogen partial pressure and the increase in domain size with growth time. (a-c) SEM images of the graphene crystallites synthesized for 90 minutes, under 100 sccm of hydrogen during the first 60 minutes of growth followed 30 minutes of (a) 80 sccm, (b) 90 sccm, and (c) 100 sccm hydrogen flow. (d-e) Graphene domains grown for (d) 100, (e) 200, and (f) 300 minutes, with a constant hydrogen flow rate (100 sccm). Scale bars

| | |
|--|----|
| are 0.2 mm | 65 |
| Figure 3-9. Hexagon with important length parameters identified | 67 |
| Figure 3-10. Raman characterization. (a) Optical image of the graphene crystallite transferred to a 300 nm SiO ₂ /Si substrate. (b) Color-coded stacked Raman spectra corresponding to the spots identified in (a). (c) 2D to G peak intensity ratio (I_{2D}/I_G), (d) FWHM of the 2D peak, (e) Position of the 2D peak, and (f) G to D peak intensity ratio (I_G/I_D) maps of another crystallite..... | 69 |
| Figure 3-11. SAED characterization. (a) SEM image of the graphene domain transferred onto a TEM grid. The edges of the domain are delineated by dashed lines. (b-i) SAED patterns taken in different windows of the TEM grid. | 70 |
| Figure 4-1. STEM images of suspended graphene edges. (a) Overview image showing an edge of a PMMA transferred graphene island. While the PMMA-assisted transfer maintains the integrity of the edge, but the edge itself is covered by contamination. (b) Zoomed-in image of panel a. (c) Overview STEM image showing an edge of a direct transferred graphene island. With direct transferred, although the edges are cleaner, but the structural integrity of the as-grown edge is lost..... | 86 |
| Figure 4-2. CVD grown h-BN crystals. (a) SEM image of equilateral triangle-shaped h-BN crystals on copper. More complicated shapes arise from merged triangles. Purple and brown dashed contours highlight oppositely oriented triangles. (b) Schematic showing two possible edge terminations for zigzag-edged triangular crystals of h-BN. (c) SEM image of the h-BN crystals after transfer onto TEM grid. Red and green dashed triangles highlight a pair of h-BN crystals, which were examined for edge orientations by STEM in Fig. 4-3..... | 88 |

Figure 4-3. Edge orientation determination of triangle-shaped h-BN crystals. (a) Overview STEM image of the red delineated h-BN crystal in Fig. 4-2c. The edges are emphasized by white dashed lines, shifted away from the edges to avoid obscuring. (b) Atomically resolved image acquired in the interior of the h-BN crystal in panel a, overlaid with colored spots representing B and N atoms. (c) Schematic illustration of the edge and bulk orientations of the h-BN crystal in panels a and b. (d) Overview STEM image of the green delineated h-BN crystal in Fig. 4-2c. Similar to panel a the edges are signified by the shifted white dashed lines. (e) Atomically resolved image taken in the 2D bulk of the h-BN crystal in panel d, superimposed with the colored spots representing B and N atoms. (f) Schematic representation of the edge and bulk orientations of the h-BN crystal in panels d and e.....89

Figure 4-4. Edge orientation determination of triangle-shaped h-BN crystals. (a) Overview STEM image of an h-BN crystal. The edges are emphasized by white dashed lines, shifted away from the edges to avoid obscuring. (b) Atomically resolved image acquired in the interior of the h-BN crystal in panel a, overlaid with colored spots representing B and N atoms. (c) Schematic illustration of the edge and bulk orientations of the h-BN crystal in panels a and b. (d) Overview STEM image of another h-BN crystal, which is oppositely oriented to the crystal in panel a. The crystal edges are signified by the shifted white dashed lines. (e) Atomically resolved image taken in the 2D bulk of the h-BN crystal in panel d, superimposed with the colored spots representing B and N atoms. (f) Schematic representation of the edge and bulk orientations of the h-BN crystal in panels d and e.92

Figure 5-1. SEM images of CVD grown h-BN film on copper. (a) Overview SEM image. (b) Zoomed-in image highlighting wrinkles in the h-BN film (blue arrows). (c,d) Further zoomed-in images, showing very dense clusters of adlayers, having sizes of tens of nm (green arrows) and

somewhat isolated triangles with dimensions of few several hundreds of nm (red arrows)108

Figure 5-2. Converting HAADF STEM image to layer count map. (A) Raw HAADF-STEM image of the h-BN film. A hole is identified, and right inset shows a zoomed-in image of the hole. The left inset shows profile along the red line, where vacuum (hole) exhibits non-zero absolute intensity due to dark current. (B) Same image after the subtraction of dark current. Insets show zero intensity in the hole. (C) HAADF STEM image in panel b, after dividing every pixel by the intensity of a single layer of h-BN. Inset is an intensity profile highlighting three regions which are 0, 2 and 1 layer thick. (D) False-color layer count map directly derived from (c) by rounding each pixel value to an integer number of layers. (E) Layer count map derived from (c) by first applying a series of Gaussian filters and then rounding to an integer number of layers109

Figure 5-3. Layer count mapping of the h-BN film based on HAADF imaging in STEM mode. (a) Color-coded layer count map. Areas with significant surface contamination are saturated as white and assigned layer count > 5. Most of the rest of the film exhibits layer counts of 1 or 2. Small adlayers at a length scale of tens of nm are observed (light pink and purple regions with total layer counts of 2 and 3, respectively). Red dashed triangular contour shows an adlayer with lateral dimensions of roughly 200 nm. The small, cluster-like and the big, triangular adlayers are respectively consistent with those observed in SEM images (Fig. 5-1). Black regions represent holes in the film. (b) Bar graph showing frequency of occurrence for pixels values in (a).111

Figure 5-4. Layer count mapping by EELS. (a) Typical EELS and corresponding fitting curves. (b) Layer count map based on EELS analysis in. (c) Histogram of layer count in (b).....114

Figure 5-5. Comparison of layer count distributions determined by HAADF imaging and EELS

mapping. (a) Map of the absolute value of layer count difference between Figs. 5-3a and Figs. 5-4b. (b) Layer count map derived from HAADF imaging in Fig. 5-3a (c) Histogram of layer count discrepancy. A side-by-side comparison of Figs. 5-5(a,b) indicates remarkable agreement between the two techniques, with discrepancies > 1 layers only in contaminated regions117

Figure 5-6. Identifying the contaminated areas. (a) Contaminated areas identified by criterion (1) colored in red, with rest of map in grayscale proportional to mass thickness derived from HAADF imaging. (b) Contaminated areas colored in red, identified by criterion (4) with $t = 1.5$119

Figure 5-7. Layer count mapping and statistics of CVD-grown h-BN excluding contaminated areas. (a) Layer count map of the same region as in Fig. 6-3a with contaminated areas colored coded white (labeled “C” in color code bar), with contaminated areas identified by the criterion (4) with $t = 1.5$. (b) Histogram of (a). (c) Layer count map of the same region with contaminated areas identified by criterion (3). (d) Histogram of (c)..121

Figure 5-8. Layer count maps of an h-BN flake exfoliated from bulk. (a) From HAADF imaging. (b) From EELS mapping. These maps indicate that a 4 layer flake folds onto itself, resulting in the 8-layer region, which is slightly overestimated to be 9 layers by EELS124

Figure 6-1. Type of FET devices studied to understand the origin of ambipolar conduction in PdSe₂ based FET. (a) Fully encapsulated (type 1) device. (b) Type 2 device, which is very similar to the type 1 device except that the top surface of PdSe₂ channel was purposely contaminated during device processing. (c) Ti/Au top-contacted (type 3) device (d) Type 4 device where the contact region between Ti and PdSe₂ is cleaned by successive oxygen plasma, and Ar⁺ ion bombardment, before metal deposition..... 138

Figure 6-2. Fabrication procedure for the fully encapsulated (type 1) device. (a) As-exfoliated FLG flakes on an oxygen plasma cleaned 285 nm SiO₂/Si substrate. (b) As-exfoliated PdSe₂ flakes on an oxygen plasma cleaned 285 nm SiO₂/Si substrate (c) H-BN flake picked up by a PC/PDMS stamp. (d) PC/h-BN/PdSe₂ stack landed onto FLG from Fig. 6-2a. (e) Stack after the removal of PC by solvents. (f) Ti/Au contacts are made to FLG by standard photolithography and metal lift-off procedure. (g) AFM height mapping of the PdSe₂ flake, highlighted by the yellow-boxed region in Fig. 6-2f. (h) Line profile taken across the red line in Fig. 6g. Scale bars are 10 μm in panels a-f, and 5 μm in panel g 141

Figure 6-3. Fabrication procedure for purposely contaminated type 2 device. (a) As-exfoliated FLG flakes on an oxygen plasma treated 285 nm SiO₂/Si substrate. (b) As-exfoliated PdSe₂ flakes on an oxygen plasma cleaned 285 nm SiO₂/Si substrate. (c) A dummy photolithography step is first performed on the PdSe₂ flake in Fig. 6-3b, and then landed on the FLG flakes from Fig. 6-3a, using a PDMS/PC stamp. PdSe₂/FLG stack after PC removal by solvents. (d) As-exfoliated h-BN flake on an oxygen plasma cleaned 285 nm SiO₂/Si substrate. (e) H-BN flake transferred onto the PdSe₂/FLG stack in Fig. 6-3c. (f) Ti/Au contacts are made to the FLG by standard photolithography and metal lift-off procedure. (g) AFM height mapping of the PdSe₂ flake, highlighted by the yellow-boxed region in Fig. 6-3f. (h) Line profile taken across the red line in Fig. 6-3g. Scale bars are 10 μm in panels a-f, and 5 μm in panel g143

Figure 6-4. Fabrication procedure for the type 3 device with Ti/Au as top contacts (a) As-exfoliated PdSe₂ flakes on an oxygen plasma treated 285 nm SiO₂/Si substrate (b) Completed device with Ti/Au as top contacts to the PdSe₂ channel by a standard photolithography and metal lift-off procedure. (c) AFM height mapping of the PdSe₂ flake, highlighted by the yellow-boxed region in Fig. 6-4b. (d) Line profile taken across the red line in Fig. 6-4c. Scale bars are 10 μm in

panels a-b, and 5 μm in panel c 145

Figure 6-5. Fabrication procedure for the type 4 device. (a) As-exfoliated PdSe_2 flakes on an oxygen plasma treated 285 nm SiO_2/Si substrate. (b) The photoresist used as a mask to define contact regions on the PdSe_2 channel. (c) The contact regions of PdSe_2 after cleaning with an oxygen plasma, and an Ar^+ ion bombardment treatment. (d) Final device with Ti/Au as top contacts to the bombarded PdSe_2 region. Scale bars are 10 μm in panels a-d.....146

Figure 6-6. Output characteristics of fully encapsulated type 1 device. (a,b) Linear output curves showing that the device behavior is not limited by the contacts, while the electron-conduction behavior is dominant. (c,d) Output curves remain linear after annealing, while the hole-conduction is suppressed, and the electron-conduction is enhanced...148

Figure 6-7. Output characteristics of type 2 device. (a,b) Hole-dominant conduction with linear output curves indicates that FLG-contacts can inject holes into the p-doped PdSe_2 channel as well (c,d) Output curves remain linear after annealing, while the overall device behavior becomes more ambipolar149

Figure 6-8. Output characteristics of type 3 device with Ti/Au as top contacts. (a,b) Both the hole and electron-conduction are Schottky-limited which is more pronounced for the later. (c,d) Output curves become linear for both hole and electron-conduction after annealing, while the overall device behavior becomes n-type.....151

Figure 6-9. Output characteristics of type 4 device, where the contact regions between Ti and PdSe_2 are cleaned before metal deposition. (a,b) The output curves are linear for both hole and electron injection, while the n-type device behavior is dominant (c,d) After annealing, electron-

conduction is enhanced further, along with a slight increase in hole-conduction as well152

Figure 6-10. Transfer characteristics of the four type of devices before and after annealing at $V_{ds} = 0.1V$ (a) As-fabricated type 1 device show an electron-dominant conduction. Type 2 device show a hole-dominant conduction before annealing. As-fabricated type 3 device show nearly symmetric ambipolar conduction, while type 4 device shows an n-type behavior before annealing. (b) N-type behavior becomes more pronounced for type 1 device after annealing. Type 2 device shows a more symmetric ambipolar conduction after annealing. Both type 3 and type 4 devices exhibit a dominant n-type conduction behavior after annealing153

CHAPTER 1

INTRODUCTION

1.1 Brief history of two-dimensional materials

The research domain of two-dimensional materials (2D) has expanded rapidly since 2004, when the monolayer graphene was first isolated from bulk graphite, under ambient conditions.¹ Before this discovery, the common wisdom was that 2D materials cannot exist in free-standing form thermodynamically, and only serve as a building block for their three-dimensional (3D) counterparts.² Interestingly, monolayer graphene and hexagonal boron nitride (h-BN) have been synthesized and extensively studied on 3D transition metals substrates in ultra-high vacuum environments earlier,³ but those 2D films were never isolated from their parent 3D substrates, under ambient environment. Initial samples of monolayer graphene were prepared by the scotch tape-assisted exfoliation of graphite and then transferring the resulting exfoliated flakes onto silicon-dioxide/silicon (SiO_2/Si) substrates.^{1,4} It is worth mentioning here that the thickness of SiO_2 on Si has also played a crucial role in the first identification of monolayer graphene.⁵ Under visible light illumination, monolayer graphene exhibits a weak interference-like contrast on a SiO_2 film of critical thickness.⁵ This distinction between monolayer graphene and the underlying SiO_2/Si diminishes if the thickness of SiO_2 deviates slightly from the critical values.⁵ The initial samples of exfoliated monolayer graphene exhibited surprisingly higher crystal quality and showed charge carrier mobilities on the orders of several thousand even at ambient temperatures.^{1,4} Graphene is a semi-metal with its charge carriers naturally confined in 2D.^{1,2} The fact that high-quality samples can be prepared even by a simple scotch tap-assisted exfoliation, opened a new avenue to study the interesting physics of 2D electron gas,^{6,7} which was previously restricted to the interfaces of III-V heterostructures only.⁸ This scheme of exfoliation-from-a-layered-3D-compound has been applied to other materials as well, e.g., hexagonal boron nitride (h-BN),⁴ molybdenum disulfide (MoS_2),⁴ Niobium diselenide (NbSe_2),⁴ black phosphorus,⁹ and

more recently to even Antimony.^{10,11} To date, the study of the existence of various materials in 2D form remains a topic of intense theoretical and experimental research.¹² On the experimental side, much progress has been made in the large-scale synthesis of high-quality crystals of 2D materials especially monolayer graphene¹³ and h-BN.¹⁴ This rapid progress in the realm of 2D materials eventually led to a Nobel Prize in 2010.

1.2 Graphene

Graphene is an atomically thin arrangement of carbon atoms in a honeycomb lattice.² It is the symmetry of this lattice which gives rise to some unusual electronic properties that are not encountered in conventional 3D semiconductors.^{15,16} Each carbon atom in graphene is sp^2 hybridized, forming three sigma (σ) bonds with the three nearest-neighbor carbon atoms.^{17,18} The remaining $2p_z$ orbitals on each carbon atom that lie perpendicular to the honeycomb lattice do not take part in sp^2 hybridization and form π bonds.¹⁷ It is the presence of sp^2 hybridization, which gives rise to a planar structure of graphene.¹⁸ Fig. 1-1a shows a honeycomb lattice of graphene, which is in fact composed of two equivalent hexagonal sub-lattices labeled as “A” and “B.”^{15,17} The dashed rhombus in Fig. 1-1a containing two carbon atoms is the unit cell of the honeycomb lattice, with \mathbf{a}_1 and \mathbf{a}_2 as the basis vectors.^{17,18} The C-C bond length in graphene is 1.42\AA which translates to an in-plane lattice constant of 2.46\AA .¹⁸ Fig. 1-1a also shows two high symmetry directions in this lattice, labeled as “zigzag” and “armchair” and separated by an angle of 30° .¹⁸ Fig. 1-1b shows a reciprocal lattice corresponding to the hexagonal Bravais lattice in Fig. 1-1a.^{17,18} The hexagonal contour in Fig. 1-1b shows the first Brillouin zone corresponding to the basis vectors \mathbf{b}_1 and \mathbf{b}_2 .^{17,18} The crystallographic letters Γ , \mathbf{K} , \mathbf{K}' and \mathbf{M} , represent high symmetry points in the Brillouin zone. The two in-equivalent crystallographic points \mathbf{K} and \mathbf{K}' at the corners of the first Brillouin zone have an important significance in determining the

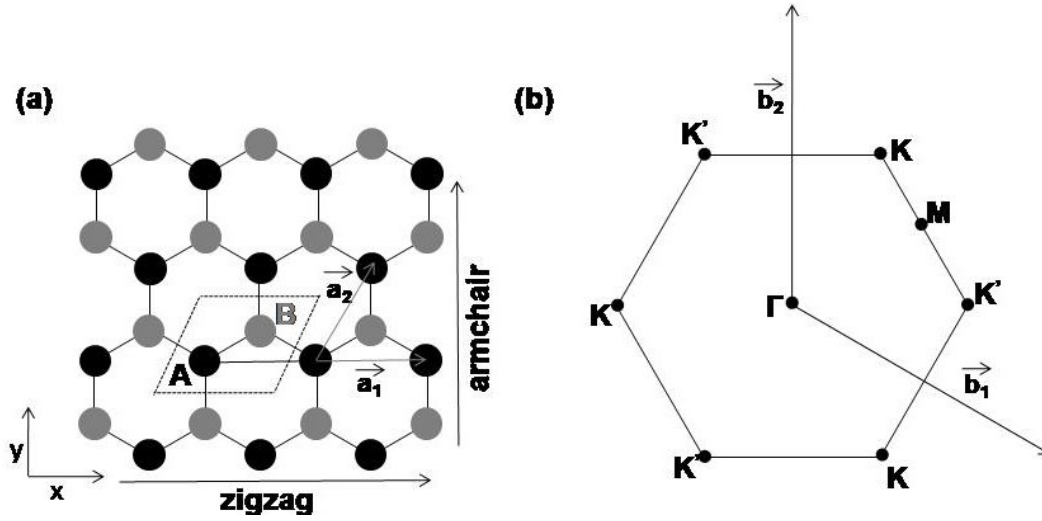


Figure 1-1. Graphene lattice in real and reciprocal space. (a) Honeycomb lattice in real space. The dashed rhombus shows the unit cell of hexagonal Bravais lattice consisting of two carbon atoms “A” and “B” (b) Reciprocal space lattice corresponding to the hexagonal Bravais lattice in (a). The solid contour shows the first Brillouin zone, while the crystallographic letters Γ , K , K' and M signify high symmetry points.

electronic properties of graphene as explained next. Fig. 1-2 shows a complete band structure of graphene in 3D.¹⁸ The right portion of Fig. 1-2 shows the zoom-in of the band structure at one of the corner points **K** of the first Brillouin zone. Clearly, at low energies, the energy bands are linear and meet at the corner point **K**. This unusual behavior implies that graphene is a zero-bandgap semiconductor, and the charge carrier density in graphene can be changed continuously from electrons to holes or vice-versa by an external electric field.^{1,4,6,7,15,16,18} The energy-dispersion relation in the vicinity of the corner points **K** or **K'** can be written as: $\mathbf{E}_{\pm} \approx \pm \hbar v_f \mathbf{q}$ where $v_f = \frac{c}{300}$, c is the speed of light in vacuum, $\mathbf{q} = \mathbf{k} - \mathbf{K}$ is a momentum relative to the corner points, and \mathbf{k} is the crystal momentum in 2D space.^{6,7,15,16,18} In conventional 3D semiconductors, e.g., Si, the energy-dispersion relation resulting from the solution of Schrodinger equation is quadratic.^{15,16,19} It implies that charge carriers behave as having an effective mass “ m_e ” and under the influence of an external force move with an effective velocity “ v ” that is dependent on their effective mass “ m_e ” and crystal momentum “ \mathbf{k} ” as $\mathbf{v} = \frac{\mathbf{k}}{m_e}$. In case of graphene, the remarkable result is the appearance of linear energy-momentum dispersion that entails that the charge carriers in graphene behave effectively as massless-relativistic particles.^{15,16} This is because the linear dispersion results from a Dirac-like Hamiltonian in 2D, and the later is used to describe the behavior of relativistic particles.^{15,16} The corner points **K** and **K'** of the first Brillouin zone, where the energy bands meet are known as *Dirac points*, and linear-energy bands in the vicinity of these points are referred to as *Dirac cones*.¹⁸

1.3 Hexagonal boron nitride

In terms of the structural arrangement of atoms, bulk-h-BN is analogous to graphite in that it is composed of 2D sheets held together by weak van der Waals forces.²⁰ Fig. 1-3 shows the real

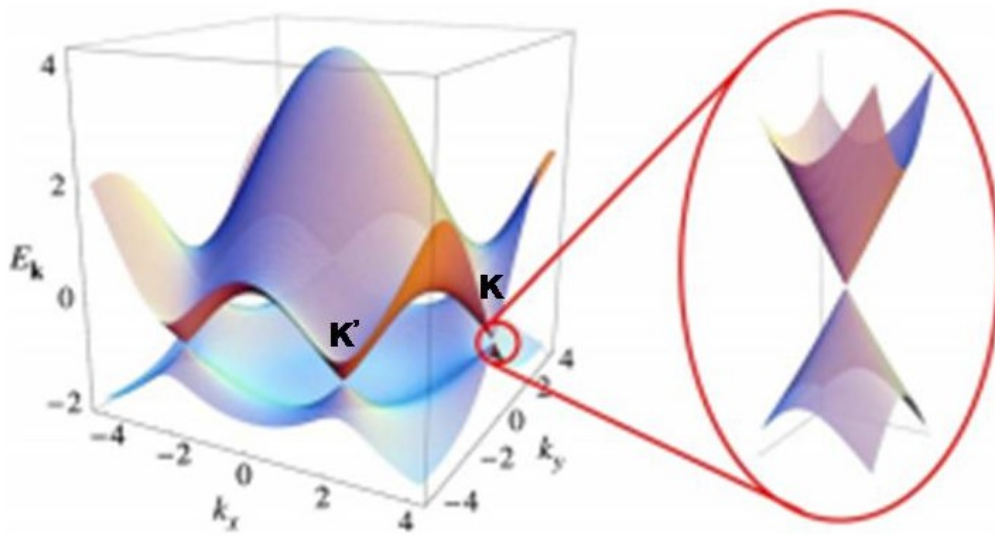


Figure 1-2. Complete bandstructure of graphene in 3D. The energy bands meet at the corners of the first Brillouin zone, i.e., \mathbf{K} and \mathbf{K}' . Zoom-in of the band structure near the vicinity of corner point \mathbf{K} reveals that the energy bands are linear, at low energies. Reprinted with permission from ref. 18. Copyrights 2009 American Physical Society.

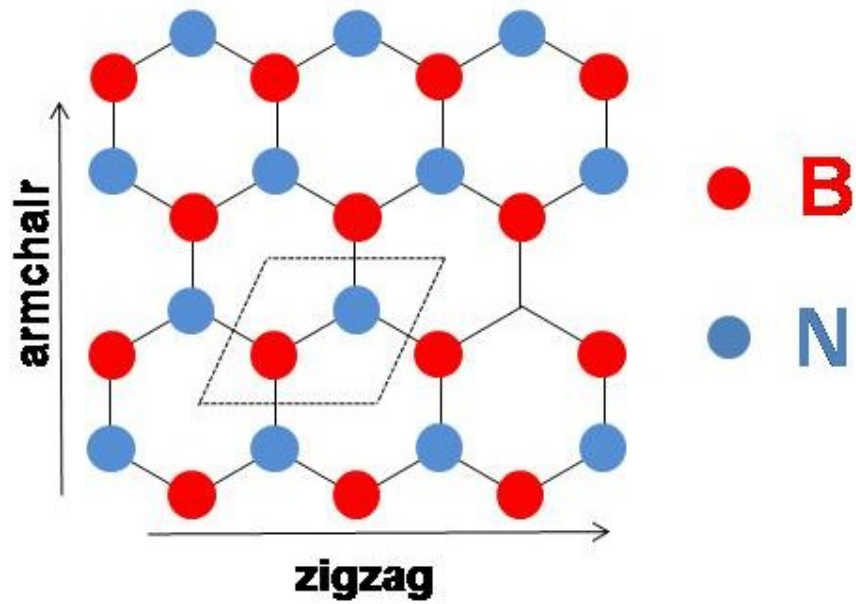


Figure 1-3. Real space lattice of monolayer h-BN. The two sub-lattices in monolayer h-BN are occupied by alternating boron and nitrogen atoms. Dashed rhombus shows the unit cell of the hexagonal Bravais lattice containing boron and nitrogen atoms.

space lattice of a monolayer h-BN. Akin to graphene, monolayer h-BN has a honeycomb lattice, but with an important difference that the two sub-lattices are now non-equivalent, and are occupied by alternating Boron and Nitrogen atoms that gives rise to nonequivalent atomic potentials with the result that monolayer h-BN is an insulator.²¹ Also, due to the presence of two nonequivalent sub-lattices, the top and bottom zigzag edges in the honeycomb lattice shown in Fig. 1-3 are terminated by Boron and Nitrogen atoms. The dashed rhombus in Fig. 1-3 shows a unit cell of monolayer h-BN, containing Boron and a Nitrogen atom. The boron-nitrogen bond length in case of monolayer h-BN is 1.45Å that translates to in an in-plane lattice constant of 2.50 Å, a mismatch of 1.8% relative to graphene.²¹

Due to the insulating behavior and 2D nature of h-BN, thin flakes having thicknesses on the orders of tens of nm serve as an excellent atomically-flat substrates to reduce corrugations and increase charge carrier mobilities of graphene, compared to conventional SiO₂/Si substrates.^{22,23,24} Also, thin flakes of h-BN having thicknesses of 1-2 nm serve as an excellent tunnel dielectric in 2D-to-2D tunneling devices.^{25,26,27}

1.4 Research motivation and goals

As mentioned earlier in the introduction that graphene has some excellent material properties, and in order to bring graphene closer to commercial applications, methods for its growth of the large area, high-quality crystals are highly desirable. Towards that goal, chemical vapor deposition (CVD) is one such method that has recently received much attention for the synthesis of large area, monolayer graphene crystals on copper.^{28,29} In this thesis, a simple method for the CVD growth of mm-sized graphene single crystals will be presented that involves a brief in-situ pretreatment of copper foils.

The hetero-interfaces of crystalline materials is an interesting research ground to search for exotic materials behavior, because sometimes an interesting physics arise, unique to a particular interface.^{30,31} The in-plane interface of zigzag-oriented monolayer graphene and h-BN is predicted to be spin polarized.^{32,33} In order to realize such heterointerfaces with precise edge orientations, it is important to first study the edge orientations of individually grown materials as crystals. In this thesis, an electron microscopy-based method will be presented to study the edge orientations of the CVD-grown, triangular-shaped, monolayer crystals of h-BN.

As mentioned earlier in the introduction, due to its insulating and inherent 2D nature, one of the emerging applications for few-layer h-BN is a tunnel dielectric in 2D-to-2D tunneling devices.^{25,26,27} Such devices require h-BN of uniform thickness. As will be explained later in this thesis, the currently available characterization techniques lack adequate spatial resolutions, to detect non-uniformity in the layer count of CVD-grown 2D material films, at a spatial resolution of hundreds of nm. To overcome this limitation, two complementary and corroborating electron microscopy based techniques will be presented, to map out the layer count of few-layer h-BN films at a spatial resolution of tens of nm.

Apart from graphene, the research field of 2D materials has expanded into the study of other layered materials as well, with most notable being the family of transition metal dichalcogenides.³⁴ While the most well-studied members of this family are MoS₂ and WS₂,³⁴ the other less-studied members of this family are gaining attention as well.³⁵ Recently few-layer palladium diselenide (PdSe₂) has been exfoliated from the bulk flakes.^{36,37} The as-fabricated field-effect transistors (FETs) based on PdSe₂ as a channel showed ambipolar conduction.^{36,37} After low-temperature vacuum annealing, the PdSe₂ FET devices showed predominant n-type conduction,³⁶ but the underlying reason for this shift in the device behavior after annealing is not

known. In this thesis, control FET device studies are conducted to reveal that few-layer PdSe₂ is an intrinsic n-type semiconductor, and the ambipolar device behavior observed in earlier reports^{36,37} was extrinsic, which got introduced unintentionally during device processing.

1.5 Outline of the dissertation

Chapter 2 is dedicated to the survey of the experimental methods and techniques used to undertake the research described in this dissertation. Chapter 3 describes the CVD growth of single crystals of monolayer graphene on the re-solidified copper surface. Chapter 4 details an electron microscopy-based method to deduce edge orientations of triangular-shaped crystals of monolayer h-BN. Chapter 5 is dedicated to the description of two complimentary electron microscopy-based techniques to map-out the layer count of CVD-grown few-layer h-BN at a higher spatial resolution. Chapter 6 explains the fabrication and testing of few-layer PdSe₂ FET devices to reveal the intrinsic n-type nature of as-exfoliated few-layer PdSe₂ flakes. Chapter 7 summarizes the key contributions of this thesis to the research domain of 2D materials.

1.6 References

- (1) Novoselov, K. S.; Morozov, S. V.; Jiang, D.; Zhang, Y.; Dubonos, S. V.; Grigorieva, I. V.; Firsov, A. A.; Geim, A. K. Electric Field Effect in Atomically Thin Carbon Films. *Science* **2004**, *306*, 666–669.
- (2) Geim, A.K.; Novoselov, K. S. The rise of graphene. *Nat. Mater.*, **2007**, *6*, 183-191.
- (3) Oshima, C.; Nagashima, A. Ultra-Thin Epitaxial Films of Graphite and Hexagonal Boron Nitride on Solid Surfaces. *J. Phys. Condense. Matter* **1997**, *9*, 1–20.
- (4) Novoselov, K. S.; Jiang, D.; Schedin, F.; Booth, T. J.; Khotkevich, V. V.; Morozov, S. V.; Geim, A. K. Two-Dimensional Atomic Crystals. *Proc. Natl. Acad. Sci.* **2005**, *102*, 10451–10453.
- (5) Blake, P.; Hill, E. W.; Castro Neto, A. H.; Novoselov, K. S.; Jiang, D.; Yang, R.; Booth, T. J.; Geim, A. K. Making Graphene Visible. *Appl. Phys. Lett.* **2007**, *91*, 063124.
- (6) Novoselov, K. S.; Geim, A. K.; Morozov, S. V.; Jiang, D.; Katsnelson, M. I.; Grigorieva, I. V.; Dubonos, S. V.; Firsov, A. A. Two-Dimensional Gas of Massless Dirac Fermions in Graphene. *Nature* **2005**, *438*, 197–200.
- (7) Zhang, Y.; Tan, Y.-W.; Stormer, H. L.; Kim, P. Experimental Observation of the Quantum Hall Effect and Berry's Phase in Graphene. *Nature* **2005**, *438*, 201–204.
- (8) Prange, R.E.; Girvin, S. M.; Cage, M.E.; Klitzing K.; Chang, A. M.; Duncan, F.; Haldane, M. *The Quantum Hall Effect*; Springer-Verlag: New York, 1990.
- (9) Li, L.; Yu, Y.; Ye, G. J.; Ge, Q.; Ou, X.; Wu, H.; Feng, D.; Chen, X. H.; Zhang, Y. Black

Phosphorus Field-Effect Transistors. *Nat. Nanotech.* **2014**, *9*, 372–377.

(10) Gibaja, C.; Rodriguez-San-Miguel, D.; Ares, P.; Gómez-Herrero, J.; Varela, M.; Gillen, R.; Maultzsch, J.; Hauke, F.; Hirsch, A.; Abellán, G.; *et al.* Few-Layer Antimonene by Liquid-Phase Exfoliation. *Angew. Chem.* **2016**, *55*, 14345–14349.

(11) Ares, P.; Aguilar-Galindo, F.; Rodríguez-San-Miguel, D.; Aldave, D. A.; Díaz-Tendero, S.; Alcamí, M.; Martín, F.; Gómez-Herrero, J.; Zamora, F. Mechanical Isolation of Highly Stable Antimonene under Ambient Conditions. *Adv. Mater.* **2016**, *28*, 6332–6336.

(12) Zhang, Y.; Rubio, A.; Lay, G. Le. Emergent Elemental Two-Dimensional Materials beyond Graphene. *J. Phys. D* **2017**, *50*, 53004.

(13) Yan, Z.; Peng, Z.; Tour, J. M. Chemical Vapor Deposition of Graphene Single Crystals. *Acc. Chem. Res.* **2014**, *47*, 1327–1337.

(14) Wang, H.; Zhao, Y.; Xie, Y.; Ma, X.; Zhang, X. Recent Progress in Synthesis of Two-Dimensional Hexagonal Boron Nitride. *J. Semicond.* **2017**, *38*, 31003.

(15) Novoselov, K. S.; Morozov, S. V.; Mohinddin, T. M. G.; Ponomarenko, L. A.; Elias, D. C.; Yang, R.; Barbolina, I. I.; Blake, P.; Booth, T. J.; Jiang, D.; Giesbers, J.; Hill, E.W.; Geim, A.K. Electronic Properties of Graphene. *Phys. Stat. Sol. (b)* **2007**, *244*, 4106–4111.

(16) Neto, A. C.; Guinea, F.; Peres, N. M. Drawing Conclusions from Graphene. *Phys. World* **2006**, *19*, 33–37.

(17) Wallace, P. R. The Band Theory of Graphite. *Phys. Rev.* **1947**, *71*, 622–634.

- (18) Neto, A. H. C.; Guinea, F.; Peres, N. M. R.; Novoselov, K. S.; Geim, A. K. The Electronic Properties of Graphene. *Rev. Mod. Phys.* **2007**, *81*, 110-155
- (19) Pierret, R. F. *Advanced Semiconductor Fundamentals*, Pearson Education: New Jersey, 2000.
- (20) Giovannetti, G.; Khomyakov, P. A.; Brocks, G.; Kelly, P. J.; Brink, J. Van Den. Substrate-Induced Band Gap in Graphene on Hexagonal Boron Nitride: Ab Initio Density Functional Calculations. *Phys. Rev. B* **2007**, *76*, 073103.
- (21) Rubio, A.; Corkill, J. L.; Cohen, M. L. Theory of Graphitic Boron Nitride Nanotubes. *Phys. Rev. B* **1994**, *49*, 5081–5084.
- (22) Dean, C. R.; Young, A F.; Meric, I.; Lee, C.; Wang, L.; Sorgenfrei, S.; Watanabe, K.; Taniguchi, T.; Kim, P.; Shepard, K. L.; *et al.* Boron Nitride Substrates for High-Quality Graphene Electronics. *Nat. Nanotech.* **2010**, *5*, 722–726.
- (23) Decker, R.; Wang, Y.; Brar, V. W.; Regan, W.; Tsai, H. Z.; Wu, Q.; Gannett, W.; Zettl, A.; Crommie, M. F. Local Electronic Properties of Graphene on a BN Substrate via Scanning Tunneling Microscopy. *Nano Lett.* **2011**, *11*, 2291–2295.
- (24) Xue, J.; Sanchez-Yamagishi, J.; Bulmash, D.; Jacquod, P.; Deshpande, A.; Watanabe, K.; Taniguchi, T.; Jarillo-Herrero, P.; LeRoy, B. J. STM Spectroscopy of Ultra-Flat Graphene on Hexagonal Boron Nitride. *Nat. Mater.* **2011**, *10*, 282–285.
- (25) Feenstra, R. M.; Jena, D.; Gu, G. Single-Particle Tunneling in Doped Graphene-Insulator-Graphene Junctions. *J. Appl. Phys.* **2012**, *111*, 043711.

- (26) Britnell, L.; Gorbachev, R. V.; Geim, A. K.; Ponomarenko, L. A.; Mishchenko, A.; Greenaway, M. T.; Fromhold, T. M.; Novoselov, K. S.; Eaves, L. Resonant Tunnelling and Negative Differential Conductance in Graphene Transistors. *Nat. Comm.* **2013**, *4*, 1794.
- (27) Mishchenko, A.; Tu, J. S.; Cao, Y.; Gorbachev, R. V.; Wallbank, J. R.; Greenaway, M.T.; Moroz J.; Wanatabe, K.; Taniguchi, T.; Vdovin, E.E.; Makarovksy, O.; Fromhold, T.M.; Fal'ko, V.I.; Geim, A.K.; Eaves, L.; Novoselov, K.S. Twist-Controlled Resonant Tunnelling in Graphene/boron Nitride/graphene Heterostructures. *Nat. Nanotech.* **2014**, *9*, 808–813.
- (28) Mattevi, C.; Kim, H.; Chhowalla, M. A Review of Chemical Vapour Deposition of Graphene on Copper. *J. Mater. Chem.* **2011**, *21*, 3324-3334.
- (29) Yan, Z.; Lin, J.; Peng, Z.; Sun, Z.; Zhu, Y.; Li, L.; Xiang, C.; Samuel, E.L.; Kittrell, C.; Tour, J.M. Toward the Synthesis of Wafer-Scale Single-Crystal Graphene on Copper Foils. *ACS Nano* **2012**, *6*, 9110–9117.
- (30) Ohtomo, A.; Hwang, H.Y. A high-mobility electron gas at the $\text{LaAlO}_3/\text{SrTiO}_3$ heterointerface. *Nature* **2004**, *427*, 423-426.
- (31) Reyren, N.; Thiel, S.; Caviglia, A.D.; Kourkoutis, L.F.; Hammerl, G.; Richter, C.; Schneider, C.W.; Kopp, T.; Rüetschi, A.-S.; Jaccard, D.; Gabay, M.; Muller, D.A.; Triscone, J.-M.; Mannhart, J. Superconducting Interfaces between Insulating Oxides. *Science* **2007**, *317*, 1196-1199.
- (32) Pruneda, J.M. Origin of half-semimetallicity induced at interfaces of C-BN heterostructures. *Phys. Rev. B* **2010**, *81*, 161409(R).

- (33) Bhowmick, S.; Singh, A.K.; Yakobson, B.I. Quantum Dots and Nanoroads of Graphene Embedded in Hexagonal Boron Nitride *J. Phys. Chem. C* **2011**, *115*, 9889-9893.
- (34) Wang, Q. H.; Kalantar-Zadeh, K.; Kis, A.; Coleman, J. N.; Strano, M. S. Electronics and Optoelectronics of Two-Dimensional Transition Metal Dichalcogenides. *Nat. Nanotech.* **2012**, *7*, 699–712.
- (35) Gong, C.; Zhang, H.; Wang, W.; Colombo, L.; Wallace, R. M.; Cho, K. Band Alignment of Two-Dimensional Transition Metal Dichalcogenides: Application in Tunnel Field Effect Transistors. *Appl. Phys. Lett.* **2013**, *103*, 053513.
- (36) Chow, W. L.; Yu, P.; Liu, F.; Hong, J.; Wang, X.; Zeng, Q.; Hsu, C. H.; Zhu, C.; Zhou, J.; Wang, X.; Xia, J.; Yan, J.; Chen, Y.; Wu, D. Yu, T.; Shen, Z.; Lin, H.; Jin, C.; Tay, B. K.; Liu, Z. High Mobility 2D Palladium Diselenide Field-Effect Transistors with Tunable Ambipolar Characteristics. *Adv. Mater.* **2017**, *29*, 1–8.
- (37) Oyedele, A. D.; Yang, S.; Liang, L.; Puretzky, A. A.; Wang, K.; Zhang, J.; Yu, P.; Pudasaini, P. R.; Ghosh, A. W.; Liu, Z.; Rouleau, C.M.; Sumpter, B.G.; Chisholm, M. F.; Zhou, W.; Rack, P.D.; Geohegan, D. B.; Xiao, K. PdSe₂: Pentagonal Two-Dimensional Layers with High Air Stability for Electronics. *J. Am. Chem. Soc.* **2017**, *139*, 14090–14097.

CHAPTER 2

SURVEY OF THE EXPERIMENTAL TECHNIQUES

2.1 Material synthesis

2.1.1 Chemical vapor deposition

Chemical vapor deposition (CVD) is a commonly used technique in the semiconductor industry for thin film deposition of semiconductors.¹ In this process, precursors in the form of gases or vapors are transported by a carrier gas to a reaction chamber,¹ as shown in Fig. 2-1. Some fraction of the precursors along with the carrier gas, diffuse to a catalytic substrate which is held at a certain temperature. Based on the designed chemistry of precursors, a chemical reaction takes place at the surface of the substrate, and a thin film of resulting material gets deposited. The by-products of chemical reaction in the vapor phase are carried away by the carrier gas. If the entire reaction chamber is heated externally, e.g., by a furnace, the scheme is known as hot-wall CVD. On the other hand, if only the substrate is heated locally, while the chamber walls are kept at a lower temperature, the process is known as cold-wall CVD. The deposition can be carried out either at atmospheric pressure (APCVD) or low pressure (LPCVD).¹ Sometimes the target substrate for deposition is thermally unstable at higher reaction temperatures involved in the CVD process. In that case, plasma is introduced in the CVD process to help pyrolyze the precursors at lower temperatures. This technique is known as plasma enhanced chemical vapor deposition (PECVD).¹

The CVD furnace used in this study is shown in Fig. 2-2. It is essentially a PECVD a system which in this study was operated in a hot-wall APCVD mode. A 2'' diameter quartz tube serves as a reactor, which is heated externally by the furnace. The copper foils which serve the dual purpose of catalyst, as well as deposition substrates, are usually placed in a quartz boat, at the center of the furnace. The upstream of the furnace is fed by carrier gases, i.e., hydrogen and

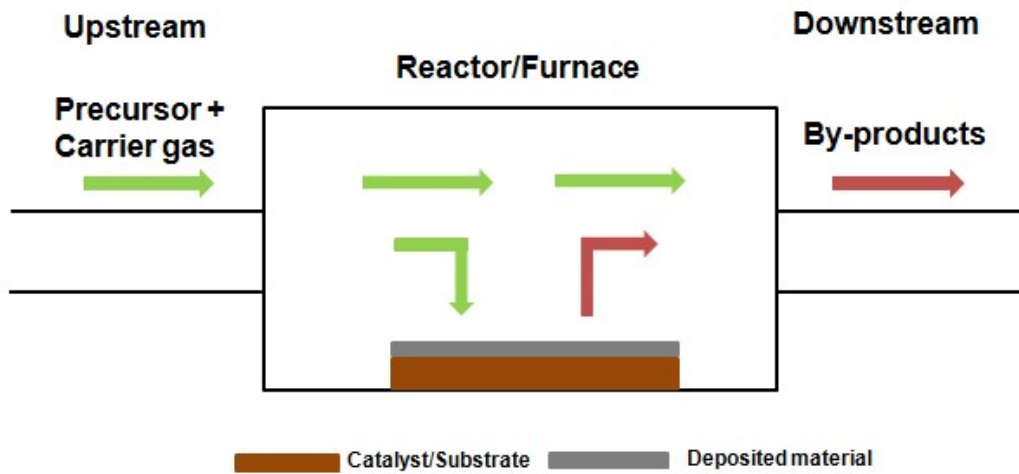


Figure 2-1. Chemical Vapor Deposition. A schematic diagram showing a process of CVD. A carrier gas transports precursor gases or vapor into a reactor, where they diffuse to a substrate. As a result of a chemical reaction that takes place at the surface of the substrate, a thin film of material gets deposited. The by-products are carried away by a carrier gas.

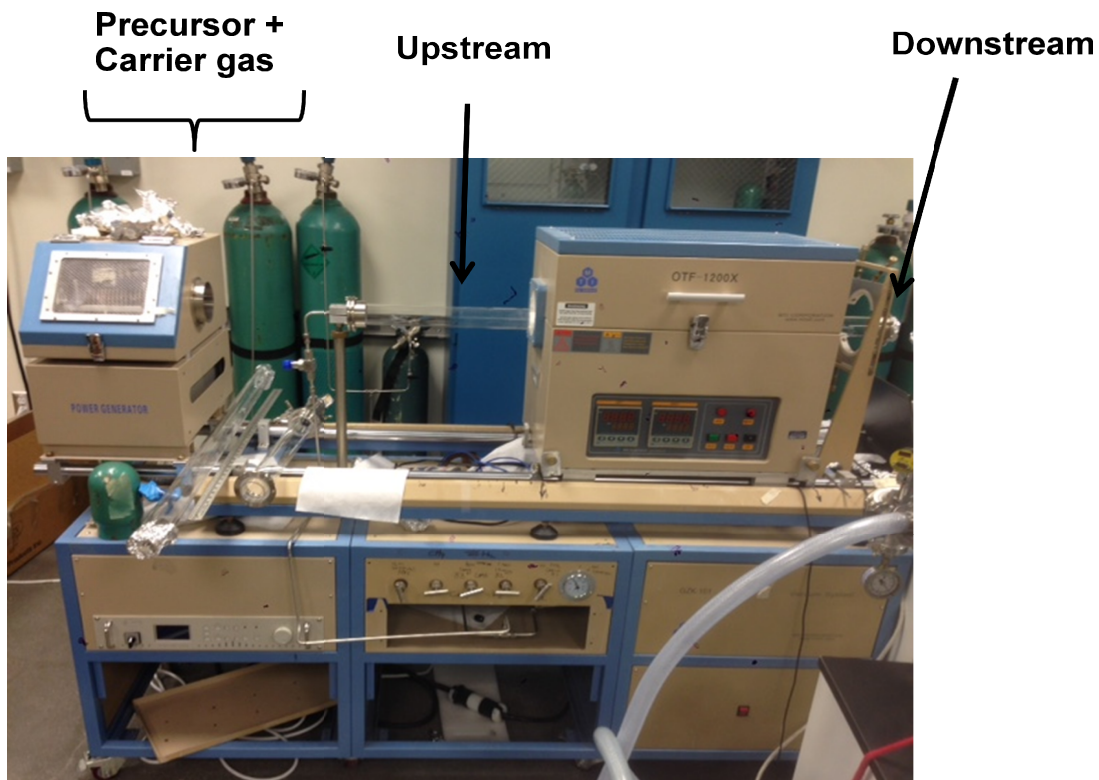


Figure 2-2. Photograph of a hot-wall CVD system used for the growth of graphene and h-BN. The reactor is essentially a long quartz tube that is heated externally by a furnace.

argon. The mass flow controllers control the flow rates of gases. Hydrogen serves as a dual role in the CVD growth of graphene² and h-BN³ on copper. It not only keeps the copper surface clean by reducing any surface oxide back to pure copper but also a controlled amount of hydrogen during growth regulates the film thickness to strictly monolayer by etching away any extra active species that can otherwise contribute to the growth of more than layer.² For the CVD growth of graphene, highly diluted methane balanced with argon serve as a carbon source.⁴ At a temperature of 1000°C and above, methane decomposes into carbon radicals on the copper surface that rearrange into graphene.⁵ For the CVD growth of h-BN, Ammonia-Borane complex (BH₃-NH₃) is used as a precursor.⁶ It is a white solid, which when heated close to 120°C, start to liberate hydrogen violently.⁷ At a temperature of 1000°C and above, it completely decomposes on a copper surface to form crystalline h-BN.⁶

The downstream-end of this CVD system can be switched between the exhaust or the roughing pump, as shown in Fig. 2-3. The liquid nitrogen cold-trap inserted between the downstream-end and the roughing pump not only prevents back-streaming of pump-oil into the quartz tube but also avoids condensation of any gas vapor coming from the quartz tube, inside the pump-oil.

In a typical growth experiment, after inserting acid-cleaned copper foils into the quartz tube, the whole CVD system is pumped down to a base pressure of ~20 mTorr and then vented back to atmospheric pressure with argon. This process of pump-down and venting is usually repeated three times to keep the inner ambient of quartz tube clean, before the growth process. After this step, the furnace is ramped-up at 20°C/min to a certain growth temperature, under argon and hydrogen ambient. When the desired temperature is reached, either dilute methane in argon is introduced into the gas stream for the growth of graphene crystals,⁴ or Ammonia-Borane

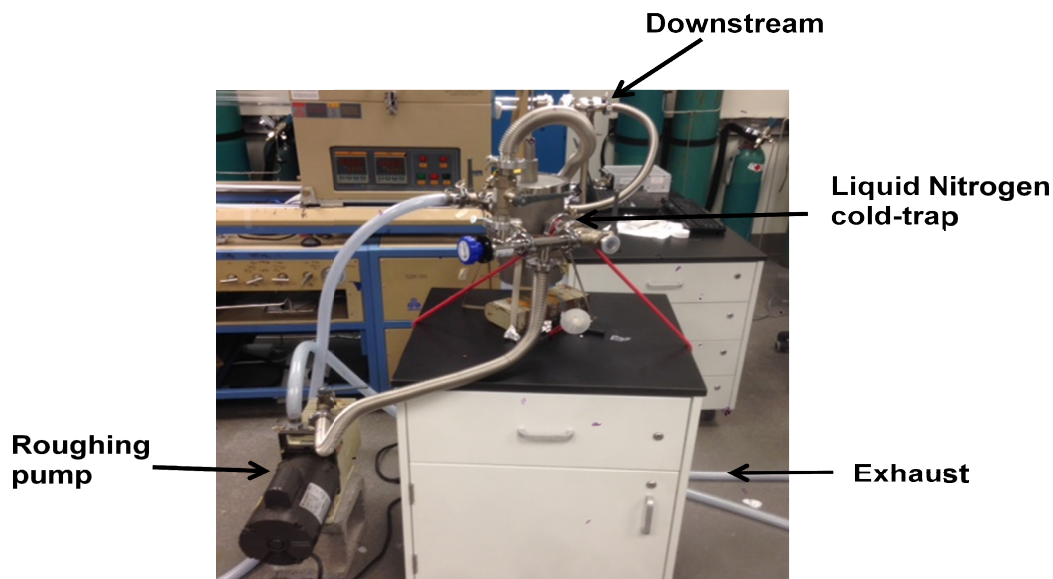


Figure 2-3. A photograph showing the downstream end of the CVD furnace. The downstream of the CVD system can be switched between the exhaust or the roughing pump. The liquid nitrogen cold-trap is inserted between the downstream-end and the roughing pump, to prevent any condensation of the vapor inside the pump-oil as well as the backstreaming of pump-oil into the quartz tube.

complex is heated by an external heating belt for the growth of h-BN crystals.⁶ After the growth process is finished, the furnace is opened for the fast-cooling of the copper foils without changing the gas flows. The samples are typically unloaded, when the temperature falls below 80°C, under argon ambient only.

2.2 Characterization techniques

2.2.1 Scanning electron microscope

A Scanning electron microscope (SEM) uses a highly focused electron-beam to produce high-quality images from specimens, at a spatial resolution much higher compared to an optical microscope.^{8,9,10} One of the main advantages of using an electron-beam for sample illumination is that electrons can be easily accelerated to higher energies, which dictates their shorter wavelength compared to visible light.^{8,9,10} A spatial resolution of sub-10 nm can be achieved in modern SEM, by accelerating an electron-beam up to 30kV.⁸ In an SEM, an electron-beam is raster-scanned across the specimen surface. Due to the interaction of electron-beam with the specimen, different types of electrons are emitted that can be detected with a dedicated detector.¹⁰ A computer software then correlates a signal from the detector, with the corresponding position of the electron-beam during raster-scan, to generate an image of the sample. A variety of specimens, including biological materials, can be studied in SEM under various conditions, e.g., high vacuum or medium pressures, specific gas environment, low or elevated temperatures. As the electron beam impinges the sample surface, a variety of electrons are emitted from the interaction volume, which is essentially a tear-shaped specimen volume,¹⁰ as shown in Fig. 2-4. The resolution of SEM is limited, not only by the probe-size of the electron beam but also by the spatial dimensions of the interaction volume. Low energy secondary electrons (SE) having

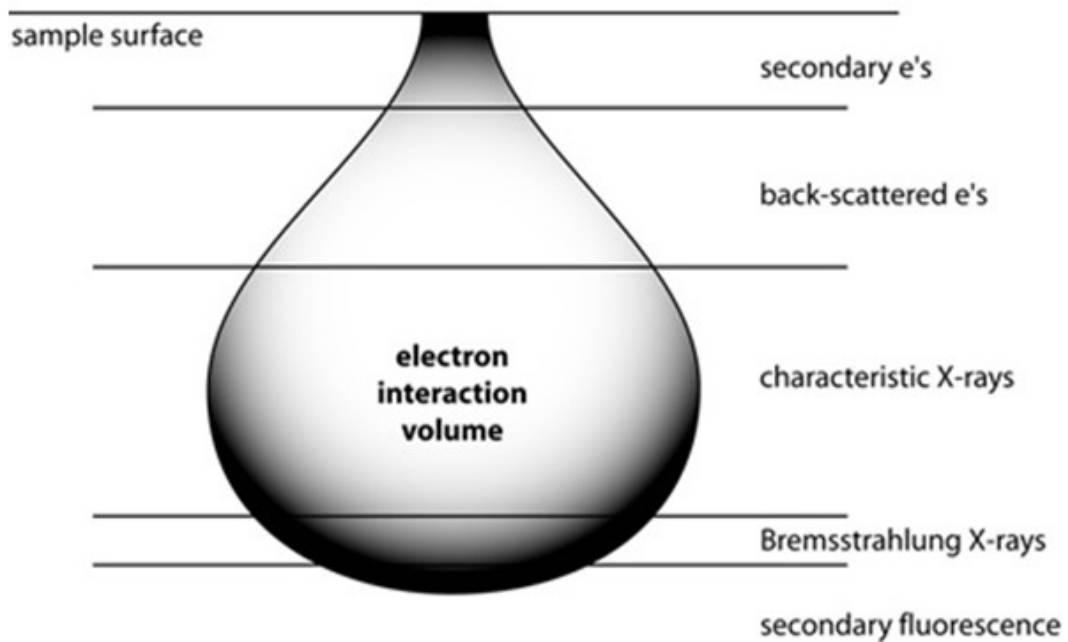


Figure 2-4. Interaction volume in SEM. The electron beam-sample interaction results in the emission of a variety of electrons, from a tear-shaped volume of a specimen, known as interaction volume. Each of these electrons contains valuable information about the sample. Reprinted with permission from ref. 8.

energies between 5-50 eV, and lower escape depth of 5-50 nm are most commonly used for imaging purpose, as they provide detailed information about the topography of specimen.⁸ Some of the incident electrons are reflected back, as a result of their elastic interactions with the atoms of the sample.⁹ These are known as back-scattered electrons, having energies from 50eV up to the energies of the primary electron beam. As a result of stronger Coulomb interaction between the nuclei of heavy atoms and incident electrons, the emission of back-scattered electrons increases with the atomic number of elements comprising the specimen. Hence, imaging with back-scattered electrons naturally depicts Z-contrast.⁸ During sample-electron beam interaction, most of the incident electrons are scattered, and some of these scattered electrons undergo diffraction, as they are incident on the crystal planes of the specimen at Bragg angles.¹⁰ These electrons are called diffracted back-scattered electrons and can be used to study the crystalline orientation of a sample in a technique known as electron backscatter diffraction (EBSD).¹¹ The high energy incident electron beam can also knock-off some of the core-shell electrons in the atoms of the specimen, resulting in some empty positions in the electronic shells. Electrons from higher shells jump to lower energy levels to fill those holes, resulting in X-ray emission of a characteristic wavelength that is dictated by the energy difference between the two levels involved in this transition.¹² Atoms of different elements have distinct energy levels. Hence, the wavelength of the emitted X-rays serves as a fingerprint to identify a particular element, in a technique known as energy dispersive spectroscopy (EDS).¹² The high energy electrons incident on the sample are further decelerated, as they travel deeper into the specimen, as a result of their strong interaction with the nuclei of atoms in the specimen. This process results in the emission of Bremsstrahlung X-rays, whose maximum energy cannot be greater than the energy of incident electron beam.¹² Finally, if the primary electron beam with a sufficiently high energy is incident

on a semiconductor specimen, it can excite electrons from valence to conduction band of a material. Electrons in the conduction bands relax to lower energy states, by the emission of photons that can be used for imaging in a technique known as Cathodoluminescence (CL) imaging.⁸

In the SEM imaging of a sample with rough topography, the angle of incidence of the electron beam relative to the sample is important, as it changes the dimensions of the interaction volume that in turn dictates the emission of secondary and back-scattered electrons.¹³ Hence, samples with rough topography require careful consideration, for the proper interpretation of bright and dark features in the corresponding SEM images.

2.2.2 Atomic force microscopy

An atomic force microscopy (AFM) can be used not only for specimen imaging but also to reveal local properties of materials as well.¹⁴ The operating principle of an AFM¹⁴ is shown in Fig. 2-5. A cantilever with a sharp tip attached at the bottom is scanned in a raster-fashion over small regions of a sample. A stationary laser beam is directed over a cantilever head, and the laser reflected-off is sensed by a fixed four-quadrant photodiode. The horizontal and vertical deflections of a cantilever, due to tip-sample interaction can be measured, by keeping track of a quadrant that detects the reflected laser. The entire system is a part of feedback loop that adjusts different parameters to control the movement of a cantilever. The AFM tips are made from either silicon or silicon nitride, with tip-ends having dimensions of few tens of nm.¹⁴ The lateral resolution of AFM is low up to tens of nm, but the vertical resolution can be up to 0.1 nm.¹⁵ This is the key advantage of an AFM over electron and optical microscopes because later cannot measure sample thickness with higher resolutions. AFM can be operated in different modes,

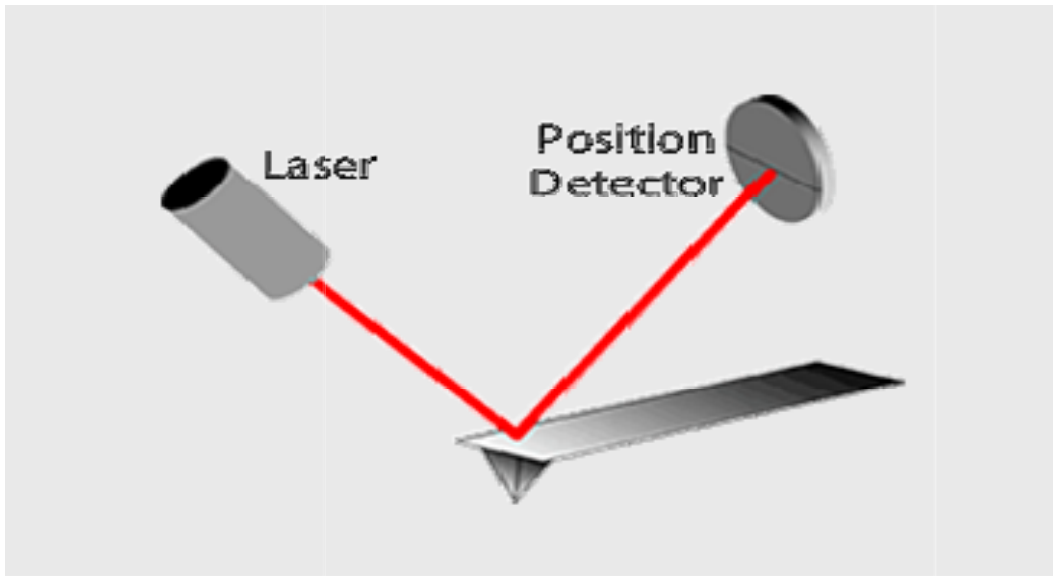


Figure 2-5. Operating principle of an AFM. A sharp tip attached to a cantilever scans across a sample surface, while a laser beam is guided to the cantilever head. The reflected laser is intercepted by a four-quadrant photodiode that detects horizontal and vertical deflections of the cantilever, as a result of tip-sample interactions. The feedback loop translates the vertical movement of the cantilever to generate images of surface topography. Reprinted with permission from ref. 14.

depending upon the information of interest.¹⁴ In a force mode, the mechanical properties of a sample, e.g., Young's modulus as a function of the separation between tip and sample can be measured.¹⁴ AFM can also be used to scribe features on a sample surface, in a controlled manner.¹⁶ In an imaging mode, the response of the tip, as a result of sample-tip interaction can be used to study the topography of a sample. The imaging procedure can be further classified into contact, non-contact and tapping modes.¹⁶ In a contact mode, a tip comes in contact with a surface during scanning. The vertical deflections of the tip are a direct measure of surface topography. This imaging mode is also known as a constant height mode because a feedback loop keeps the tip-sample distance constant while the tip scans across the surface. The adjustments needed to raise or lower the cantilever height are directly translated to generate an image of sample topography. There is another variant of contact mode known as a constant force mode, in which the force acting on a tip is kept constant, during scanning. The changes in the tip-height are then a direct measure of surface topography. In a non-contact mode, a cantilever oscillates at a resonant frequency and amplitude, while it scans across the specimen. Due to the tip-sample interactions, the resonant frequency of the tip is reduced. The feedback loop then adjusts the distance between tip and sample surface, to maintain the resonant frequency of the cantilever. This variation in tip-sample distance is then translated by an imaging software, to generate an image of the surface. In a tapping mode, a cantilever oscillates at a resonant frequency, and a feedback loop maintains the amplitude of oscillation during scanning. Depending upon the surface topography of the specimen, the tip intermittently touches the surface, and as a consequence, its amplitude of oscillation gets reduced. The feedback loop then adjusts the height of cantilever to preserve its amplitude of oscillation. The imaging software then uses the intermittent sample-tip interactions to generate images of sample topography

2.2.3 Transmission electron microscope

A Transmission electron microscopy (TEM) uses a very high energy beam of electrons to study thin specimens at a very high spatial resolution of up to sub-nm.¹⁷ The advantage of using an electron beam for sample imaging is that the former can be accelerated to very high energies, to achieve higher spatial resolutions.¹⁷ Typical TEM operate between 100-300kV. Another advantage of using electron beam for specimen illumination is that it is easier to build electron sources that produce higher brightness.¹⁷ A TEM specimen is usually very thin up to few tens of nm, and as an electron beam impinges upon the sample, only a fraction of it passes through it. An image obtained from TEM is not straightforward to elucidate, compared to an SEM image, and a proper understanding of a particular TEM operating mode is needed for image interpretation. Lenses in TEM are electromagnetic, just like in an SEM, and their strengths can be changed, by changing the currents passing through the coils. An electron column of a typical TEM¹⁷ is shown in Fig. 2-6. An electron source produces a very bright and coherent electron beam to generate high spatial resolution images from specimens. The two condenser lenses define illumination area and spot size of an electron beam, on the sample. The condenser lenses can be used to produce either parallel or convergent electron beam. For normal TEM imaging and diffraction modes, a parallel electron-beam is used for sample illumination. In scanning transmission electron microscopy (STEM) mode, a highly convergent electron-beam is used for imaging purpose. A condenser aperture can be inserted in the electron beam path, to reduce any aberrations introduced by the condenser lenses. The objective condenser and imaging lenses are used to focus and magnify an image of the specimen. The specimen sits in between these two lenses. The objective aperture can be inserted, to increase in an image contrast. Intermediate lenses magnify the image produced by the objective lenses that is further magnified by the

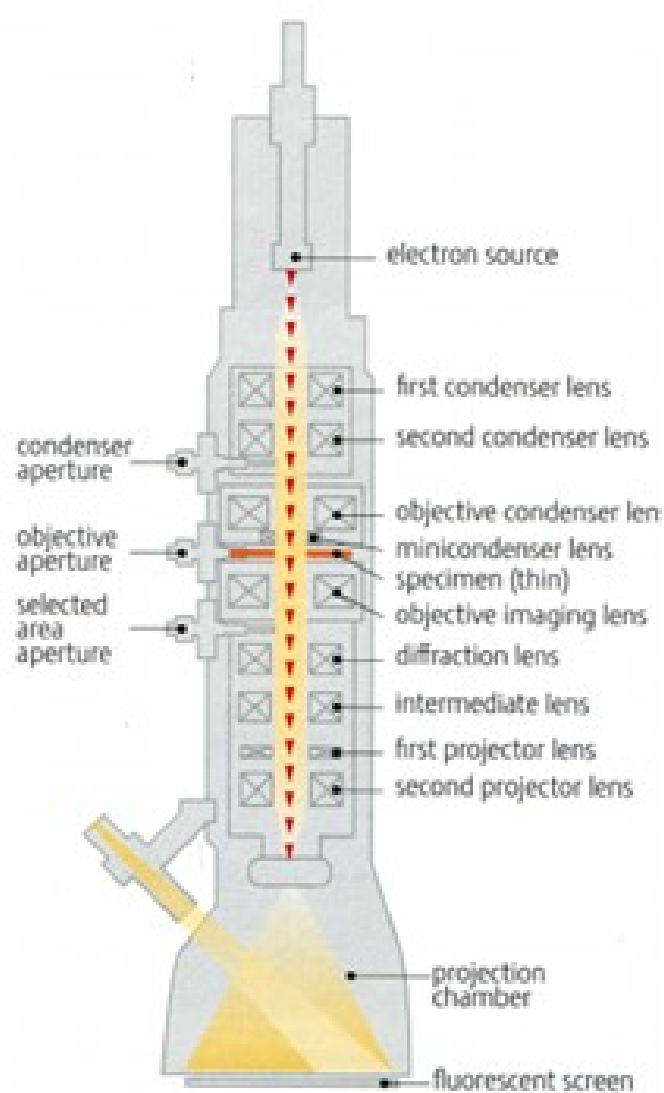


Figure 2-6. An electron column of a typical TEM. A bright and coherent electron beam produced by an electron source is condensed by condenser lenses, to define an illumination area on the sample. Objective lenses are used to focus and magnify an image of the sample that is further magnified by intermediate and projector lenses and is finally displayed on the fluorescent screen. Reproduced with permission from ref. 17.

projector lenses and is finally displayed on the phosphor screen.

A TEM is operated in either imaging or diffraction mode.¹⁷ The difference between the two can be explained with the help of ray-diagrams, as shown in Fig. 2-7.¹⁷ A parallel beam of electrons is impinging on the sample. During the process of image formation, an objective lens produces both diffraction patterns from the sample in the back-focal plane, as well as the real-space image in the imaging plane. Thus, both the imaging and back-focal planes are conjugate. The intermediate lens can be focused onto either back focal-plane to magnify diffraction patterns from the specimen (Fig. 2-7a), or it can be focused onto imaging plane (Fig. 2-7b) to magnify a real-space image of the sample. In a selected-area diffraction (SAED) mode, a selected-area aperture is inserted in the imaging plane to select a portion of the sample that contributes to the diffraction on the screen.¹⁷

A TEM can also be used to generate diffraction contrast images.¹⁷ There are two imaging modes to obtain diffraction contrast images. In a bright-field imaging mode, an objective aperture is inserted in the imaging plane of an objective lens to intercept the diffracted beams, while allowing the directly transmitted beam through the sample for image formation, as shown in Fig. 2-8a. In a dark-field imaging mode, an objective aperture can be used to intercept the directly transmitted beam, and only allows one of the diffracted beams for image formation, as shown in Fig. 2-8b.

2.2.4 Z-Contrast scanning transmission electron microscope

In a scanning transmission electron microscope (STEM), a highly converged electron beam is raster-scanned across the sample, just like in an SEM.¹⁷ The main differences, however, compared to an SEM, are that the sample in a STEM is very thin, and a transmitted electron-

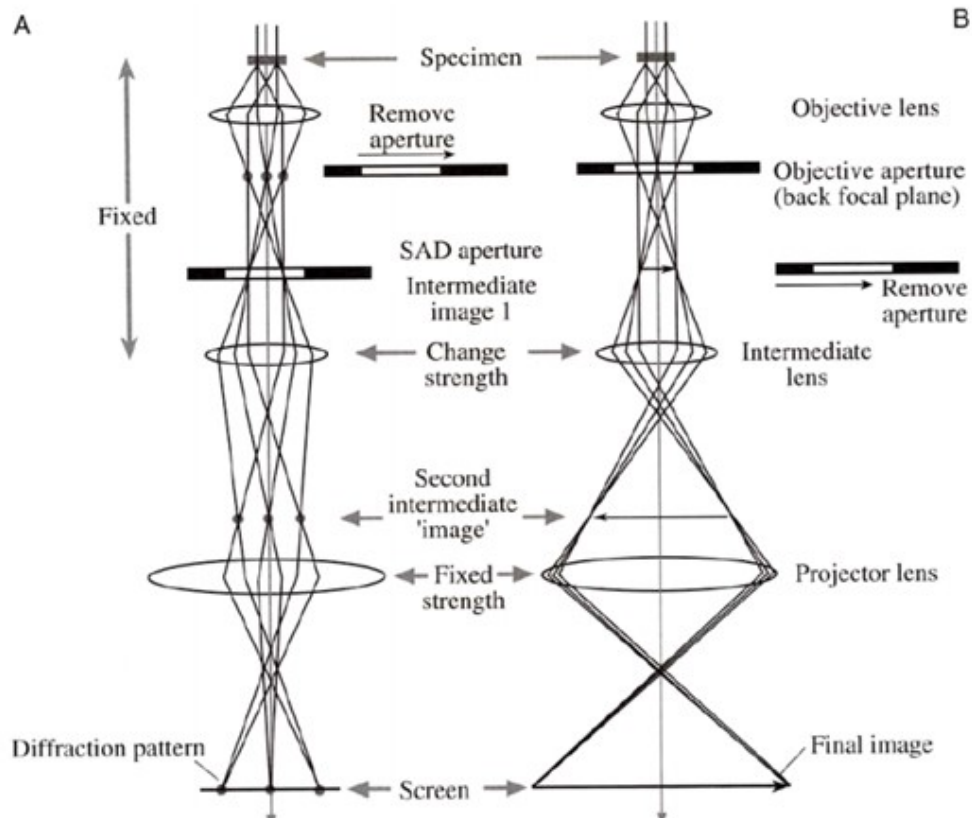


Figure 2-7. Two common operating modes of TEM. (a) In a diffraction mode, an intermediate lens is focused onto the diffraction pattern produced by the objective lens in the back-focal plane. (b) In a real-space imaging mode, an intermediate lens is focused onto the real-space image produced by the objective lens in the imaging plane. In both cases, projection lens serves to further magnify the image produced by the intermediate lens and displays it on the screen. Reproduced with permission from ref. 17.

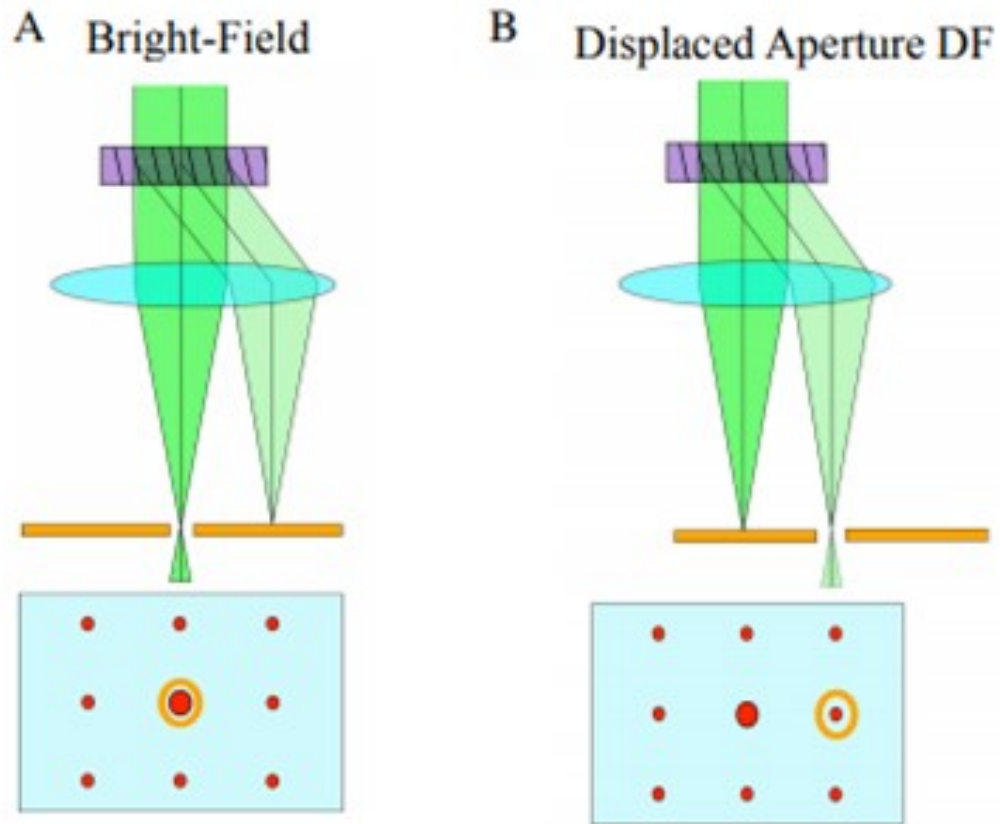


Figure 2-8. Diffraction contrast imaging in TEM. (a) In a bright-field imaging mode, an objective aperture is inserted in the imaging plane of an objective lens to block diffracted electron-beams, and only allows directly transmitted beam through the sample for image formation. (b) In a dark-field imaging mode, an objective aperture is inserted to intercept directly transmitted electron-beam, while allowing only one of the diffracted beams for image formation. Reproduced with permission from ref. 17.

beam through the sample is used for image formation. In the modern aberration-corrected STEM, atomic resolution imaging can be achieved.¹⁸

As the high energy electron beam interacts with the atoms in the specimen it gets scattered,¹⁷ as shown in Fig. 2-9a. If an electron-beam interacts with the electron cloud in an atom only, it is scattered by a small angle θ_2 . However, an electron that comes close to a nucleus gets scattered by a large angle θ_1 , due to the strong Coulomb attraction. Greater the atomic number of the nucleus, larger will be the scattering angle. In some cases, the primary electron-beam is even back-scattered, if the scattering angle is greater than 90° , as shown in Fig. 2-9a. For the electron-beam sample interaction shown in Fig. 2-9a, the principal electron beam does not lose much of its energy, hence, such interactions are termed as elastic. Also, there is no phase relationship between the scattered electrons that are scattered at large angles by the isolated atoms. This high angle-scattering of an incident high energy electron by an isolated atom is known as incoherent Rutherford scattering.¹⁷ The signal intensity I due to scattered electrons scales with atomic number Z of the scattering atom approximately as $I \propto Z^2$, and therefore imaging with such scattered electrons, naturally depicts Z -contrast in the images.¹⁷ This is the idea behind Z -contrast STEM,¹⁹ as shown in Fig. 2-9b, where a large annular detector known as high-angle annular dark-field detector (HAADF) is used to collect electrons that are scattered at large angles, by the atoms in the specimen. Typical values of β_1 and β_2 are ~ 50 mrad and ~ 200 mrad, respectively.¹⁹ The presence of Z -contrast makes the interpretation of images much easier, as the heavier elements in the specimen contribute to the bright features in the images.

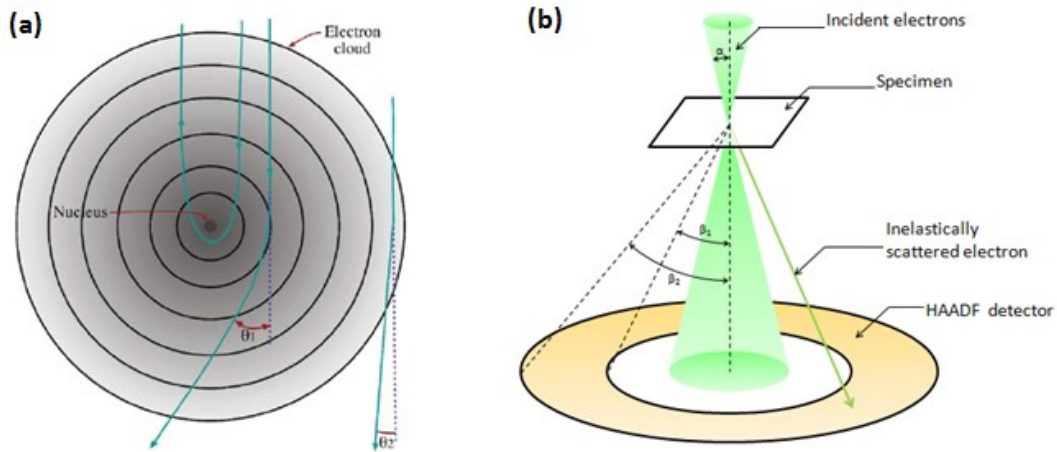


Figure 2-9. Incoherent Rutherford scattering and Z-contrast STEM. (a) A high energy incident electron is scattered by a large angle θ_2 , due to the strong Coulomb attraction force exerted by a nucleus of an isolated atom. (b) In a Z-contrast STEM, electrons that are scattered at large angles by the atoms in the specimen are collected by a large annular detector. These scattered electrons naturally contain elemental Z-contrast. Typical values of β_1 and β_2 are ~ 50 mrad and ~ 200 mrad, respectively. Reproduced with permission from ref. 19.

2.2.5 Raman spectroscopy

As a vibrational spectroscopy technique, Raman spectroscopy is used as a fingerprint to identify materials and compounds.²⁰ If a sample is illuminated by a laser, the electromagnetic field of photons, induce a dipole moment in molecules exciting them to a virtual high energy state.²⁰ This excited state is short-lived, on the order of femtoseconds, and the molecule returns to ground state and a scattered photon is released having same energy and wavelength as the incident photon. This elastic scattering, which is predominant when a monochromatic light is scattered by particles much smaller than the wavelength of incident light, is known as Rayleigh scattering,²¹ as shown in the left portion of Fig. 2-10. Raman scattering, however, is inelastic as the wavelength of the scattered photon is either higher or lower than the incident photon.²¹ In Stokes Raman scattering (middle panel of Fig. 2-10), a molecule excited to a virtual high energy state by an incident photon returns to a vibrational lower energy state by releasing a scattered photon that has a lower energy and longer wavelength, than the incident photon. The probability of such an event is very low, e.g., one in a million. That is why, the strength of Raman scattering signal is much weaker than a Rayleigh scattering. In an Anti-Stokes Raman scattering event, a molecule already in a vibrational high energy state returns to ground state, due to its interaction with an incident photon. As a result, a scattered photon having a shorter wavelength and higher energy than the incident photon is released. These shifts in the energies of the scattered photons with reference to the incident photons are the characteristics of the molecules comprising the sample, and hence serve as fingerprints, to identify materials. Not all the molecular vibrations are Raman active. Only the vibrations modes that can change the polarizability of a molecule contribute to Raman scattering.²¹ The statistics of the population of the molecules in the ground state or vibrational high energy states are dictated by Bose-Einstein statistics.²² Hence, the population of

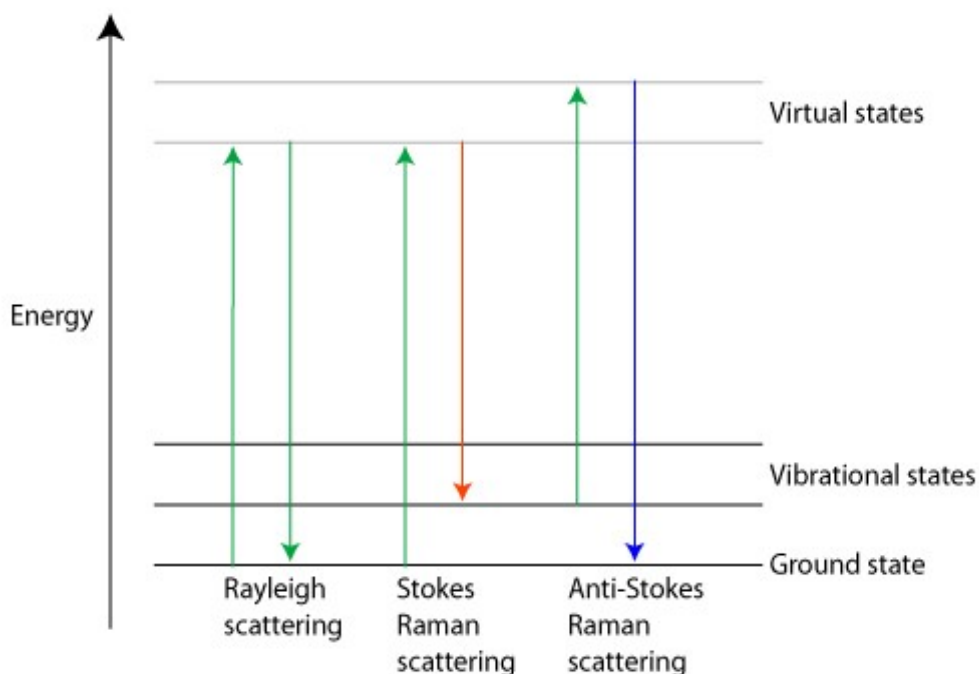


Figure 2-10. Rayleigh vs Raman scattering. In Rayleigh scattering, a molecule excited to a virtual high energy state by an incident photon returns to a ground state, and a scattered photon is released having same energy and wavelength as the incident photon. In a Stokes Raman scattering, an incident photon excites a molecule to a virtual high energy state which later returns to a vibrational lower energy state, by releasing a scattering photon of longer wavelength than the incident photon. In an Anti-Stokes scattering, an incident photon brings a molecule already in a vibrational energy state to a ground state, by releasing a scattered photon having a shorter wavelength than the incident photon. Reprinted with permission from ref. 21.

of molecules in vibrational high energy, states is much lower, compared to molecules in ground states, at room temperature.²² As a result, the intensity of Anti-Stokes Raman scattering signal is much lower than the Stokes Raman scattering.²²

A typical Raman spectrum is plotted as an intensity of the scattered light during Raman scattering process versus Raman shift, where Raman shift (cm^{-1}) = $\frac{1}{\lambda_{\text{incident}}} - \frac{1}{\lambda_{\text{scattered}}}$.²¹ Representing a Raman spectrum in the units of Raman shift, makes it independent of the excitation wavelength.²¹ The high intensity Rayleigh scattering signal that does not contain any useful sample information is usually rejected by a filter, during data acquisition.²¹ Typically, a Raman spectrum of a material only shows a Stokes part, as the Anti-Stokes part carries the same information as the Stokes part, but with a much reduced signal intensity.²¹ Apart from the identification of materials, Raman spectroscopy can reveal much more information about a particular specimen.²⁰ The width of the Raman peaks depicts the crystallinity of the sample, with sharper peaks indicating higher crystallinity of a given sample.²⁰ The heights of the characteristic Raman peaks of a material indicate relative concentration of that material in a mixture.²⁰ Also, the shifts in the position and direction of the characteristic Raman peaks can be used to evaluate stress and strain in a material.²⁰ By using a polarized laser light for data acquisition, the Raman peaks due to certain molecular vibrations can be enhanced depending upon laser polarization, which can reveal more information about the orientation of molecules in the specimen.²⁰

Next, we discuss the Raman spectrum of monolayer graphene. Fig. 2-11a shows a typical Raman spectrum of pristine (top panel) and defective (bottom panel) monolayer graphene.²³ If a sample is illuminated with laser with excitation wavelength of 514nm, the most important peaks in the Raman spectrum of pristine monolayer graphene are G and 2D peaks, with Raman shifts

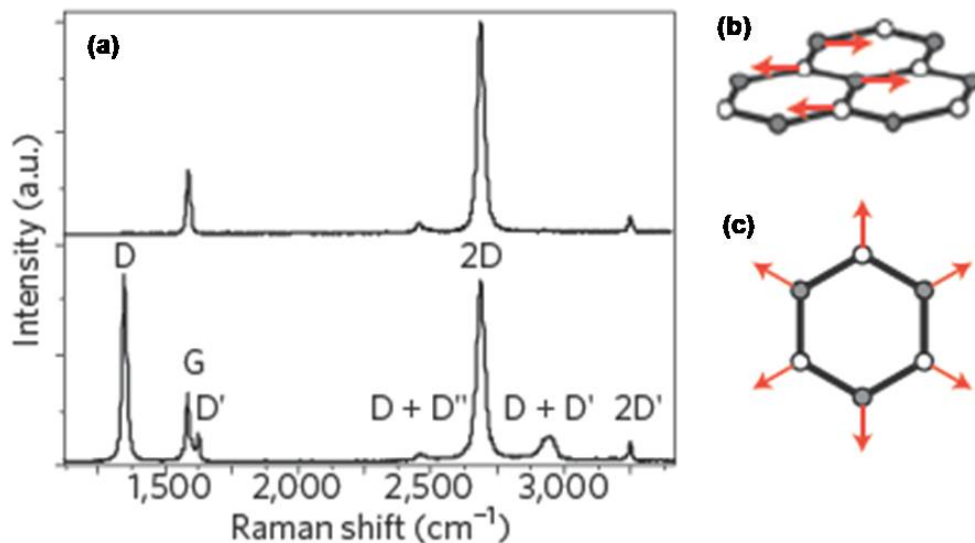


Figure 2-11. Raman spectrum of monolayer graphene. (a) Raman spectrum of pristine (top panel) and defective (bottom panel) monolayer graphene. (b) In-plane and opposite motions of carbon atoms belonging to different sub-lattices are responsible for the G peak in graphene (c) Breathing motion of carbon atoms in the ring is responsible for the observation of D peak. Reprinted with permission from ref. 23. Copyrights 2013 Macmillan Publishers Limited.

of $\sim 1580 \text{ cm}^{-1}$ and 2680 cm^{-1} , respectively, and less intense $2D''$ and $D+D''$ bands occurring with Raman shifts of $\sim 3250 \text{ cm}^{-1}$ and 2450 cm^{-1} , respectively.²³ For a defective graphene, additional peaks arise with most intense being the D peak with a Raman shift of 1350 cm^{-1} , and less intense D' and $D+D'$ peaks with Raman shifts of $\sim 1620 \text{ cm}^{-1}$ and 2950 cm^{-1} .²³ The G peak is the characteristics of sp^2 nature of carbon atoms in graphene, and is due to the opposite in-plane motion of the carbon atoms belonging to different sub-lattices²³ as shown in Fig. 2-11b. The D peak is due to the breathing motion of the carbon atoms in the rings²³ as shown in Fig. 2-11c.

Due to the absence of bandgap in graphene, Raman scattering in graphene is always resonant meaning that the excited vibrational state happens to be an electronic state with a definite energy.^{23,24} The G peak in graphene is the only peak that arises from the fundamental selection rule in Raman scattering process i.e., $\mathbf{q} \approx 0$ which is satisfied by the phonons near the center point Γ of the first Brillouin zone in the reciprocal space.^{23,24} As a result, G peak is non-dispersive meaning that its frequency does not shift with the change in the wavelength of laser excitation.²⁴

Fig. 2-12a shows the first order Raman scattering process explaining the origin of G peak.²³ An electron with a given wavevector \mathbf{k} is excited by an incident laser photon from a filled valence band to an empty conduction band in graphene. A phonon with a wave vector $\mathbf{q} \approx 0$ brings this excited electron back to the valence band, with the release of a photon to conserve the overall energy in this transition.

The rest of the peaks in Raman spectrum of graphene involve more than one phonons, hence either double resonance (DR) or triple resonance (TR) processes have been proposed to

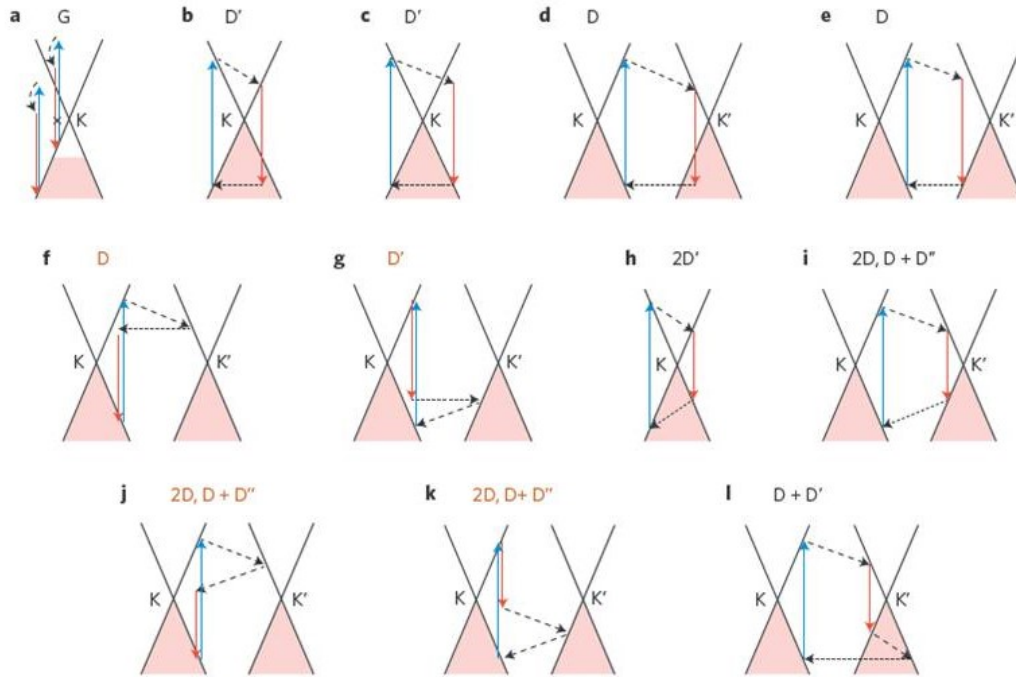


Figure 2-12. Raman scattering processes responsible for different peaks in monolayer graphene. Blue arrows represent electron-hole pair generation facilitated by an incident laser photon of a given energy. Red arrows represent electron-hole pair recombination along with a release of resulting photon. Black dashed arrows represent intermediate transitions of electrons or holes facilitated by phonons or defects. (a) First order Raman scattering process for G peak involving phonons with wave vector $\mathbf{q} \approx \mathbf{0}$. (b-g,j,k) Double resonance process responsible for D', D, 2D and D+D'' peaks. (h,i,l) Triple resonance process responsible for 2D', 2D, D+D'' and D+D' peaks. Orange labels indicate the contributions of those processes to the corresponding peaks are small. Pink regions represent filled energy states. Reprinted with permission from ref. 23. Copyrights 2013 Macmillan Publishers Limited.

explain their origin.^{23,24}

Fig. 2-12i explain the TR process responsible for the 2D and D+D'' peaks, in intrinsic graphene, where fermi-level lies at the K-point of Brillouin zone.²³ First, an electron with a given wave vector \mathbf{k} near the K-valley of graphene is excited by an incident laser from valence to the conduction band. This excited electron gets in-elastically scattered by a phonon of energy E_{phonon} and wave vector \mathbf{q} to a neighboring conduction band state with wave vector $\mathbf{k}+\mathbf{q}$ belonging to the K'-valley. This excited electron then falls back to the valence band state with a wave vector $\mathbf{k}+\mathbf{q}$, belonging to the same K'-valley. Then, a hole corresponding to valence band state with wave vector \mathbf{k} , belonging to the K-valley is scattered by a phonon with wave vector \mathbf{q} to recombine with this electron in the valence band state $\mathbf{k}+\mathbf{q}$, belonging to K'-valley. As a result of this electron-hole pair recombination, a photon is released. This process has three resonant sub-processes namely electron-hole pair generation, electron-hole scattering, and electron-hole pair recombination.^{23,24} Figs. 2-12j and 2-12k show two DR processes that can also explain the origin of the 2D peak, but their contribution is small compared to the TR process mentioned earlier.²³ This TR process responsible for the 2D peak is only possible in monolayer graphene, due to its unique perfect symmetry of conduction and valence bands around the Dirac point.²⁴ Also due to this TR process, the strength of the 2D peak is strongest in monolayer graphene, compared to the higher number of graphene layers.²⁴ Since, 2-4 layers of graphene exhibit band structures involving multiple conduction and valence bands around the K-point, the electronic states belonging to different bands can satisfy the requirements of DR process for the 2D peak.²⁴ As a result, 2D peak in 2-4 layers of graphene is composed of different sub-peaks, which can be used to differentiate up to 4 layers of graphene.²⁴ Also, a 2D peak does not require any phonon contribution from defects, hence it always shows up in pristine graphene.²³ The 2D peak happens

to be at roughly twice the Raman shift corresponding to the D peak, that is why it is labeled as “2D”.

Fig. 2-12d explains the origin of D peak.²³ Here an electron with a given wave vector \mathbf{k} around K-valley is first excited by a laser of given energy E_{laser} . This excited electron is then inelastically scattered by a phonon of energy E_{phonon} and wave vector \mathbf{q} to a neighboring conduction band state with wave vector $\mathbf{k}+\mathbf{q}$, belonging to the K'-valley. This electron then returns to the valence energy state corresponding to energy $E_{\text{laser}}-E_{\text{phonon}}$ and wave vector $\mathbf{k}+\mathbf{q}$, belonging to the same K'-valley. A defect with wave vector $-\mathbf{q}$ then elastically scatters back this electron to the original valence band state with wave vector \mathbf{k} , belonging to the K-valley, resulting in the release of a photon. This entire process is DR because it involves two resonant sub-processes namely electron-hole pair generation and recombination.^{23,24} Figs. 2-12e and 2-12f show two other possibilities of DR processes that can be used to explain the origin of D peak, but their contribution compared to the DR process in Fig. 2-12d is small.²³

Fig. 2-12b shows an intra-valley DR process responsible for D' peak.²³ This process is very similar to the DR process for D peak shown in Fig. 2-12d, except that in this case an electron with wavevector \mathbf{k} in the excited state gets scattered by a phonon with wave vector \mathbf{q} to the conduction band state with wavevector $\mathbf{k}+\mathbf{q}$, belonging to the same K-valley. A defect with wave vector $-\mathbf{q}$ finishes the DR process by scattering an electron from valence band state with wave vector $\mathbf{k}+\mathbf{q}$ to a starting valence band state with wavevector \mathbf{q} , both belonging to same K-valley, and releasing a photon. Figs. 2-12c and 2-12g explain two other possibilities of DR process for D' peak.²³ Since a defect is required to complete DR process for both D and D' peaks, these peaks only show up in samples of defective graphene.^{23,24} In fact, in highly defective graphene samples I_D/I_G ratio can be used to estimate crystal size.²⁴

Fig. 2-12h explains the TR process responsible for the overtone of D' peak²³ i.e. 2D' peak. This is very similar to the TR process responsible for the 2D peak in Fig. 2-12i, except that in this case scattering of an electron during the intermediate transitions is an intra-valley process involving conduction and valence band states of the same K'-valley. Since no defects are involved in the intermediate transitions, this peak always shows up in pristine graphene, just like the 2D peak.²³

Finally Fig. 2-12l shows TR process responsible for D+D' peak.²³ An electron with a wavevector \mathbf{k} near the K-valley of graphene is first excited by an incident laser from valence to the conduction band. This excited electron gets in-elastically scattered by a phonon of energy E_{phonon1} and wave vector \mathbf{q}_1 to a neighboring conduction band state with wave vector $\mathbf{K}+\mathbf{q}_1$, belonging to the K'-valley. This electron then returns to the valence band state with wave vector $\mathbf{K}+\mathbf{q}_1$ and is further in-elastically scattered by another phonon of energy E_{phonon2} and wave vector \mathbf{q}_2 to the neighboring valence band state with wave vector $\mathbf{K}+\mathbf{q}_1+\mathbf{q}_2$, belong to the same K'-valley. A defect with wavevector $\mathbf{q}_1+\mathbf{q}_2$ then scatters a hole from the valence band state with wave vector \mathbf{k} belonging to the K-valley, to the valence band state with wavevector $\mathbf{K}+\mathbf{q}_1+\mathbf{q}_2$ belonging to the K'-valley, thus resulting in the release of the photon as a result of electron-hole pair recombination.

All the peaks in Raman spectrum of graphene involving DR and TR processes, except the G peak are dispersive, meaning that their peak positions shift with the change in the excitation wavelength of the incident laser.²⁴ The reason for this behavior is that the wave vector of electron \mathbf{k} in the excited state is dictated by the energy of the incident laser photon E_{laser} .²⁴ When E_{laser} is increased or decreased, the wave vector of an electron in the excited state around K-valley is increased or decreased, accordingly.²⁴ Also, the wave vector of phonon \mathbf{q} required to

complete the intermediate transitions of electrons between different energy states, and its corresponding energy $\hbar\omega(q)$ is increased or decreased, accordingly.²⁴ As a result, Raman shifts corresponding to different peaks are shifted, depending upon E_{laser} .²⁴

2.3 References

- (1) Plummer, J. D.; Deal, M.; Griffin, P. *Silicon VLSI Technology, Practice and Modelling*. Prentice Hall-New York, 2000.
- (2) Vlassioulak, I.; Regmi, M.; Fulvio, P.; Dai, S.; Datskos, P.; Eres, G.; Smirnov, S. Role of Hydrogen in Chemical Vapor Deposition Growth of Large Single-Crystal Graphene. *ACS Nano* **2011**, *5*, 6069-6076.
- (3) Wu, Q.; Park, J.-H.; Park, S.; Jung, S. J.; Suh, H.; Park, N.; Wongwiriyan, W.; Lee, S.; Lee, Y. H.; Song, Y. J. Single Crystalline Film of Hexagonal Boron Nitride Atomic Monolayer by Controlling Nucleation Seeds and Domains. *Sci. Rep.* **2015**, *5*, 16159.
- (4) Yu, Q.; Jauregui, L. A.; Wu, W.; Colby, R.; Tian, J.; Su, Z.; Cao, H.; Liu, Z.; Pandey, D.; Wei, D. *et al.* Control and Characterization of Individual Grains and Grain Boundaries in Graphene Grown by Chemical Vapour Deposition. *Nat. Mater.* **2011**, *10*, 443–449.
- (5) Mattevi, C.; Kim, H.; Chhowalla, M. A Review of Chemical Vapour Deposition of Graphene on Copper. *J. Mater. Chem.* **2011**, *21*, 3324-3334.
- (6) Kim, K.K.; Hsu, A.; Jia, X.; Kim, S.M.; Shi, Y.; Hofmann, M.; Nezich, D.; Rodriguez-Nieva, J.F.; Dresselhaus, M.; Palacios, T.; Kong, J. Synthesis of Monolayer Hexagonal Boron Nitride on Cu Foil Using Chemical Vapor Deposition. *Nano Lett.* **2011**, *12*, 161-166.
- (7) Hu, M.G.; Geanangel, R.A.; Wendlandt, W.W. The Thermal decomposition of Ammonia-Borane. *Thermochimica Acta* **1978**, *23*, 249-255.
- (8) M.T. Postek, K.S. Howard, A.H. Johnson and K.L. McMichael, *Scanning Electron*

Microscopy: A Student's Handbook, Ladd Research Ind., Inc. Williston, 1980.

(9) Brief Introduction to Scanning Electron Microscopy. <http://cfamm.ucr.edu/documents/se-m-intro.pdf> (Accessed June 22, 2018).

(10) Darrell, H. Electron-Sample Interactions. https://serc.carleton.edu/research_education/geochemsheets/electroninteractions.html (Accessed June 22, 2018).

(11) Schwartz, A.J.; Kumar, M.; Adams, B.L.; Field, D.P. *Electron Back Scatter Diffraction in Materials Science*. Springer-Verlag US, 2009.

(12) C.E. Lyman, D.E. Newbury, J.I. Goldstein, D.B. Williams, A.D. Romig, J.T. Armstrong, P. Echlin, C.E. Fiori, D.C. Joy, E. Lifshin and Klaus-Ruediger Peters. *Scanning Electron Microscopy, X-Ray Microanalysis and Analytical Electron Microscopy: A Laboratory Workbook*. Plenum Press-New York, 1990.

(13) Scanning Electron Microscopy. <https://cmrf.research.uiowa.edu/scanning-electron-microscopy> (Accessed June 22, 2018).

(14) How an AFM Works. <http://nanoscience.com/technology/afm-technology/how-afm-works> (Accessed June 22, 2018).

(15) Mai, W. Fundamental Theory of Atomic Force Microscopy. <http://nanoscience.gatech.edu/zlwang/research/afm.html> (Accessed June 22, 2018).

(16) Zang, L. Basics of Atomic Force Microscope. <http://eng.utah.edu/~lazang/images/Lectur>

e_10_AFM.pdf (Accessed June 22, 2018).

(17) Williams, D. B.; Carter, C. B. *Transmission Electron Microscopy: A Textbook for Materials Science*, Springer-Verlag New York, 2009.

(18) Nion UltraSTEM™ 100. <http://www.nion.com/products.html> (Accessed June 22, 2018).

(19) High-angle annular dark-field scanning transmission electron microscopy. https://www.jeol.co.jp/en/words/emterms/search_result.html?keyword=high-angle%20annular%20dark-field%20scanning%20transmission%20electron%20microscopy (Accessed June 22, 2018).

(20) Raman Spectroscopy. <http://www.nanophoton.net/raman/raman-spectroscopy.html> (Accessed June 22, 2018).

(21) Raman spectroscopy-A tutorial. http://kosi.com/na_en/products/raman-spectroscopy/raman-technical-resources/raman-tutorial.php (Accessed June 22, 2018).

(22) Stokes and anti-Stokes Raman Scattering. <https://www.doitpoms.ac.uk/tlplib/raman/stokes.php> (Accessed June 22, 2018).

(23) Ferrari, A. C.; Basko, D. M. Raman Spectroscopy as a Versatile Tool for Studying the Properties of Graphene. *Nat.Nanotech.* **2013**, 8, 235–246.

(24) Malard, L. M.; Pimenta, M. A.; Dresselhaus, G.; Dresselhaus, M. S. Raman Spectroscopy in Graphene. *Phys. Rep.* **2009**, 473, 51–87.

CHAPTER 3

SYNTHESIS OF MILLIMETER-SIZE HEXAGON-SHAPED GRAPHENE SINGLE CRYSTALS ON RESOLIDIFIED COPPER

This chapter is a slightly modified version of the paper with the same title published in ACS Nano in September 2013 by Ali Mohsin, Lei Liu, Peizhi Liu, Wan Deng, Ilia N. Ivanov, Guoliang Li, Ondrej E. Dyck, Gerd, Duscher, John R. Dunlap, Kai Xiao and Gong Gu. The introduction in this chapter has been expanded to cover the most recent developments in this research area. Also, the supporting information in the published paper has been included as a part of the main text in this chapter.

All the figures and most of the text in this chapter are reproduced with permission from Mohsin, A.; Liu, L.; Liu, P.; Deng, W.; Ivanov, I. N.; Li, G.; Dyck, O. E.; Duscher, G.; Dunlap, J. R.; Xiao, K.; Gu, G. Synthesis of Millimeter-Size Hexagon Shaped Graphene Single Crystals on Re-solidified Copper. *ACS Nano* **2013**, 7, 8924-8931. Copyright 2013 American Chemical Society.

As a first author of the paper, I was responsible for (1) Designing of the experiments for the CVD growth of graphene crystals. (2) Optimization of the growth parameters. (3) Characterization of graphene crystals by Optical microscopy, SEM, and Raman. (4) Transfer of the graphene crystals onto the TEM grids. (5) Data analysis and writing of the manuscript. L. L. assembled the CVD system on which CVD growth experiments were carried out. P. L. and G. D. did the TEM characterization of the graphene crystals. Wan Deng performed the AFM of the different copper surfaces. I.N.I. acquired Raman area maps. G. L. and O.E.D performed EBSD characterization. J. R. D trained me on the SEM. K.X. and G.G. oversaw the research.

3.1 Abstract

We present a facile method to grow millimeter-size, hexagon-shaped, monolayer, single-crystal graphene domains on commercial metal foils. After a brief *in situ* treatment, namely melting and

subsequent re-solidification of copper at atmospheric pressure, a smooth surface is obtained, resulting in the low nucleation density necessary for the growth of large-size single-crystal graphene domains. Comparison with other pretreatment methods reveals the importance of copper surface morphology and the critical role of the melting-resolidification pretreatment. The effect of important growth process parameters is also studied to determine their roles in achieving low nucleation density. Insight into the growth mechanism has thus been gained. Raman spectroscopy and selected area electron diffraction confirm that the synthesized millimeter-size graphene domains are high-quality monolayer single crystals with zigzag edge terminations.

3.2 Introduction

Copper has recently become a popular catalytic substrate for the CVD growth of graphene, due to its low carbon solubility at typical growth temperatures.¹ Low or atmosphere pressure CVD grown graphene on copper is polycrystalline,² formed by the coalescence of domains.^{3,4} The polycrystalline nature lowers the overall electrical performance of CVD graphene-based devices,⁵ although certain types of grain boundaries are relatively benign to electrical transport.⁶ Recently, synthesis of hexagon-shaped single-crystal graphene domains attracted considerable interest in the graphene CVD community.^{7,8,9,10,11,12} The hexagonal crystallite shape is desirable due to the well-defined edge geometry (zigzag)¹¹ which is shown to have interesting electronic properties.¹³ In the earlier reports, the size of hexagonal single-crystal graphene domains was limited to tens of microns.^{7,8,9,10,11,12} Later reports revealed that smooth copper surface morphology plays an important role to limit the initial density of graphene nuclei to grow large single-crystal domains.^{14,15,16,17,18} By extended thermal annealing of the Cu foil, Wang *et al.* demonstrated square-shaped sub-millimeter single-crystal graphene domains with jagged

edges.¹⁴ Yan *et al.* reported the synthesis of hexagonal single-crystal graphene domains up to 2.4 mm in size by the prolonged pretreatment of copper foils including high-pressure annealing (~ 2 atm) for an extended period (7 hours) following electrochemical polishing.¹⁵ Chen *et al.* synthesized ~ 1.8 mm, single-crystal graphene domains by reducing copper evaporation from the inner walls of a copper enclosure used as a catalytic substrate, but the synthesis required low pressure (~ 70 mTorr) for a prolonged time (~ 6 hours).¹⁶ To overcome the barriers imposed by solid copper on the control of nucleation density, Geng *et al.* and Wu *et al.* grew graphene crystallites on liquid copper.^{17,18} Contrary to intuition, graphene nucleation density was higher on liquid copper than in the aforementioned reports and the domain size was limited to $200\text{ }\mu\text{m}$.^{17,18} The possible reason, subjected to further studies, is that the gradient in carbon concentration during cooling leads to convection within the liquid copper, which limits the size of graphene domains.¹⁹ The controlled amount of oxygen has also been found to play a key role in the growth of large area single crystals of monolayer graphene.^{20,21} By ramping-up the temperature of copper foils before graphene growth in argon environment only, Lin *et al.* showed that the nucleation density of graphene could be lowered by several orders of magnitude that resulted in the synthesis of graphene crystals up to sub-cm in dimensions.²⁰ Also, by introducing a small pulse of pure oxygen before the graphene growth under low-pressure conditions, Hao *et al.* showed the successful synthesis of cm-sized single crystals of graphene.²¹ The authors also showed that the introduction of oxygen just before the graphene growth, not only passivates the surface defects in copper that can otherwise contribute to uncontrolled graphene nucleation but also accelerates the graphene growth process by changing the growth mechanism from edge-attachment-limited to the diffusion-limited regime.²¹ More recently, Wu *et al.* developed an efficient way to synthesize an inch-sized graphene single crystals by a local feeding of carbon

source, on an optimized Ni-Cu alloy substrate.²² The use of Ni-Cu alloy allowed isothermal segregation of carbon that accelerated the graphene growth process.²²

3.3 Results and discussion

APCVD was used as a synthesis technique in this study due to its simple setup. Growth at atmospheric pressure also avoids copper evaporation from the foil substrate, an issue associated with low-pressure CVD (LPCVD).²³ Fig. 3-1a summarizes the growth of graphene on the resolidified copper surface. Commercial copper foils of 99.999% purity were used to minimize uncontrolled nucleation due to impurities, which can segregate on the resolidified copper surface after melting.⁹ After very brief initial cleaning to remove any manufacturer coating, copper foils are placed on a tungsten foil, to prevent de-wetting of liquid copper on quartz.^{17,18} To melt the copper, the substrate is heated at 1100 °C for 30 minutes under argon (940 sccm) and hydrogen (60 sccm). Then, the temperature is slowly ramped down to 1075°C, *i.e.* below the melting point of bulk copper (1084 °C), and the copper re-solidifies. Growth is carried out at this temperature, with 0.1% dilute methane in argon, hydrogen, and argon flowing at 46, 100, and 854 sccm, respectively, for 5 hours. Fig. 3-1b shows a photograph of the graphene domains made visible by oxidizing the unprotected copper surface by heat treatment on a hot plate.¹⁴ Fig. 3-1c shows a scanning electron microscope (SEM) image of the two graphene domains, identified in Fig. 3-1b. The side-to-side distance is ~ 1 mm, and the 120° angles between the hexagon sides are clearly identifiable. Compared to previous reports on millimeter-size single-crystal graphene,^{15,16} domains obtained in this study are more regular hexagons without rough edges.

Graphene growth on copper initiates by the formation of small stable single-crystal clusters, which then coalesce to form a polycrystalline film.³ Therefore, the key step in growing

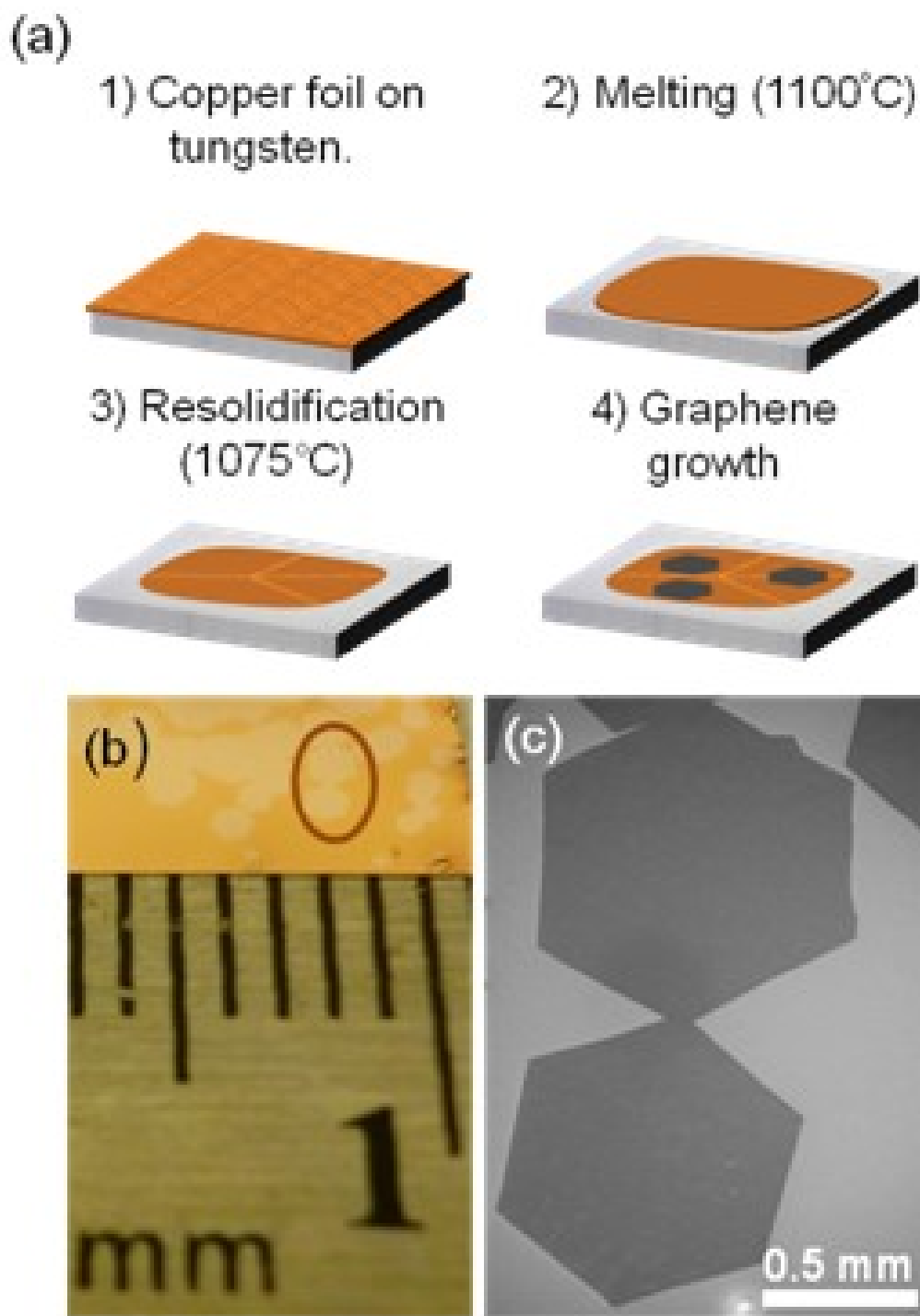


Figure 3-1. (a) A simple method to grow millimeter-size graphene single crystals on melted and resolidified copper. (b) Photograph of the synthesized domains. (c) SEM image of an area identified in (b).

millimeter-size domains is to have only one single-crystal cluster in $\sim 1\text{mm}^2$ area. To reveal the importance of copper surface morphology in achieving this goal, Fig. 3-2 shows graphene grown on different copper surfaces for 30 minutes at the same temperature (1075°C). Fig. 3-2a shows nearly complete graphene coverage on a solid copper foil that was annealed at 1075°C for 30 minutes before the graphene growth, with small un-covered copper surface areas as the one indicated by an arrow. Fig. 3-2b shows the graphene grown on electro-polished foils (also annealed at 1075°C for 30 minutes before the graphene growth), where the fraction of un-covered copper regions is much higher compared to Fig. 3-2a, indicating lower nucleation density on electro-polished foils. However, the nucleation density is still too high for the growth of millimeter-size domains. In Fig. 3-2c, on melted and re-solidified copper, only three hexagonal nuclei are present in a $\sim 3\text{mm}^2$ area. Fig. 3-2d shows a higher magnification image of the boxed region in Fig. 3-2a. Areas of darker contrasts, indicated by arrows, are assigned as multi-layer graphene.¹ Fig. 3-2e is a higher magnification image of the boxed region in Fig. 3-2b. Interestingly, all the graphene domains have small multilayer regions at the centers. This is due to the mounds introduced during electropolishing, as will be shown later, which can have a higher density of active carbon species, leading to stable graphene clusters.²⁴ The domain size, in this case, is $\sim 40\text{ }\mu\text{m}$. Fig. 3-2f is a higher magnification image of the region boxed in Fig. 3-2c, showing a graphene domain on melted and re-solidified copper, which exhibits a distinct hexagon shape with sides 120° apart, as well as a uniform contrast within it, indicating the absence of multilayer regions. The domain size, in this case, is $\sim 55\text{ }\mu\text{m}$, larger than obtained on electro-polished foils. The wrinkle-like features can also be seen as indicated by an arrow. These are due to the rolling features on the tungsten foil underlying the Cu foil, as will be shown later.

To further clarify the growth on thermally annealed solid copper, Fig. 3-3 shows SEM

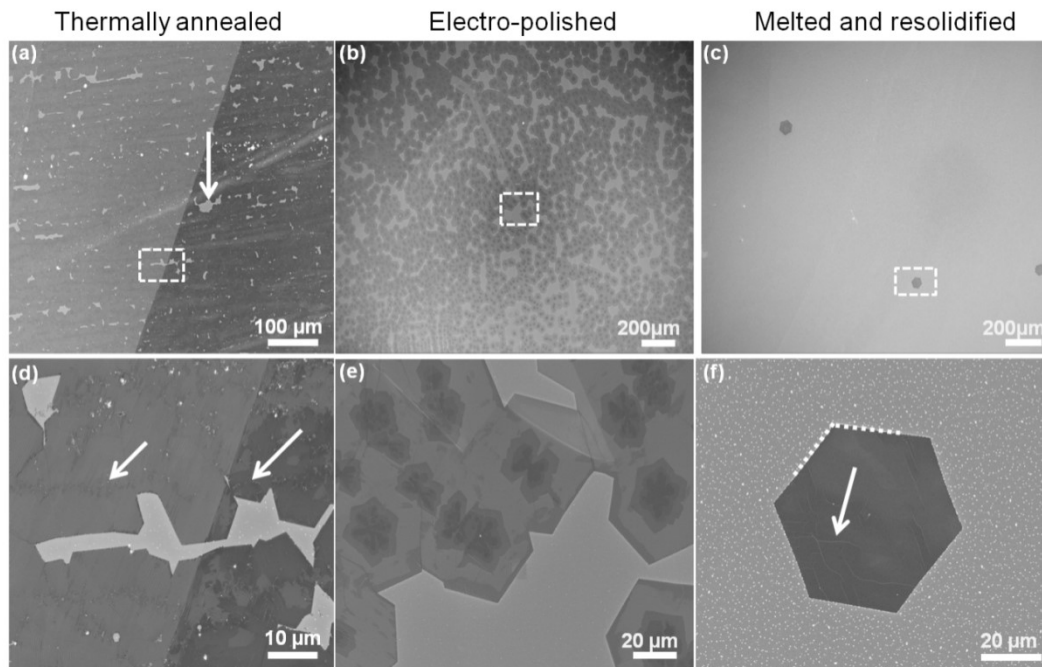


Figure 3-2. Comparison of graphene nucleation density on different copper surfaces. SEM images of (a) thermally annealed solid copper; (b) electro-polished foil; (c) melted and resolidified copper. (d-f) Higher magnification images of the areas identified in (a-c).

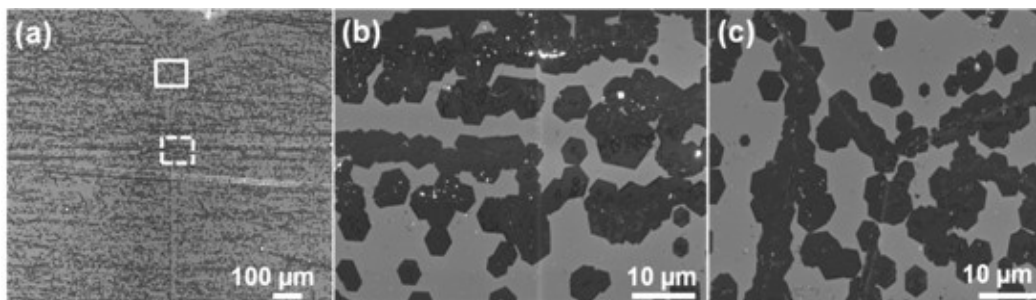


Figure 3-3. Graphene crystallites grown on thermally annealed solid copper over a short time duration (10 minutes). (a) Graphene domains preferentially nucleate along the surface irregularities, as they follow the pattern of underlying rolling marks on copper surface. Higher magnification images of the dashed (b) and the solid (c) boxes in (a).

images of graphene crystallites grown over a shorter duration of 10 minutes at the same temperature of 1075° C, as in Fig. 3-2 above. Fig. 3-3a shows that a high density of graphene nuclei roughly follow the underlying rolling features, present on commercial copper foils,^{9,1415} while Figs. 3-3(b,c) indicate that graphene nucleation density is low in the regions between the rolling marks. When the growth was carried out for 30 minutes, however, the dense graphene nuclei on the thermally annealed foil coalesced to result in nearly complete graphene coverage, as shown in Fig. 3-2a earlier. The higher initial nucleus density on the rolling features also leads to the formation of small multi-layer graphene regions.

To understand the significant reduction in the graphene nucleation density on melted and re-solidified copper as compared to thermally annealed and electro-polished foils, Fig. 3-4 shows the AFM topographical images of these copper foil surfaces. Fig. 3-4a shows that the root mean square (RMS) roughness of the as-received copper foil is ~ 166 nm and the surface is very irregular as shown by the corresponding line profile in Fig. 3-4e. Thermal annealing without melting and resolidification, as well as electro-polishing, reduces surface irregularities as shown by the line profile in Fig. 3-4e. Noticeably, for the melted and re-solidified copper, the surface roughness is only 8 nm and the surface profile is the smoothest in Fig. 3-4e. Interestingly in Fig. 3-4d, an additional set of features can also be seen. These are due to the surface morphology of the underlying tungsten foil. To verify, Fig. 3-5a and b show AFM images for the as-received tungsten foil as well as a foil annealed in the same manner as melted and resolidified copper foils. Fig. 3-5d and e show the corresponding SEM images taken at a tilt angle of 75°. The improvement in the surface roughness is slight, if any, after annealing (6.78 nm) compared to the as-received (6.96 nm), which is expected as tungsten is a refractory metal and the temperature at copper is melted in this study (1100° C) is well below the melting point of

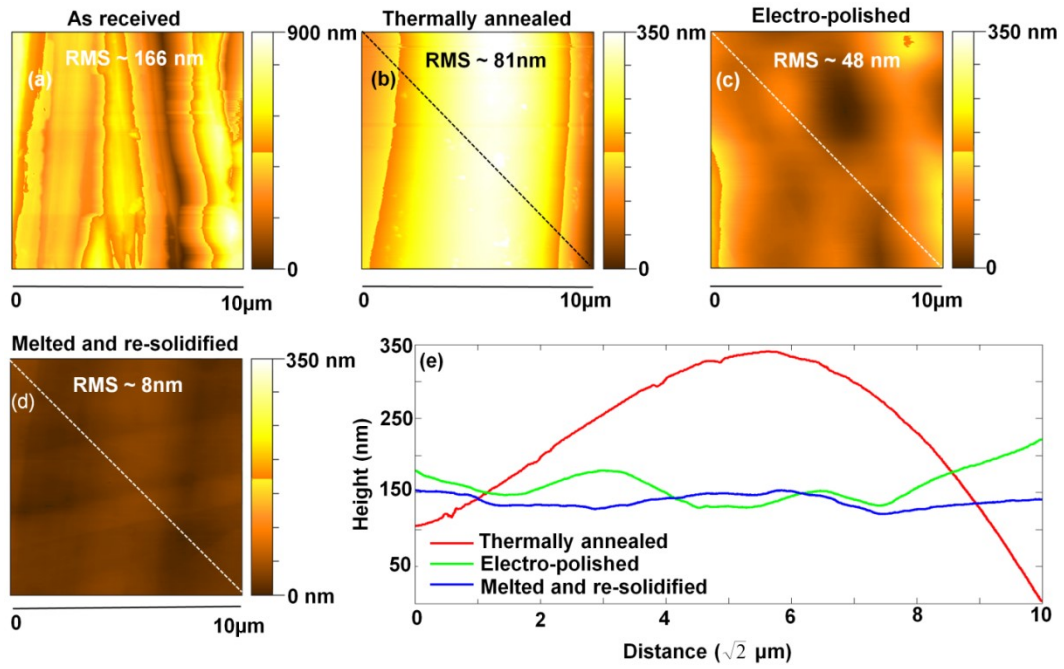


Figure 3-4. AFM topographical images of various copper surfaces. (a) As-received, (b) Thermally annealed, (c) Electro-polished, and (d) Melted and resolidified. (e) AFM line profiles corresponding to the white dashed lines marked in a-d.

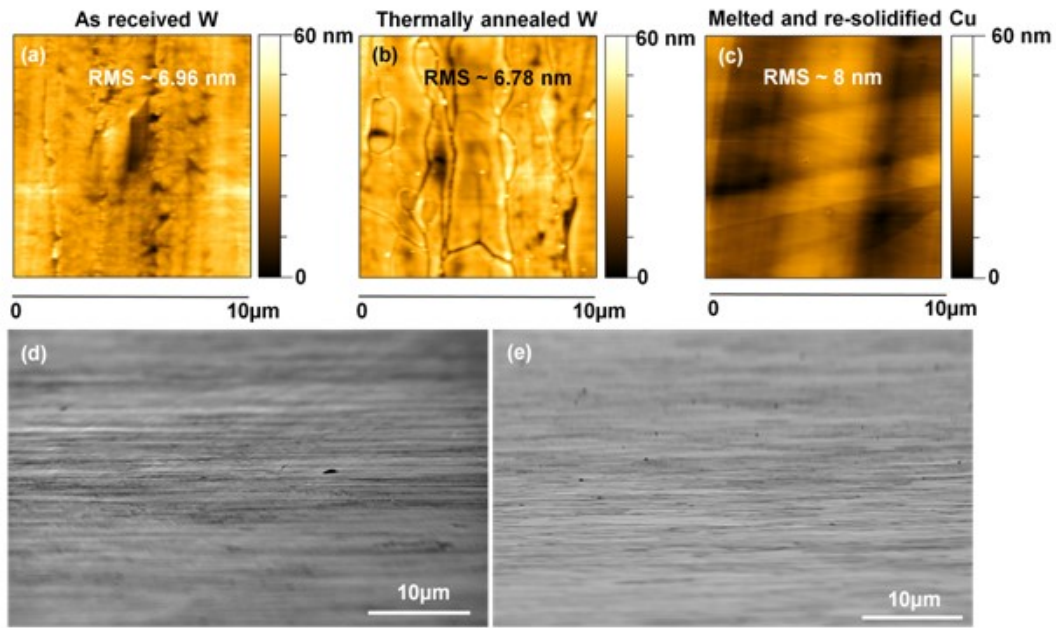


Figure 3-5. AFM and tilted SEM images of tungsten foils and re-solidified copper (a, b, c) AFM topographic images of (a) as-received, (b) annealed tungsten foils. And (c) melted and re-solidified copper (d, e) SEM images of (a) as-received and (b) annealed tungsten foil at a tilt angle of 75°.

tungsten (above 3000 °C). Nevertheless, the surface roughness of the tungsten foil (~ 7 nm) is low compared to as-received, electro-polished and thermally annealed copper foils. Careful examination of Figs. 3-5(b,c) shows that the re-solidified Cu surface is slightly planarized although the RMS roughness is comparable to the annealed tungsten foil surface. The planarization is due to the large copper foil thickness (0.25 mm). As the re-solidified copper surface largely conforms to the underlying tungsten foil surface, the smooth copper surface morphology originating from the smooth tungsten surface is critical to the low nucleation density in graphene growth.

To complement the topological information displayed by AFM images, Figs. 3-6 show the SEM images at a tilt angle of 75° for the different copper surfaces discussed above. Fig. 3-6a shows the rough topography of the as-received copper foil with rolling marks. The annealed solid copper surface in Fig. 3-6b is smoother but still with significant rolling features. Fig. 3-6c shows that mounds are introduced on the copper surface during electrochemical polishing. Electro-polishing planarizes the copper surface better than thermal annealing of solid copper, but cannot completely eliminate rolling marks. The left-over rolling marks and the mounds introduced during polishing contribute to a nucleation density that is still high. Fig. 3-6d shows the melted and re-solidified copper, where visible features originate from the underlying tungsten foil.

The above results show that the Cu surface morphology is one of the most important factors to limit graphene nucleation density. This can be understood from the thermodynamics and kinetics of the growth process. Since precursor adsorption is favorable on surface irregularities,²⁵ the local concentration of active carbon species, which lead to graphene growth, is higher along the rolling marks than in smooth regions. This higher concentration can

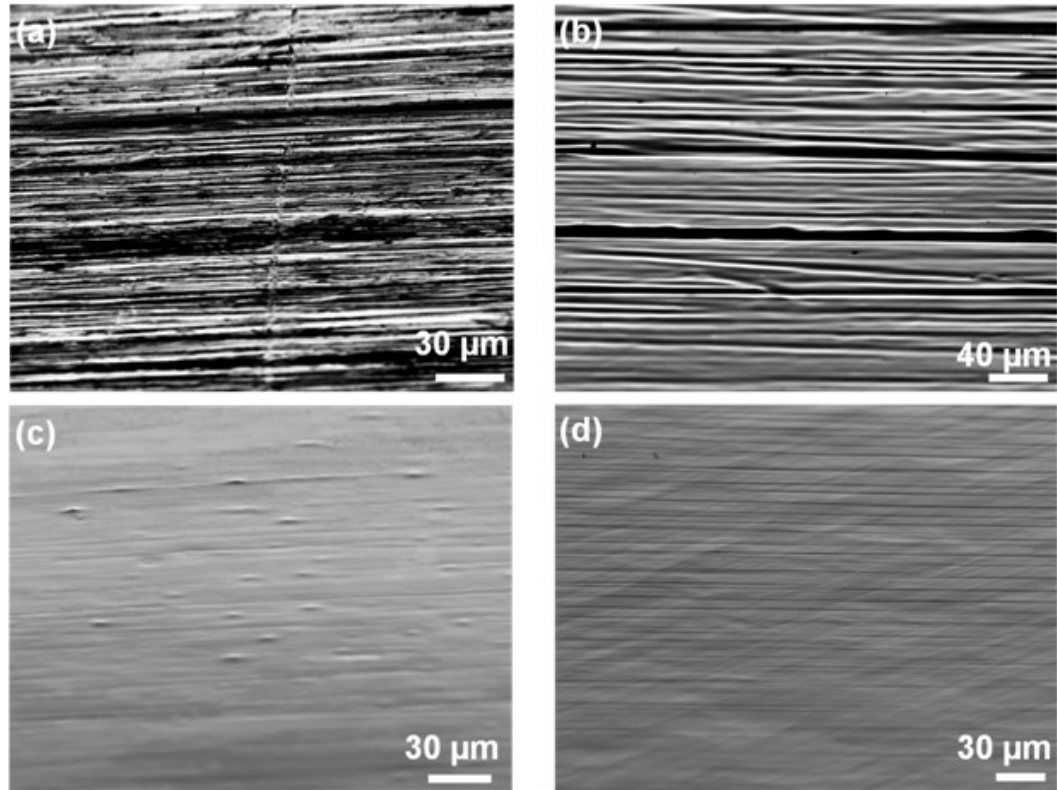


Figure 3-6. SEM images of various copper surfaces at a tilt angle of 75°. (a) As-received foil; (b) Thermally annealed solid copper; (c) Electro-polished foil; (d) Melted and resolidified copper.

overcome the thermodynamic barrier for nucleation,²⁵ leading to a high density of graphene nuclei. Moreover, diffusion of active carbon species is limited in the presence of rolling marks,^{24,26} leading to the formation of multilayer graphene. In contrast, smooth copper surface morphology facilitates surface diffusion,²⁶ resulting in a lower nucleation density on melted and resolidified copper.

To highlight the importance of the melting-resolidification treatment as opposed to merely high-temperature annealing of solid copper, Fig. 3-7a shows graphene domains obtained on copper foils annealed at 1080°C and Fig. 3-7b show graphene domains grown on melted and re-solidified copper. In both cases, graphene growth was carried out at 1075°C for 30 minutes. Figs. 3-7(a,b) indicate that graphene nucleus density/size is higher/smaller for the copper melted at 1080°C compared to 1100°C. At 1080°C, a temperature very close to but below the melting point of bulk copper (1084°C), the copper surface is flowing. This movement removed the majority of the rolling marks but did not eliminate their effect completely. Therefore, the surface is not sufficiently smooth, leading to the still high nucleation density. In contrast, only one large-size hexagonal graphene domain is present in $\sim 1\text{mm}^2$ area on the copper that was melted at 1100°C followed by resolidification.

Figs. 3-7(c,d) compare the effect of growth temperature on nucleation density and grain size on resolidified Cu, with growth time fixed at 30 minutes. Fig. 3-7c shows four graphene nuclei, each $\sim 25\text{ }\mu\text{m}$ in size, in a $\sim 1\text{ mm}^2$ area, typical of the graphene grown at 1050° C on resolidified copper. As the growth temperature increases to 1075° C, only one $\sim 65\text{ }\mu\text{m}$ graphene domain is present in $\sim 1\text{ mm}^2$. This temperature dependence can be explained in the framework of existing graphene nucleation model.²⁴ At the higher temperature, increased desorption rate and capture rate prevents further nucleation after the initial stage, while the increased capture rate

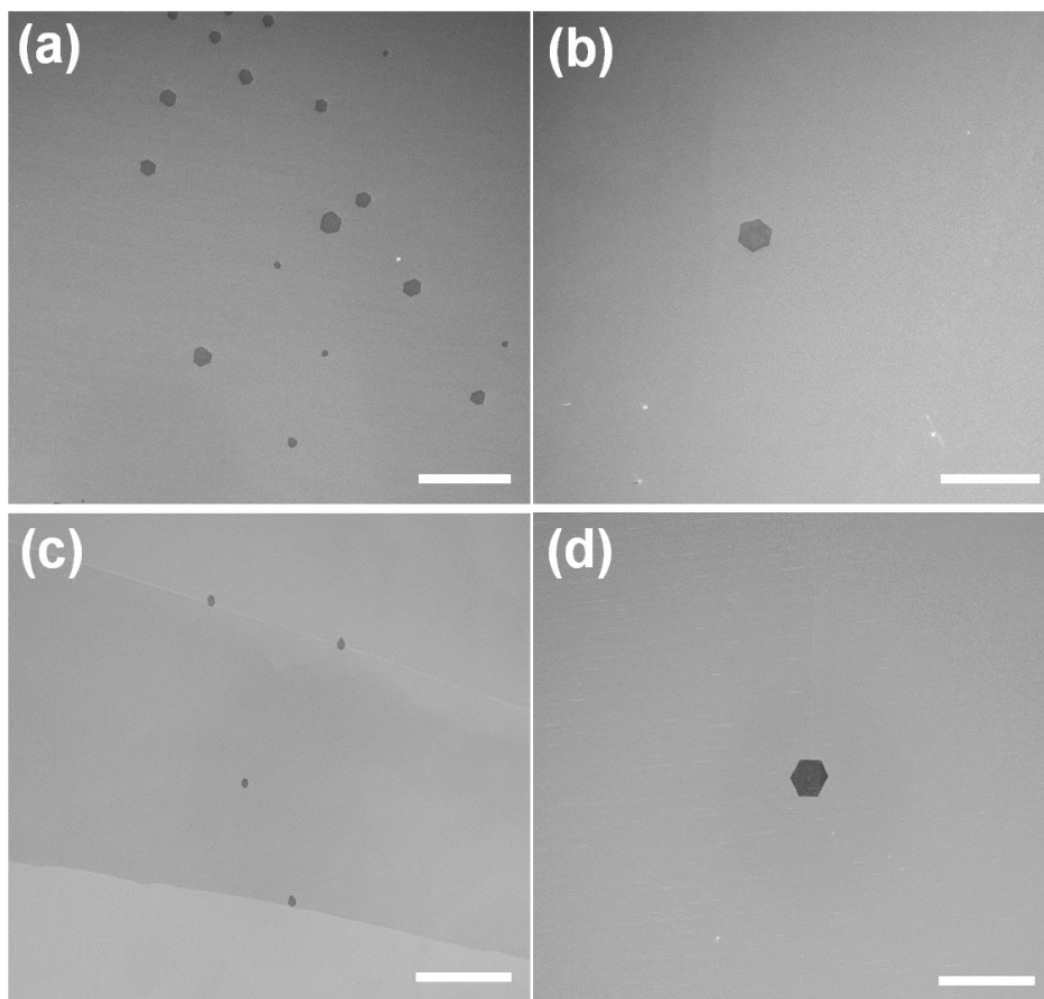


Figure 3-7. Dependence of graphene nucleation density on thermal pretreatment and growth temperature. (a, b) SEM images of graphene on copper foil annealed/melted for 30 min at (a) 1080°C and (b) 1100°C. Growth temperature (1075°C) and growth time (30 min) were kept constant. (c, d) SEM images of the graphene grown at (c) 1050°C and (d) 1075°C. Melting temperature (1100°C) and growth time (30 min) were fixed. Scale bars are 0.2 mm

due to higher carbon species mobility increases growth rate and therefore the grain size grown in a fixed duration. Notice that the partition between the capture- and desorption-controlled regimes in the nucleation density-temperature dependence is very different in APCVD then in LPCVD studied in previous work.²⁴

Hydrogen also plays an important role in graphene synthesis.³ Vlassiouk *et al.* showed that hydrogen acts as both an activator and an etching reagent during graphene growth.⁹ Although the presence of oxygen impurity in commonly used ultrahigh purity (UHP)-grade hydrogen is shown to be necessary for graphene etching,²⁷ the discussion below is independent of the exact chemistry as the O₂ impurity is inevitable unless a hydrogen purifier is incorporated in the CVD system. To gain further insight into the role of hydrogen in our experiments, the hydrogen partial pressure during growth is varied, while keeping synthesis temperature (1075° C), dilute methane flow rate (46 sccm), total flow rate (1000 sccm), and growth time (90 minutes) constant. For three experiments, the hydrogen flow rate is 100 sccm during the first 60 minutes of growth followed by 30 minutes of growth with hydrogen flow rates 80 sccm (Fig. 3-8a), 90 sccm (Fig. 3-8b) and 100 sccm (Fig. 3-8c), respectively.

Comparison of Figs. 3-8(a-c) seems to suggest that it is desirable to accelerate growth after initial nucleation by decreasing hydrogen partial pressure, but careful examination of Fig. 3-8b indicates that secondary graphene domains begin to nucleate when hydrogen flow rate was decreased to 90 sccm and that the size of secondary graphene domains is significantly bigger in Fig. 3-8a, where the hydrogen flow rate was reduced even further to 80 sccm. Hydrogen acts as an etching reagent and thus suppresses secondary nucleation. There is a competition between the growth of existing graphene domains and the formation of secondary nuclei. When the hydrogen flow rate is reduced, the local concentration of active carbon species is high enough that it can

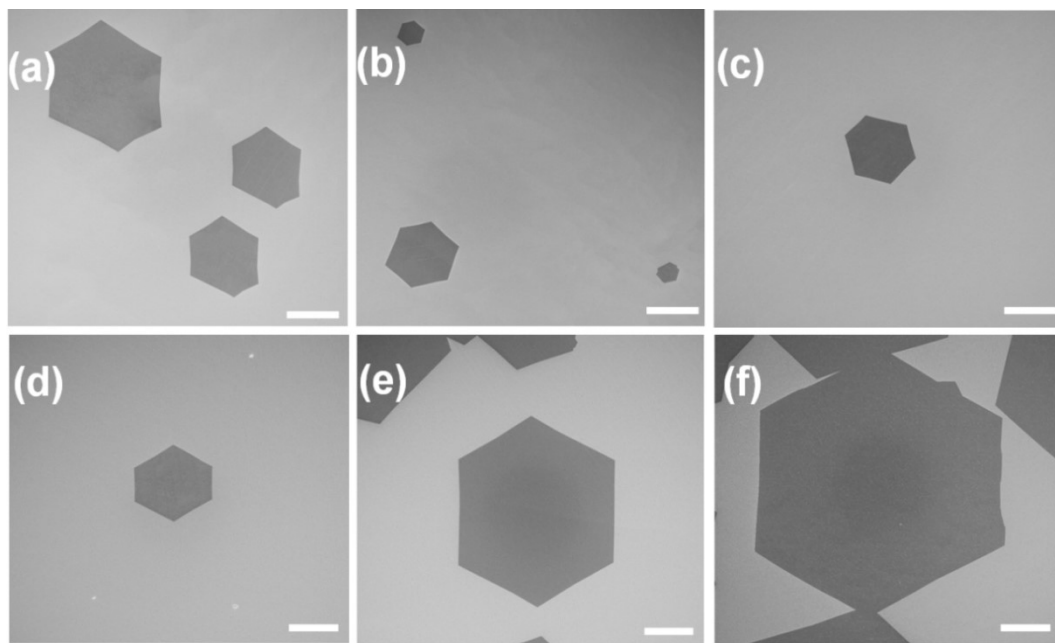


Figure 3-8. Dependence of nucleation density on hydrogen partial pressure and the increase in domain size with growth time. (a-c) SEM images of the graphene crystallites synthesized for 90 minutes, under 100 sccm of hydrogen during the first 60 minutes of growth followed 30 minutes of (a) 80 sccm, (b) 90 sccm, and (c) 100 sccm hydrogen flow. (d-e) Graphene domains grown for (d) 100, (e) 200, and (f) 300 minutes, with a constant hydrogen flow rate (100 sccm). Scale bars are 0.2 mm.

overcome the thermodynamic barrier for nucleation,²⁵ leading to secondary graphene domains. Also, when the hydrogen flow rate is reduced to 80 sccm in Fig. 3-8a, the edges of the primary graphene domain begin to show an increased inward curvature compared to graphene domain obtained in Fig. 3-8c. Due to the formation of secondary graphene nuclei nearby, the effective rate of attachment of carbon species to the primary graphene domain is reduced, resulting in an inward curvature. Notice that the above analysis is not contradictory to previous work,²⁴ where nucleation does not occur after the initial stage due to the competition from capture. Here, the nucleus density is sufficiently low, therefore new nuclei can form, not affected by existing nuclei at distances much longer than the mean travel distance of active carbon species.

Next Figs. 3-8(d,e) show the evolution of graphene domains with time towards millimeter sizes. Synthesis temperature (1075°C), dilute methane flow rate (46 sccm) and hydrogen flow rate (100 sccm) were all kept constant. For growth times 100 minutes (Fig. 3-8d), 200 minutes (Fig. 3-8e), and 300 minutes (Fig. 3-8f), the side-to-side distances for the graphene domains are ~ 0.3 mm, ~ 0.63 mm, and ~ 1 mm, respectively. This largely linear time dependence indicates that the growth velocity of the edge is constant as can be deduced as follows. Growth velocity v of the hexagonal edge can be defined as ²⁸ $v = \frac{1}{L} \frac{dA}{dt}$ where D is the side-to-side distance, S is the length of the edge, $A = (3/2)DS$ is the area and $L = 6S$ is the perimeter of the hexagon, as shown in Fig. 3-9. Hence, $v = \frac{1}{4} \frac{dD}{dt}$. The increase in the size of an existing domain is due to the attachment of carbon atoms to the growth front.^{24,29} Due to the very low nucleus density, there is virtually no competition between nuclei in capturing the active carbon species. Therefore, the increase in a linear dimension of a growing crystallite is simply proportional to the diffusion rate, *i.e.* average, of the active carbon species, which is constant at a fixed temperature.

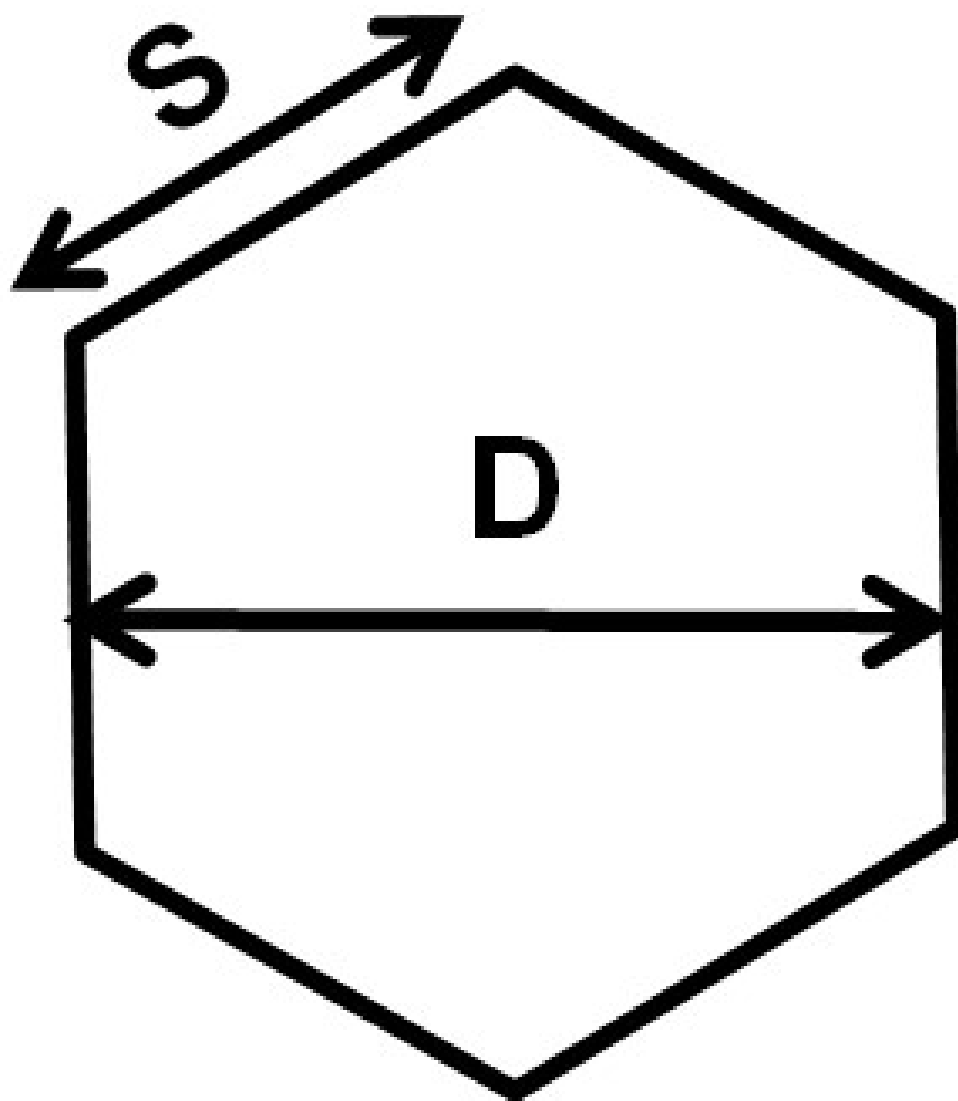


Figure 3-9. Hexagon with important length parameters identified

Raman spectroscopy is an important graphene characterization technique to determine the number of layers, the presence of defects,³⁰ as well as edge types.³¹ Fig. 3-10a shows an optical image of a graphene domain transferred to a 300 nm SiO₂/Si substrate. The color-coded stacked Raman spectra corresponding to the discrete points identified in Fig. 3-10a are shown in Fig. 3-10b. The important peaks, D ($\sim 1322\text{ cm}^{-1}$), G ($\sim 1589\text{ cm}^{-1}$) and 2D ($\sim 2646\text{ cm}^{-1}$) agree well with the literature.^{32,33} The excellent consistency of these spectra indicates the uniformity of our synthesized domains. The 2D to G peak intensity ratio ($I_{2D}/I_G > 2$), the position of the 2D peak ($\sim 2646\text{ cm}^{-1}$) and the full width half maximum (FWHM) of the 2D peak ($\sim 33\text{ cm}^{-1}$), suggests that the graphene crystallite is a monolayer.^{34,35} The high G to D peak intensity ratio (I_G/I_D) above ~ 10 at all spots including spots 3 and 4 at corners indicates high quality as well as zigzag edge termination of the graphene domain.³¹ Two very weak peaks at 1448 cm^{-1} and 1529 cm^{-1} are due to polymethyl methacrylate (PMMA) residue introduced during the transfer step;³⁶ their absolute intensities are very small compared to the G peak. To further reveal the spatial uniformity of the transferred graphene, the mappings of I_{2D}/I_G , FWHM and position of the 2D peak, and I_G/I_D are shown in Figs. 3-10(c-f). The mean values of 2D the peak position ($\sim 2650\text{ cm}^{-1}$), I_{2D}/I_G ratio (>2), and 2D peak FWHM ($\sim 25\text{ cm}^{-1}$) indicate that the synthesized domain is uniformly monolayer.^{34,35} High average G to D peak intensity ratio (~ 100), along with its uniformity throughout the crystallite, indicates that the zigzag edges are of same high quality as the center of the graphene domain.

To demonstrate the single-crystal, of the synthesized graphene crystallites on re-solidified copper, SAED results are presented next. An SEM image of a graphene domain transferred onto transmission electron microscope (TEM) grid is shown in Fig. 3-11a, where the edges of the graphene domain are identified by dashed lines. SAED patterns at random location of the

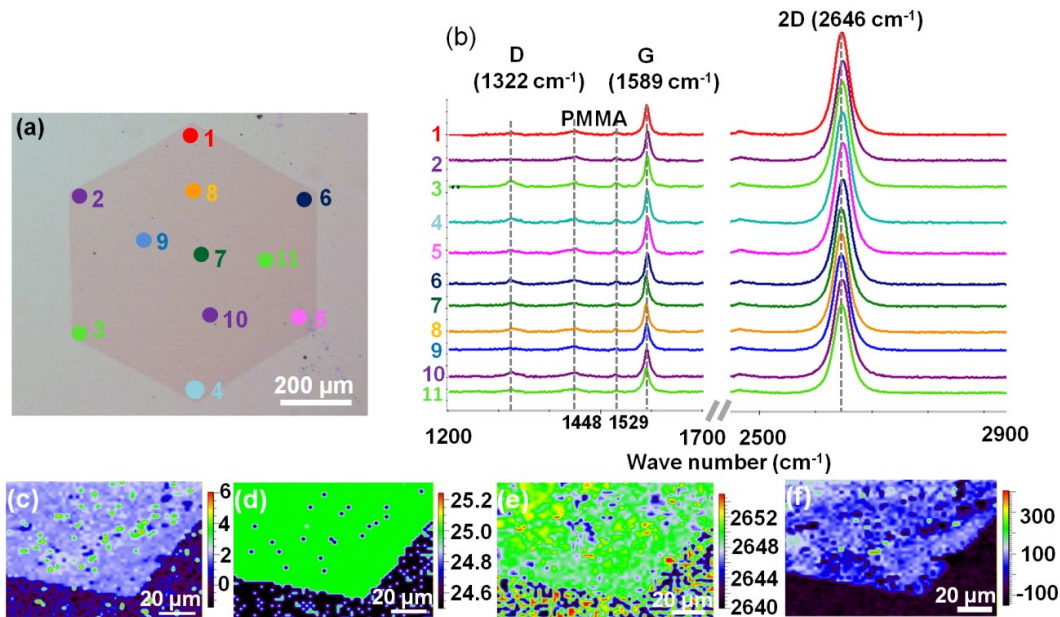


Figure 3-10. Raman characterization. (a) Optical image of the graphene crystallite transferred to a 300 nm SiO₂/Si substrate. (b) Color-coded stacked Raman spectra corresponding to the spots identified in (a). (c) 2D to G peak intensity ratio (I_{2D}/I_G), (d) FWHM of the 2D peak, (e) Position of the 2D peak, and (f) G to D peak intensity ratio (I_G/I_D) maps of another crystallite.

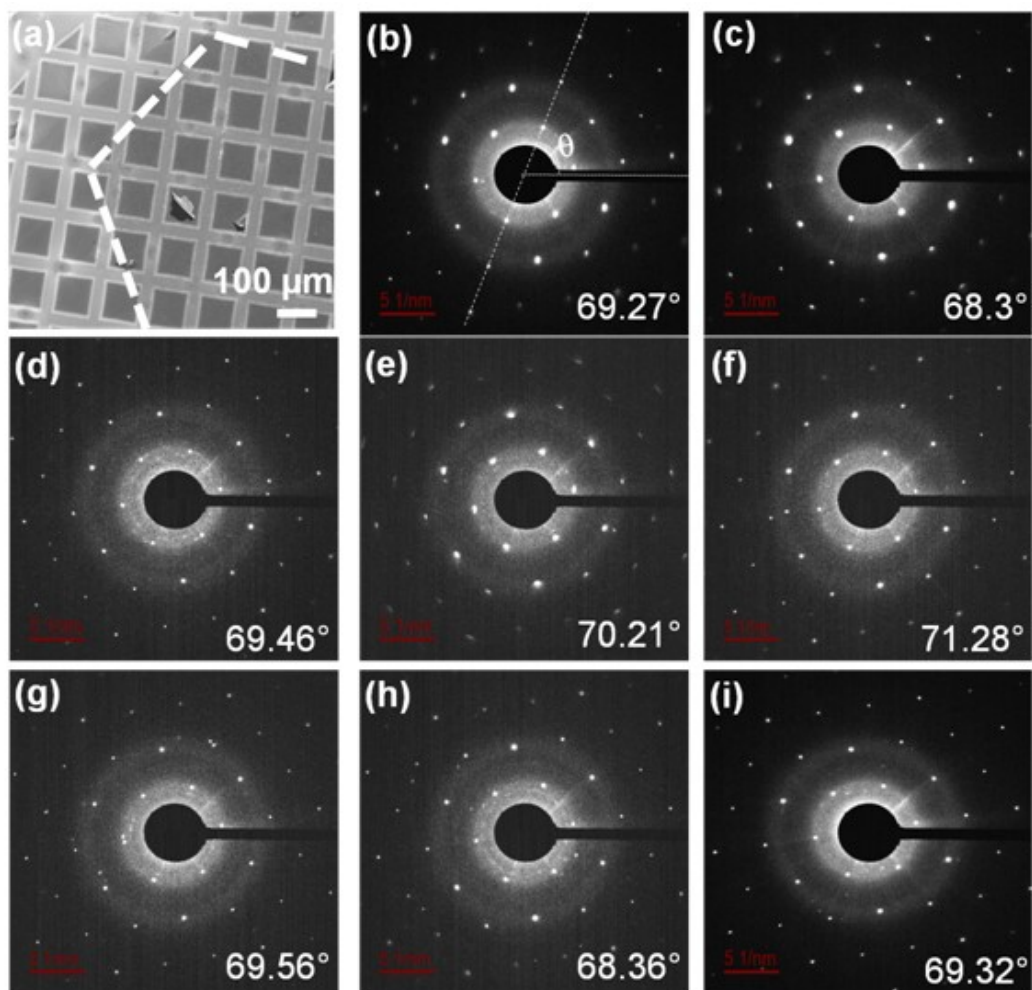


Figure 3-11. SAED characterization. (a) SEM image of the graphene domain transferred onto a TEM grid. The edges of the domain are delineated by dashed lines. (b-i) SAED patterns taken in different windows of the TEM grid.

graphene domain on TEM grid are acquired, including those near the edges and near the center of the graphene domain. Eight representative patterns are shown in Figure 3-11(b-i). Hexagonal diffraction spots confirm the presence of graphene.^{14,15,16,17,18} To quantify the rotation of the graphene lattice at each location, an angle θ is defined as shown in Fig. 3-11b. The less than 3° maximum variation shows the single-crystal nature of the graphene domain.

3.4 Conclusion

A simple method for the growth of millimeter-size, single-crystal, monolayer graphene domains, on commercial metal foils is devised in this study, that only requires brief *in situ* treatment of the substrate at atmospheric pressure. The nucleation density, a key factor in obtaining large size single crystal domains, strongly depends on the copper surface morphology. Thermal annealing below the copper melting point or electro-polishing cannot effectively eliminate surface irregularities, therefore the nucleation density remains high after both treatments. When copper is melted and then re-solidified on a tungsten foil, a smooth surface is obtained resulting in a significant reduction in nucleation density. A relatively high growth temperature results in an increased desorption of active carbon species, which further reduces the nucleation density. Hydrogen partial pressure is also critical since hydrogen suppresses secondary nucleation, which competes against existing nucleus growth, and therefore skews the competition towards the latter. Raman spectroscopy indicates that the graphene domains obtained are single layered with negligible defects and zigzag edge terminations. Moreover, SAED patterns confirm the single-crystal natures of the synthesized domains.

3.5 Experimental methods

3.5.1 Graphene synthesis

High purity commercial copper foils (99.999%, 0.25 mm thick, Alfa- Aesar) and tungsten foils (99.95%, 0.05 mm thick, Alfa-Aesar) were used. The gases used in this research were of ultra-high purity (UHP) grade supplied by Airgas. Dilute methane (0.1%) balanced with argon was used as the carbon precursor. The growth was performed in a commercial CVD reactor (OTF-1200X-80-II-4CV-PE-SL, MTI) with a 2 in. diameter processing tube. Before growth, copper foils were dipped in dilute nitric acid and DI water for 20 seconds each and gently dried with a nitrogen gun. The copper foil was then placed on a tungsten foil and loaded into the quartz tube. The whole CVD system was then pumped down to the base pressure and then back-filled with argon and hydrogen. This procedure was repeated twice to minimize air residue in the subsequent growth process. After bringing the processing tube to atmospheric pressure, hydrogen and argon flow rates were adjusted to 60 sccm and 940 sccm, respectively. The temperature was first ramped up to 1000°C in 50 minutes and then to 1100°C in 10 minutes. The temperature was kept constant for 30 minutes and then slowly ramped down (1°C/minute) to 1075°C. After temperature stabilization for 10 minutes, dilute methane was introduced at a flow rate of 46 sccm and hydrogen and argon flow rates were changed to 100 sccm and 854 sccm, respectively. After the growth, the furnace was cooled without changing the gas flows. The sample was unloaded below 80°C under argon and hydrogen flow. To make graphene domains visible, the substrate was heated at 300°C on a hot plate for 2 minutes. For electro-polishing, the as-received copper foil was used as the cathode in a home-built electrochemical cell, while another piece of copper foil was used as the anode. Ortho-phosphoric acid (85%, Sigma-Aldrich) was used as an electropolishing solution and foils were polished at a DC voltage of 5V for 30

minutes.

3.5.2 Characterization

For Raman characterization graphene was transferred onto 300 nm SiO₂/Si substrate using PMMA.¹ Immediately after spin coating PMMA at 4000 rpm for 60 seconds, the substrate was then baked at 160°C for 10 minutes on a hot plate. Tungsten was then etched away by a tungsten etchant (Tungsten etch TFW, Transene company) and copper was removed by a copper etchant (APS-100, Transene company). The membrane was then transferred to a clean SiO₂/Si substrate and PMMA was removed by subsequent dipping in acetone (~ 4 hours) and chloroform (overnight) at room temperature. For SAED characterization, a graphene/PMMA membrane was scooped onto a TEM grid (Quantifoil) directly. The PMMA was then removed by thermal annealing at 370°C for 2 hours in 100 sccm of hydrogen and 1000 sccm of argon.

Scanning electron microscope images were acquired using an LEO 1525 SEM operated at 5 kV. SAED patterns were obtained using a Zeiss Libra 200 MC TEM operated at 200 kV. Raman spectra were recorded using a Renishaw confocal Raman microscope with 633nm laser excitation. Atomic force microscopy (Asylum, Oxford Instruments) was carried out in the tapping mode in the air at room temperature.

3.6 References

- (1) Li, X.; Cai, W.; An, J.; Kim, S.; Nah, J.; Yang, D.; Piner, R.; Velamakanni, A.; Jung, I.; Tutuc, E. *et al.* Large-Area Synthesis of High-quality and Uniform Graphene Films on Copper Foils. *Science* **2009**, *324*, 1312–1314.
- (2) Huang, P. Y.; Ruiz-Vargas, C. S.; Zande, A. M. van der; Whitney, W. S.; Levendorf, M. P.; Kevek, J. W.; Garg, S.; Alden, J. S.; Hustedt, C. J.; Zhu, Y. *et al.* Grains and Grain Boundaries in Single-Layer Graphene Atomic Patchwork Quilts. *Nature* **2011**, *469*, 389–392
- (3) Mattevi, C.; Kim, H.; Chhowalla, M. A Review of Chemical Vapour Deposition of Graphene on Copper. *J. Mater. Chem.* **2011**, *21*, 3324–3334.
- (4) Li, X.; Cai, W.; Colombo, L.; Ruoff, R. S. Evolution of Graphene Growth on Ni and Cu by Carbon Isotope Labeling. *Nano Lett.* **2009**, *9*, 4268–4272
- (5) Yu, Q.; Jauregui, L. A; Wu, W.; Colby, R.; Tian, J.; Su, Z.; Cao, H.; Liu, Z.; Pandey, D.; Wei, D. *et al.* Control and Characterization of Individual Grains and Grain Boundaries in Graphene Grown by Chemical Vapour Deposition. *Nat. Mater.* **2011**, *10*, 443–449.
- (6) Tsen, A. W.; Brown, L.; Levendorf, M. P.; Ghahari, F.; Huang, P. Y.; Havener, R. W.; Ruiz-Vargas, C. S.; Muller, D. A; Kim, P.; Park, J. Tailoring Electrical Transport Across Grain Boundaries in Polycrystalline Graphene. *Science* **2012**, *336*, 1143–1146.
- (7) Yu, Q.; Jauregui, L. A; Wu, W.; Colby, R.; Tian, J.; Su, Z.; Cao, H.; Liu, Z.; Pandey, D.; Wei, D. *et al.* Control and Characterization of Individual Grains and Grain Boundaries in Graphene Grown by Chemical Vapour Deposition. *Nat. Mater.* **2011**, *10*, 443–449.

- (8) Robertson, A. W.; Warner, J. H. Hexagonal Single Crystal Domains of Few-Layer Graphene on Copper Foils. *Nano Lett.* **2011**, *11*, 1182–1189.
- (9) Vlassiounk, I.; Regmi, M.; Fulvio, P.; Dai, S.; Datskos, P.; Eres, G.; Smirnov, S. Role of Hydrogen in Chemical Vapor Deposition Growth of Large Single-Crystal Graphene. *ACS Nano* **2011**, *5*, 6069–6076.
- (10) Wu, B.; Geng, D.; Guo, Y.; Huang, L.; Xue, Y.; Zheng, J.; Chen, J.; Yu, G.; Liu, Y.; Jiang, L. *et al.* Equiangular Hexagon-Shape-Controlled Synthesis of Graphene on Copper Surface. *Adv. Mater.* **2011**, *23*, 3522–3525.
- (11) Luo, Z.; Kim, S.; Kawamoto, N.; Rappe, A. M.; Johnson, A. T. C. Growth Mechanism of Hexagonal-Shape Graphene Flakes with Zigzag Edges. *ACS Nano* **2011**, *5*, 9154–9160.
- (12) Wu, W.; Jauregui, L. A.; Su, Z.; Liu, Z.; Bao, J.; Chen, Y. P.; Yu, Q. Growth of Single Crystal Graphene Arrays by Locally Controlling Nucleation on Polycrystalline Cu Using Chemical Vapor Deposition. *Adv. Mater.* **2011**, *23*, 4898–4903.
- (13) Tian, J.; Cao, H.; Wu, W.; Yu, Q.; Chen, Y. P. Direct Imaging of Graphene Edges: Atomic Structure and Electronic Scattering. *Nano Lett.* **2011**, *11*, 3663–3668.
- (14) Wang, H.; Wang, G.; Bao, P.; Yang, S.; Zhu, W.; Xie, X.; Zhang, W.-J. Controllable Synthesis of Submillimeter Single-Crystal Monolayer Graphene Domains on Copper Foils by Suppressing Nucleation. *J. Am. Chem. Soc.* **2012**, *134*, 3627–3230.
- (15) Yan, Z.; Lin, J.; Peng, Z.; Sun, Z.; Zhu, Y.; Li, L.; Xiang, C.; Samuel, E.L.; Kittrell, C.; Tour, J.M. Toward the Synthesis of Wafer-Scale Single-Crystal Graphene on Copper Foils. *ACS*

Nano **2012**, *6*, 9110–9117.

(16) Chen, S.; Ji, H.; Chou, H.; Li, Q.; Li, H.; Suk, J. W.; Piner, R.; Liao, L.; Cai, W.; Ruoff, R. S. Millimeter-Size Single-Crystal Graphene by Suppressing Evaporative Loss of Cu During Low Pressure Chemical Vapor Deposition. *Adv. Mater.* **2013**, *25*, 2062–2065.

(17) Geng, D.; Wu, B.; Guo, Y.; Huang, L.; Xue, Y.; Chen, J.; Yu, G.; Jiang, L.; Hu, W.; Liu, Y. Uniform Hexagonal Graphene Flakes and Films Grown on Liquid Copper Surface. *Proc. Natl. Acad. Sci. USA* **2012**, *109*, 7992–7996.

(18) Wu, Y.A.; Fan, Y.; Speller, Creeth, G.L.; Sadowski, J.T.; He, K.; Robertson, A.W. Large Single Crystals of Graphene on Melted Copper Using Chemical Vapor Deposition. *ACS Nano* **2012**, *6*, 5010–5017.

(19) Paronyan, T. M.; Pigos, E. M.; Chen, G.; Harutyunyan, A. R. Formation of Ripples in Graphene as a Result of Interfacial Instabilities. *ACS Nano* **2011**, *5*, 9619–9627.

(20) Gan, L.; Luo, Z. Turning off Hydrogen To Realize Seeded Growth of Subcentimeter Single-Crystal Graphene Grains on Copper. *ACS Nano*, **2013**, *7*, 9480–9488.

(21) Hao, Y.; Bharathi, M. S.; Wang, L.; Liu, Y.; Chen, H.; Nie, S.; Wang, X.; Chou, H.; Tan, C.; Fallahazad, B.; *et al.* The Role of Surface Oxygen in the Growth of Large Single-Crystal Graphene on Copper. *Science* **2013**, *342*, 720–723.

(22) Wu, T.; Zhang, X.; Yuan, Q.; Xue, J.; Lu, G.; Liu, Z.; Wang, H.; Wang, H.; Ding, F.; Yu, Q.; *et al.* Fast Growth of Inch-Sized Single-Crystalline Graphene from a Controlled Single Nucleus on Cu–Ni Alloys. *Nat. Mater.* **2015**, *15*, 43–47.

- (23) Kidambi, P. R.; Ducati, C.; Dlubak, B.; Gardiner, D.; Weatherup, R. S.; Martin, M.-B.; Seneor, P.; Coles, H.; Hofmann, S. The Parameter Space of Graphene Chemical Vapor Deposition on Polycrystalline Cu. *J. Phys. Chem. C* **2012**, *116*, 22492–22501
- (24) Kim, H.; Mattevi, C.; Calvo, M.; Oberg, J. Activation Energy Paths for Graphene Nucleation and Growth on Cu. *ACS Nano* **2012**, *6*, 3614–3623.
- (25) Ohring, M. *The Material Science of Thin Films*; Academic Press: New York, 1992.
- (26) Luo, Z.; Lu, Y.; Singer, D. W.; Berck, M. E.; Somers, L. A.; Goldsmith, B. R.; Johnson, A. T. C. Effect of Substrate Roughness and Feedstock Concentration on Growth of Wafer-Scale Graphene at Atmospheric Pressure. *Chem. Mater.* **2011**, *23*, 1441-1447
- (27) Choubak, S.; Biron, M.; Levesque, P. L.; Martel, R.; Desjardins, P. No Graphene Etching in Purified Hydrogen. *J. Phys. Chem. Lett.* **2013**, *4*, 1100–1103.
- (28) Loginova, E.; Bartelt, N. C.; Feibelman, P. J.; McCarty, K. F. Evidence for Graphene Growth by C Cluster Attachment. *New J. Phys.* **2008**, *10*, 093026.
- (29) Luo, Z.; Kim, S.; Kawamoto, N.; Rappe, A. M.; Johnson, A. T. C. Growth Mechanism of Hexagonal-Shape Graphene Flakes with Zigzag Edges. *ACS Nano* **2011**, *5*, 9154–9160.
- (30) Ferrari, A. C.; Meyer, J. C.; Scardaci, V.; Casiraghi, C.; Lazzeri, M.; Mauri, F.; Piscanec, S.; Jiang, D.; Novoselov, K. S.; Roth, S. *et al.* Raman Spectrum of Graphene and Graphene Layers. *Phys. Rev. Lett.* **2006**, *97*, 1–4.
- (31) Almeida, C. M.; Carozo, V.; Prioli, R.; Achete, C. A. Identification of Graphene Crystallographic Orientation by Atomic Force Microscopy. *J. Appl. Phys.* **2011**, *110*, 086101.

- (32) Vidano, R. B.; Fischbach D.B. Observation of Raman Band Shifting with Excitation Wavelength For Carbons and Graphites. *Solid. State. Comm.* **1981**, *39*, 341-344.
- (33) Malard, L. M.; Pimenta, M. A.; Dresselhaus, G.; Dresselhaus, M. S. Raman Spectroscopy in Graphene. *Phys. Rep.* **2009**, *473*, 51–87.
- (34) Lenski, D. R.; Fuhrer, M. S. Raman and Optical Characterization of Multilayer Turbostratic Graphene Grown *via* Chemical Vapor Deposition. *J. Appl. Phys.* **2011**, *110*, 013720.
- (35) Lee, D. S.; Riedl, C.; Krauss, B.; von Klitzing, K.; Starke, U.; Smet, J. H. Raman Spectra of Epitaxial Graphene on SiC and of Epitaxial Graphene Transferred to SiO₂. *Nano Lett.* **2008**, *8*, 4320–4325
- (36) Lin, Y.-C.; Jin, C.; Lee, J.-C.; Jen, S.-F.; Suenaga, K.; Chiu, P.-W. Clean Transfer of Graphene for Isolation and Suspension. *ACS Nano* **2011**, *5*, 2362–2368.

CHAPTER 4

EXPERIMENTALLY DETERMINED EDGE ORIENTATION OF TRIANGULAR CRYSTALS OF HEXAGONAL BORON NITRIDE

This chapter is a slightly modified version of the paper with the same title published in *Physica Status Solidi B* in April 2017 by Ali Mohsin, Nicholas G. Cross, Lei Liu, Peizhi Liu, Gerd Duscher, and Gong Gu. The introduction in this chapter has been expanded to cover literature review about the growth of triangular crystals of h-BN. Also, the supporting information in the published paper has been included as a part of the main text in this chapter.

All the figures and most of the text in this chapter are reproduced with permission from Mohsin, A.; Cross, N. G.; Liu, L.; Liu, P.; Duscher, G.; Gu, G. Experimentally Determined Edge Orientation Of Triangular Crystals Of Hexagonal Boron Nitride. *Phys. Stat. Solidi. B* **2017**, 254, 1700069. Copyright 2017 Wiley-VCH Verlag GmbH & Co. KGaA, Weinheim.

As a first author of the paper, I was responsible for (1) Designing of the experiments for the CVD growth of h-BN crystals. (2) Optimization of the growth parameters. (3) Characterization of h-BN crystals by Raman. (4) Transfer of the h-BN crystals onto the TEM grids for further characterization. (5) Data analysis and writing of the manuscript. L. L. assembled the CVD system on which CVD growth experiments were carried out. N.G.C and P.L. carried out the STEM characterization of the h-BN crystals under the supervision of G.D. G.G. proposed the experimental scheme and oversaw the research.

4.1 Abstract

This work demonstrates a method to directly determine edge orientations of three-fold symmetric two-dimensional crystals in real space, without resolving the edge structure. In an annular dark-field scanning transmission electron microscope, the orientation of an edge is derived from the overall edge direction recorded at a low magnification and the crystal orientation revealed by atomic resolution, element-contrast imaging at a high magnification. By applying this method,

the edge orientation of equilateral triangle-shaped hexagonal boron nitride (h-BN) crystals grown by chemical vapor deposition on Cu is experimentally determined for the first time. The experimentally determined nitrogen-terminated zigzag edges validate the kinetic theory of h-BN crystal growth, which is a useful case study of the growth of 2D crystals lacking inversion symmetry.

4.2 Introduction

Crystal shape and surface orientation manifest the interplay between the thermodynamics and growth kinetics of the crystal, following principles that have been illustrated with fictitious two-dimensional (2D) crystals as pedagogical models for easy visualization.¹ The advent of real 2D crystals enables experimental investigation of real 2D models, leveraging facile visualization of 2D crystals by conventional and advanced microscopy,² in principle allowing for experimental determination of edge orientations. Furthermore, an interface formed by heteroepitaxy on a crystalline substrate surface may exhibit novel physics determined by the orientation of the interface.^{3,4} Similarly, in the case of epitaxy in two dimensions, specific orientations of the 1D interface can also lead to unique properties. For example, the zigzag-oriented interface between graphene and hexagonal boron nitride (h-BN) is predicted to be spin polarized.^{5,6} In order to realize such predicted peculiar properties, it is important to determine the orientations of the starting 2D crystal edges, which turns into the 1D interface upon heteroepitaxial growth.

After graphene single crystals were grown on copper,⁷ Kim *et al.* demonstrated the LPCVD growth of equilateral triangle-shaped monolayer h-BN crystals on copper, using Ammonia-Borane (AB) complex as a precursor.⁸ Interestingly, the authors showed that by increasing the temperature of the precursor source, the triangular h-BN islands evolved into different shapes.⁸ Using AB as a precursor source, Guo *et al.* developed a more controlled way to

grow triangular crystals of few layers (1-4) h-BN exclusively, by LPCVD.⁹ The authors loaded the copper foil in a small quartz tube closed at one end.⁹ Since the closed end of the small quartz tube faced the precursor, the later diffused slowly from the open end of the small tube to reach the copper foils, allowing slower growth of h-BN.⁹ Tay *et al.* demonstrated the APCVD growth of h-BN on copper, using AB as a precursor.¹⁰ The authors studied the growth parameters in detail and found that precursor temperature of 60°C was sufficient to growth monolayer triangular islands of h-BN, while further increase in the precursor temperature resulted in the growth of h-BN islands with more complex and irregular shapes,¹⁰ consistent with the observation of Kim *et al.*⁸ Han *et al.* revealed that during the growth of monolayer h-BN triangles on copper using AB as a precursor source, nanoparticles of poly-aminoborane (BH₂NH₂) accumulate at the edges of individual triangles that are generated as the precursor is heated and carried away into the high-temperature zone of furnace.¹¹ By enclosing the precursor in a filter, which traps the nanoparticles liberated by the heated precursor, the authors demonstrated the growth of monolayer h-BN free of nanoparticles.¹¹ In all the previous studies mentioned so far, the individual domain size of monolayer h-BN triangle was limited to below 5µm.^{8,9,10,11} Wang *et al.* found that by ramping up the temperature of pre-annealed copper foils in argon environment only during LPCVD, resulted in the reduced nucleation density of monolayer h-BN islands.¹² This procedure allowed the growth of triangular monolayer h-BN up to 20 µm in lateral dimensions.¹² Tay *et al.* showed that electropolishing of copper before APCVD growth resulted in an order of magnitude reduction in the nucleation density of h-BN islands on copper.¹³ This reduced island density allowed the growth of triangular h-BN crystals with dimensions up to 35µm.¹³ Interestingly, the authors observed the growth of hexagonal domains of h-BN on some regions of copper foils as well, which had never been observed experimentally

before.¹³ The authors attributed this observation to an increased diffusion of B, N radicals on the smooth copper surface after electropolishing, along with an increased content of surface oxygen on copper foil caused by the phosphoric acid solution during electropolishing.¹³ Both of these factors changed the growth kinetics of h-BN, by allowing the B, N radicals to attach to existing edges of h-BN, irrespective of their polarity.¹³ Lu *et al.* demonstrated the LPCVD growth of triangular monolayer of h-BN up to 90 μ m on a copper-nickel alloy of an optimized composition.¹⁴ The authors also observed white particles of poly-amino borane accumulating at the edges of monolayer h-BN crystals,¹⁴ consistent with the observation of Han *et al.*¹¹ The authors conclude that the presence of those nanoparticles is the main culprit in the higher nucleation density of h-BN on copper, as those poly-amino borane nanoparticles cannot be converted to h-BN at the temperature of 1050°C, used in that study.¹⁴ A controlled amount of a stronger catalyst i.e. Ni, helps to decompose those nanoparticles which result in either desorption of B, N radicals or the formation of strong Ni-B or Ni-N bonds, with an overall result that the nucleation density of monolayer h-BN crystals is greatly reduced.¹⁴ Song *et al.* demonstrated LPCVD growth of wafer-scale films of monolayer h-BN on copper, consisting of triangular h-BN islands, up to 72 μ m in lateral dimensions.¹⁵ The author used a copper foil enclosure approach,¹⁶ which not only results in a smooth inner surface of foil due to reduced evaporation of copper under lower pressure environment at the higher growth temperature but also slows down the diffusion of precursors reaching the inner copper surface, effectively lowering the nucleation density.¹⁵ Wu *et al.* found that by pre-annealing the copper foils for 2-3 hours in argon environment only, and then carrying out the growth in a mixed argon and hydrogen environment, resulted in the growth of monolayer triangular h-BN islands, with lateral dimensions exceeding 100 μ m.¹⁷ The authors hint that the presence of a trace of oxygen during argon annealing only

might have changed the surface morphology of copper foil, that helped in the reduction of nucleation density of h-BN, the exact mechanism, however, remains unclear.¹⁷ Recently Stehle *et al.* studied the shape evolution of monolayer h-BN crystals on copper and found that shape of h-BN crystals evolve from triangles to truncated triangles and even hexagons, depending upon the position and distance of copper foil from the precursor source.¹⁸ The authors attribute this evolution in the shape of h-BN crystals to the variation in the atomic ratios of B and N species, from the upstream end of the quartz tube to the downstream end.¹⁸

Based on the first-principles calculation result that the edge energy is the lowest for the N-terminated zigzag edge,¹⁹ Kim *et al.* suggested that the edges of the equilateral triangle-shaped 2D crystals were zigzag with nitrogen termination.⁸ Later reports of CVD-grown, equilateral triangle-shaped monolayer h-BN crystals on copper all assumed N-terminated zigzag edges,^{9,10,11,12,13,14,15,17,18} citing Kim *et al.*⁸ The edge orientation of these triangular crystals has nevertheless not been experimentally verified. Crystal growth is intrinsically a nonequilibrium process, therefore crystal shape and edge orientation may be dominated by process kinetics and deviate from the equilibrium picture. Indeed, more recent theory work²⁰ points out that the equilibrium shape under common growth conditions calculated by edge energy minimization is not the experimentally observed triangle. Also recently, the growth of h-BN crystals with shapes other than regular triangles, e.g., truncated triangles^{13,21} or hexagons^{13,18,21} has been reported, again different from the equilibrium shapes.¹⁹ By considering kinetics under various conditions, Zhang *et al.* reproduced all experimentally observed h-BN crystal shapes on Cu.²⁰ According to the new kinetic theory,²⁰ the sides of CVD grown equiangular triangle h-BN crystals on Cu are N-terminated zigzag edges, but the reason is not edge energy minimization. To fully verify the theory, a method to determine orientations of all edges, especially the short and long edges of the

truncated triangles, is highly desirable.

Here, by leveraging the elemental contrast (Z contrast) and atomic resolution of the annular dark-field scanning transmission electron microscope (ADF STEM),²² we validate for the first time that the edges of equilateral triangle-shaped h-BN crystals grown by CVD on copper under the widely used condition are indeed zigzag-oriented with N termination. The exact atomic structure of edges may undergo reconstructions, e.g. in the case of zigzag-edges of graphene²³ that can change reversibly under the electron beam in the STEM,²⁴ and hence is not the focus of this work. Instead, we acquire overview STEM images of an h-BN crystal to locate edges, and combine this information with the atomically resolved, Z -contrast images of the interior, or “bulk”, of the 2D crystal, to deduce the edge orientations; N- and B- terminated zigzags without detailed atomic structures (reconstructions) are regarded as edge orientations 180° apart from each other. This study not only verifies the theoretical prediction²⁰ but also justifies the assumed edge orientations of h-BN in our earlier work on the van der Waals epitaxy of h-BN on Cu(100).²⁵ The method used can also be applied to resolve the edge orientations of other 2D crystals such as transition metal dichalcogenides.

4.3 Results and discussion

Due to the fragile nature and reactivity of 2D crystal edges in general, it is very challenging to preserve the atomic structure of the edges during transfer from the copper foil substrate and subsequently resolve the structure by microscopy. This is depicted in Fig. 4-1a, which shows an overview STEM image of a CVD grown graphene. The graphene was grown by CVD on copper⁷ foil and transferred by a PMMA-assisted²⁶ procedure. Fig. 4-1b shows a zoomed-in image of Fig. 4-1a. While the exact edge atomic structure, obscured by contamination that tends to accumulate

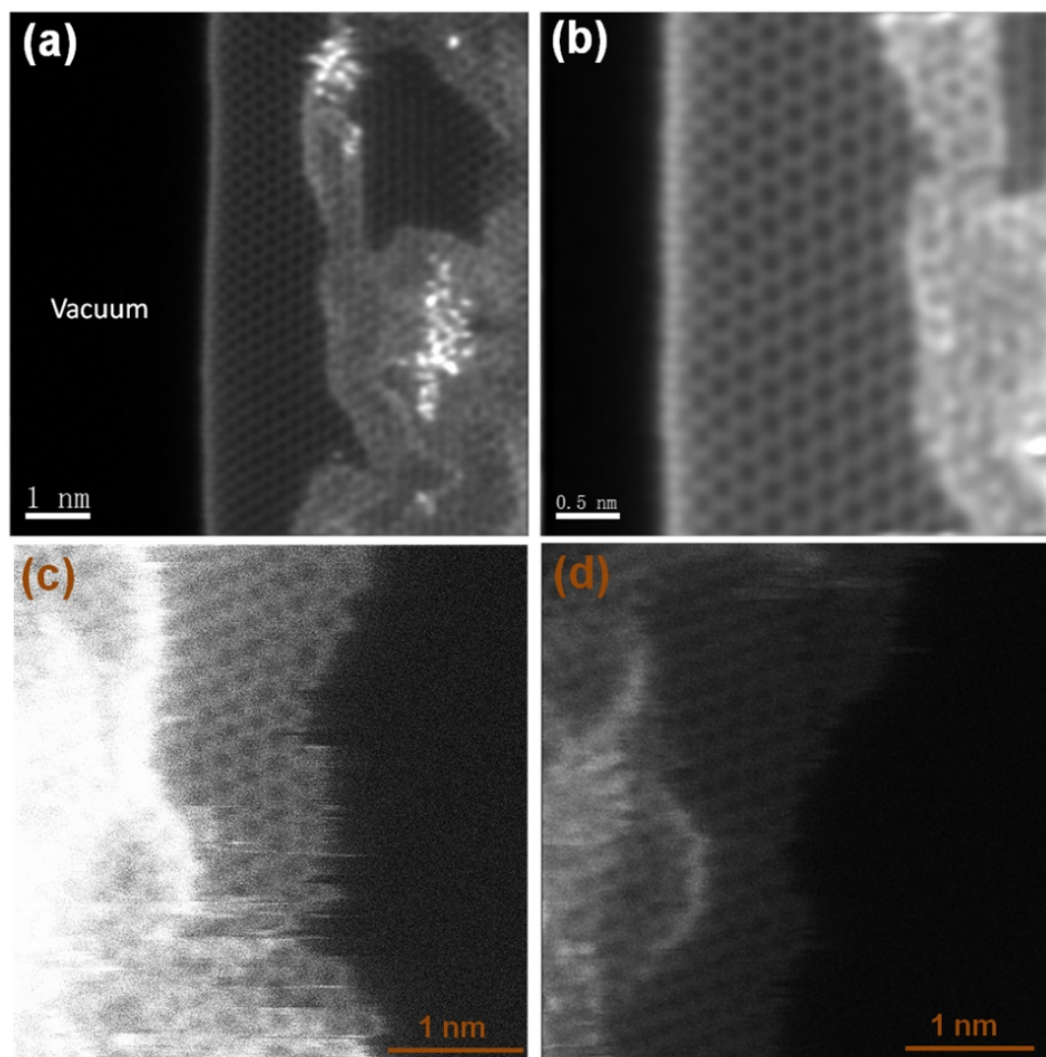


Figure 4-1. STEM images of suspended graphene edges. (a) Overview image showing an edge of a PMMA transferred graphene island. While the PMMA-assisted transfer maintains the integrity of the edge, but the edge itself is covered by contamination. (b) Zoomed-in image of panel a. (c) Overview STEM image showing an edge of a direct transferred graphene island. With direct transferred, although the edges are cleaner, but the structural integrity of the as-grown edge is lost.

on edges and possibly reconstructed,²⁴ cannot be resolved, the atomic resolution image unambiguously reveals the bulk orientation and therefore the edge orientation. In order to reduce contamination introduced by PMMA-assisted transfer,²⁶ Figs. 4-1(c,d) shows the STEM images of CVD grown graphene that was direct-transferred²⁷ onto a TEM grid. While the edges tend to be relatively cleaner compared to PMMA-assisted graphene in Figs. 4-1(a,b), but the suspended edges are broken, and orientations of as-grown edges are not preserved.

Fig. 4-2a displays an SEM image of the as-grown h-BN crystals on a copper foil. We optimized the CVD conditions to grow h-BN crystals with triangular shape only. Some of the h-BN crystals grow as oppositely oriented triangles, highlighted by the purple and brown dashed contours, due to the orientational alignment with the underlying Cu(100) grain.^{25,28} The lattice of h-BN is composed of two sub-lattices occupied by nitrogen and boron atoms respectively.²⁰ Hence, h-BN lacks inversion symmetry and a zigzag-edged triangle can be either B- or N-terminated.^{8,20} This is shown by the schematic in Fig. 4-2b, which highlights the need for unambiguous experimental determination of the two opposite zigzag edge orientations. Fig. 4-2c shows an SEM image of h-BN crystals after transfer from the copper foil onto a TEM grid. After the transfer process, the h-BN triangles with sharp edges can still be identified by SEM, emphasizing the high fidelity of the transfer procedure. A pair of oppositely oriented h-BN crystals, delineated by the red and green dashed triangles, are further examined for edge orientations, as explained next.

Fig. 4-3a shows an overview STEM image of the triangular h-BN crystal delineated by the red dashed triangle in Fig. 4-2c. The h-BN crystal on the amorphous carbon film of the TEM grid shows sufficient contrast to identify the edges, which are indicated by a white dashed triangular contour, shifted away from the actual edges to not obscure them. Fig. 4-3b is an

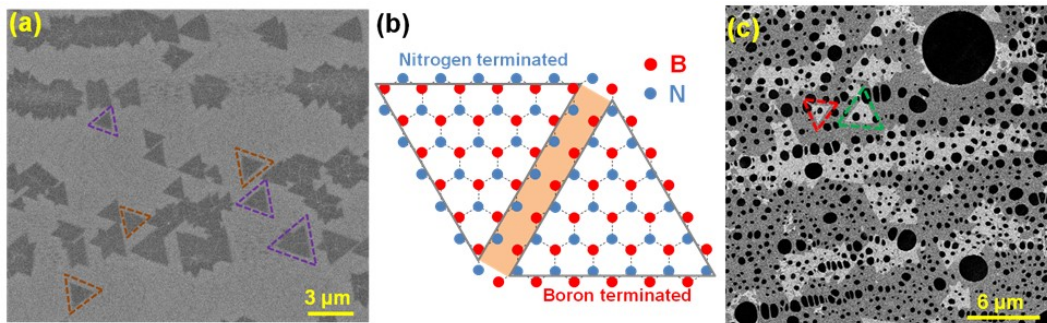


Figure 4-2. CVD grown h-BN crystals. (a) SEM image of equilateral triangle-shaped h-BN crystals on copper. More complicated shapes arise from merged triangles. Purple and brown dashed contours highlight oppositely oriented triangles. (b) Schematic showing two possible edge terminations for zigzag-edged triangular crystals of h-BN. (c) SEM image of the h-BN crystals after transfer onto TEM grid. Red and green dashed triangles highlight a pair of h-BN crystals, which were examined for edge orientations by STEM in Fig. 4-3.

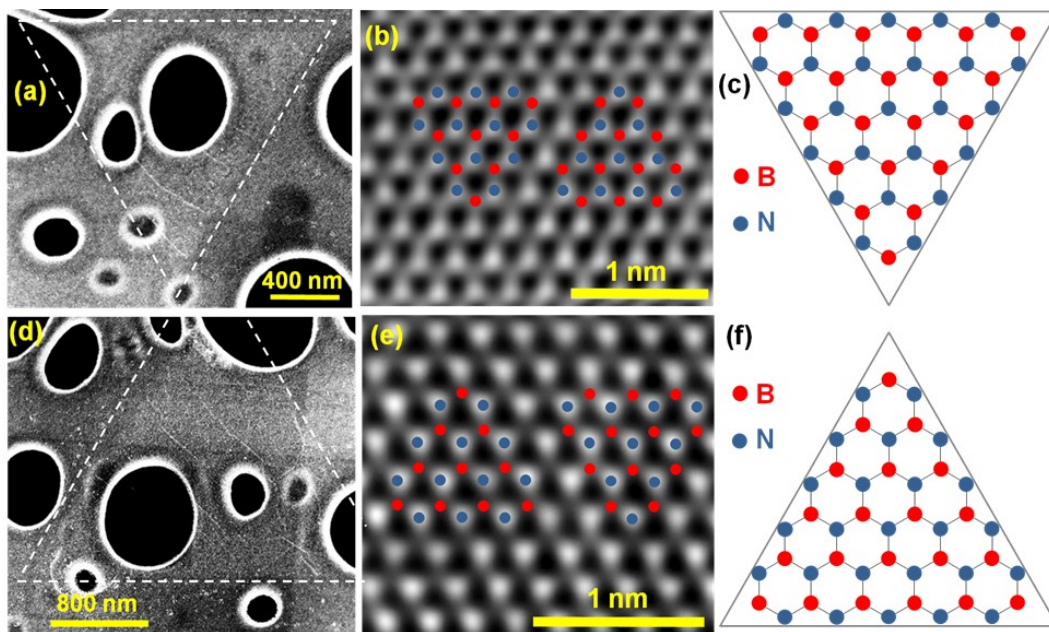


Figure 4-3. Edge orientation determination of triangle-shaped h-BN crystals. (a) Overview STEM image of the red delineated h-BN crystal in Fig. 4-2c. The edges are emphasized by white dashed lines, shifted away from the edges to avoid obscuring. (b) Atomically resolved image acquired in the interior of the h-BN crystal in panel a, overlaid with colored spots representing B and N atoms. (c) Schematic illustration of the edge and bulk orientations of the h-BN crystal in panels a and b. (d) Overview STEM image of the green delineated h-BN crystal in Fig. 4-2c. Similar to panel a the edges are signified by the shifted white dashed lines. (e) Atomically resolved image taken in the 2D bulk of the h-BN crystal in panel d, superimposed with the colored spots representing B and N atoms. (f) Schematic representation of the edge and bulk orientations of the h-BN crystal in panels d and e.

atomic-resolution Z -contrast image taken in the interior of the same h-BN crystal. Red and blue dots overlaid on this image signify nitrogen and boron atoms, respectively, at the atomic positions, as identified by the atomic number Z calculated from the intensity at each position. Fig. 4-3c shows a schematic, combining the lattice orientation information derived from the atomic resolution image Fig. 4-3b, and the contour of h-BN crystal from the overview image Fig. 4-3a. Clearly, the edges of this h-BN crystal are zigzag-oriented and N-terminated. It is worth mentioning here that, in a STEM, there is no rotation of images with increasing or decreasing magnification, since scan coils simply change the area over which they are scanned.²⁹ This is in contrast to a TEM, where changing magnification is accompanied by an image rotation due to the helical paths of electrons.²⁹ To ensure that there is no change of rotation in the scan direction with varying magnifications, a simple procedure was adopted. Starting at a high magnification (atomic resolution) the magnification was reduced in steps and identifying features between each image were compared. This procedure showed there was no rotation in MAADF image scan direction with a reduction to the magnification.

Next the edge orientation of the other h-BN crystal, which is delineated by the green dashed triangle in Fig. 4-2c is revealed. Similar to the discussion above, Fig. 4-3d is an overview, STEM image, where the h-BN crystal edges are signified by the shifted white dashed contour. Fig. 4-3e shows an atomically resolved image acquired in the 2D bulk of the h-BN crystal shown in Fig. 4-3d, with superimposed colored spots signifying B and N atoms. Fig. 4-3f shows a schematic, combining the lattice orientation information extracted from the atomic resolution image Fig. 4-3e and the contour of h-BN edges from the overview image Fig. 4-3d. Once again the edges of the h-BN crystal in Fig. 4-3d are also zigzag-oriented and N-terminated. The examination of these two crystals verifies in real space that their 2D bulks are oppositely

oriented, i.e., in two opposite directions, consistent earlier conclusions drawn from diffraction experiments.²⁵ For statistical significance, Fig. 4-4 shows another pair of triangular crystals of h-BN, whose edge-orientations turned out to be N-terminated and zigzag oriented. No armchair or B-terminated zigzag edges have ever been observed in this study.

The procedure discussed above determines the edge orientations by combining the “macroscopic” directions of the edges with the “bulk” orientation of the 2D crystal that is resolved by *Z*-contrast, atomic resolution imaging, circumventing the difficulty in directly imaging the atomic structure of the edges. This method can be used to further confirm the edge orientations of the “truncated triangle” (or equiangular but not equilateral hexagon) crystals of h-BN grown under B-rich conditions.^{13,18,21} Moreover, the method can also be applied to determine the edge orientations of other 2D materials. With “macroscopic” edge directions recorded in an overview image, edge orientations can in principle be determined by resolving the “bulk” orientation. This can be done for three-fold symmetric 2D crystals by diffraction only if particle beams are in the suitable energy range, and the rotation angle between the diffractogram and the real space image needs to be determined by a skillful scheme.²⁹ Low-energy electron diffraction patterns of h-BN show three-fold symmetry,²⁵ but the correspondence between relative spot brightness (bright/dark spots) and opposite orientations (B-/N-terminated zigzag) is not directly known and must be inferred by complicated simulation. The method discussed in this chapter, in contrast, directly resolves opposite edge orientations of 2D crystals that lack inversion symmetry.

Another advantage of this method is that the difficulty of suspending intact, as-grown edges on TEM grid for atomic resolution imaging (Fig. 4-1) is circumvented. It is important to note here that N-terminated zigzag in this work simply refers to the edge orientation. The actual edges may or may not be truncated edges terminated by N atoms as shown in Fig. 4-2.

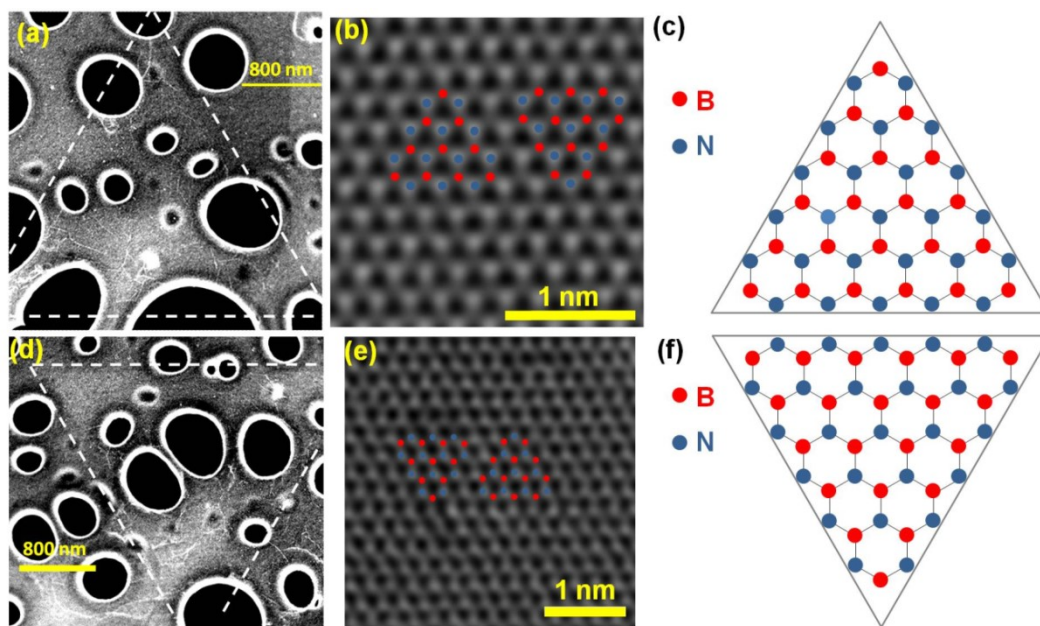


Figure 4-4. Edge orientation determination of triangle-shaped h-BN crystals. (a) Overview STEM image of an h-BN crystal. The edges are emphasized by white dashed lines, shifted away from the edges to avoid obscuring. (b) Atomically resolved image acquired in the interior of the h-BN crystal in panel a, overlaid with colored spots representing B and N atoms. (c) Schematic illustration of the edge and bulk orientations of the h-BN crystal in panels a and b. (d) Overview STEM image of another h-BN crystal, which is oppositely oriented to the crystal in panel a. The crystal edges are signified by the shifted white dashed lines. (e) Atomically resolved image taken in the 2D bulk of the h-BN crystal in panel d, superimposed with the colored spots representing B and N atoms. (f) Schematic representation of the edge and bulk orientations of the h-BN crystal in panels d and e.

Nevertheless, high-resolution TEM images of equilateral triangular holes in h-BN^{30,31,32} indicate that the sides of the holes are bulk truncated zigzag edges without reconstructions, although terminations cannot be resolved due to lack of Z-contrast. While the formation kinetics of those hole edges are different from that of the grown outer edges of crystals, the absence of edge reconstruction should be universal for all h-BN zigzag edges. Indeed, unreconstructed zigzag edges have been assumed in theoretical works^{33,34}.

4.4 Conclusion

In this study, the edge orientations of equilateral triangle-shaped h-BN crystals grown by CVD under a widely used condition have been resolved experimentally for the first time. All the examined edges are zigzag-oriented and N-terminated. Interestingly, for each apparently oppositely oriented pair of equilateral triangle-shaped crystals, both triangles have N-terminated zigzag edges but opposite bulk orientations, consistent with the previous experimental study.²⁵ This experimental determination finally verifies the long-held presumption in the literature about edge orientation of h-BN crystals grown on copper. Our CVD growth uses $\text{H}_3\text{B-NH}_3$ as the precursor, presumably providing a feedstock relatively balanced in B and N, which is predicted to lead to N-terminated zigzag edges for kinetic reasons rather than edge energy minimization.²⁰

4.5 Experimental methods

4.5.1 Growth of triangular h-BN crystals

Commercial copper foils (99.999%, 25 μm thick, Alfa Aesar) were used for the growth of h-BN crystals. The growth was performed with a commercial CVD system (OTF-1200X-80-II-4CV-PE-SL, MTI) with a 2 in. diameter quartz tube. The Ar and H_2 were ultra-high purity (UHP) grade gases, supplied by Airgas. Before growth, Cu foils were dipped in dilute nitric acid and DI

water for 20 seconds each and subsequently dried gently with a nitrogen gun. The foils were then loaded into a quartz tube (2'' diameter), which was then pumped down to the base pressure and then back-filled with Ar. This process was repeated three times. At atmospheric pressure, H₂ and Ar flows were adjusted to 100 and 900 sccm, respectively. The temperature was first ramped up to 1000 °C in 50 minutes, and then to 1040 °C in 10 minutes. H₂ and Ar flows were adjusted to 100 and 400 sccm, respectively. To initiate h-BN growth, 0.5 mg of ammonia borane⁸ was sublimed for 6.5 minutes at ~120 °C, using an external heating belt.²⁵ After the h-BN growth, the furnace was opened for rapid cooling without changing the gas flows. Foils were unloaded after the temperature dropped to around 50 °C under Ar ambient.

4.5.2 Transfer of h-BN crystals onto TEM grids

To reduce carbon contamination, a direct-transfer technique was used to transfer h-BN crystals onto transmission electron microscope (TEM) grids.²⁷ Briefly, holey carbon TEM grids were placed faced down onto the h-BN covered copper foils. A few drops of isopropyl alcohol were placed on the TEM grid and allowed to dry naturally for ~ 15 minutes. Afterward, to enhance the adhesion between the holey carbon film and h-BN crystals, the TEM grids were heated on a hot plate at 120 °C for 20 minutes. The underlying copper foil was etched away by a commercial etchant (CE-100, Transene). The etching time was ~ 60 minutes. To reduce carbon residue, the TEM grids were floated for ~12 hours on the surface of a 1:1 solution of commercial hydrochloric acid and de-ionized (DI) water.³⁵ The TEM grids were then further floated on three DI water baths, and allowed to dry naturally. In order to further reduce carbon contamination, the TEM grids were briefly annealed in air at 200 °C for 30 min on a hot plate³⁵ and then annealed at 160 °C in high vacuum for 8 hours, prior to loading in the STEM.

4.5.3 Microscopy characterization

Scanning electron microscope (SEM) images were acquired with an LEO 1525 SEM at 5 kV. The STEM imaging was performed with a Nion aberration-corrected UltraSTEM 100TM electron microscope, operated at 60 kV. The UltraSTEM 100TM has third and fifth-order aberration correcting capabilities, and a spatial resolution of 1.1 Å. To differentiate between atom types (N and B), Z-contrast imaging was employed.³⁶ This technique allows for the atom-by-atom determination of the atomic number Z by signal intensity from, in the case of 2D materials, a single atom alone. An annular detector is used to detect the transmitted electrons scattered to high angles. The contrast of such images follows approximately as Z squared.^{37,38,39} The technique is able to differentiate B, C, and N in single layers.²² All the Z-contrast STEM images were acquired using the medium angle annular dark field (MAADF) detector. During imaging, the high angle annular dark field (HAADF) detector was retracted to allow additional scattered electrons to reach the MAADF. This has the effect of reducing the Z-contrast but improving the signal-to-noise ratio. The atomic resolution Z-contrast images were acquired with a camera length of 1.24 m, a convergence semi-angle of 30 mrad, a collection semi-angle of approximately 50 mrad, a pixel count of 1024×1024 pixels, and a pixel dwell time of 32 μ s. The Z-contrast overview images were acquired under the same conditions as mentioned above, but with a pixel count of 2024×2024 pixels. The atomic resolution Z-contrast images were post-processed by a Lucy-Richardson deconvolution, a maximum entropy algorithm that treats the imaging probe as a point spread function.^{40,41} Deconvoluting probe shape contributions from the image has the effect of consolidating atom shape and improves the signal-to-noise ratio.

4.6 References

- (1) Y. Tsao, Materials Fundamentals of Molecular Beam Epitaxy. Academic Press-San Diego, 1993.
- (2) van der Zande, A. M.; Huang, P. Y.; Chenet, D. a; Berkelbach, T. C.; You, Y.; Lee, G.-H.; Heinz, T. F.; Reichman, D. R.; Muller, D. a; Hone, J. C. Grains and Grain Boundaries in Highly Crystalline Monolayer Molybdenum Disulphide. *Nat. Mater.* **2013**, *12*, 554–561.
- (3) Ohtomo, A.; Hwang, H.Y. A high-mobility electron gas at the LaAlO₃/SrTiO₃ heterointerface. *Nature* **2004**, *427*, 423–426.
- (4) Reyren, N.; Thiel, S.; Caviglia, A.D.; Kourkoutis, L.F.; Hammerl, G.; Richter, C.; Schneider, C.W.; Kopp, T.; Rüetschi, A.-S.; Jaccard, D.; Gabay, M.; Muller, D.A.; Triscone, J.-M.; Mannhart, J. Superconducting Interfaces between Insulating Oxides. *Science* **2007**, *317*, 1196–1199.
- (5) Pruneda, J.M. Origin of half-semimetallicity induced at interfaces of C-BN heterostructures. *Phys. Rev. B* **2010**, *81*, 161409(R).
- (6) Bhowmick, S.; Singh, A.K.; Yakobson, B.I. Quantum Dots and Nanoroads of Graphene Embedded in Hexagonal Boron Nitride. *J. Phys. Chem. C* **2011**, *115*, 9889–9893.
- (7) Yu, Q.; Jauregui, L. A; Wu, W.; Colby, R.; Tian, J.; Su, Z.; Cao, H.; Liu, Z.; Pandey, D.; Wei, D. *et al.* Control and Characterization of Individual Grains and Grain Boundaries in Graphene Grown by Chemical Vapour Deposition. *Nat. Mater.* **2011**, *10*, 443–449.
- (8) Kim, K. K.; Hsu, A; Jia, X.; Kim, S. M.; Shi, Y.; Hofmann, M.; Nezich, D.; Rodriguez-

Nieva, J. F.; Dresselhaus, M.; Palacios, T.; *et al.* Synthesis of Monolayer Boron Nitride on Cu Foil Using Chemical Vapor Deposition. *Nano Lett.* **2011**, *12*, 161-166.

(9) Guo, N.; Wei, J.; Fan, L.; Jia, Y.; Liang, D.; Zhu, H.; Wang, K.; Wu, D. Controllable Growth of Triangular Hexagonal Boron Nitride Domains on Copper Foils by an Improved Low-Pressure Chemical Vapor Deposition Method. *Nanotechnology* **2012**, *23*, 415605.

(10) Tay, R. Y.; Wang, X.; Tsang, S. H.; Loh, G. C.; Singh, R. S.; Li, H.; Mallick, G.; Tong Teo, E. H. A Systematic Study of the Atmospheric Pressure Growth of Large-Area Hexagonal Crystalline Boron Nitride Film. *J. Mater. Chem. C* **2014**, *2*, 1650-1657.

(11) Han, J.; Lee, J.-Y.; Kwon, H.; Yeo, J.-S. Synthesis of Wafer-Scale Hexagonal Boron Nitride Monolayers Free of Aminoborane Nanoparticles by Chemical Vapor Deposition. *Nanotechnology* **2014**, *25*, 145604.

(12) Wang, L.; Wu, B.; Chen, J.; Liu, H.; Hu, P.; Liu, Y. Monolayer Hexagonal Boron Nitride Films with Large Domain Size and Clean Interface for Enhancing the Mobility of Graphene-Based Field-Effect Transistors. *Adv. Mater.* **2014**, *26*, 1559–1564.

(13) Tay, R. Y.; Griep, M. H.; Mallick, G.; Tsang, S. H.; Singh, R. S.; Tumlin, T.; Teo, E. H. T.; Karna, S. P. Growth of Large Single-Crystalline Two-Dimensional Boron Nitride Hexagons on Electropolished Copper. *Nano Lett.* **2014**, *14*, 839–846.

(14) Lu, G.; Wu, T.; Yuan, Q.; Wang, H.; Wang, H.; Ding, F.; Xie, X.; Jiang, M. Synthesis of Large Single-Crystal Hexagonal Boron Nitride Grains on Cu–Ni Alloy. *Nat. Commun.* **2015**, *6*, 6160.

- (15) Song, X.; Gao, J.; Nie, Y.; Gao, T.; Sun, J.; Ma, D.; Li, Q.; Chen, Y.; Jin, C.; Bachmatiuk, A.; *et al.* Chemical Vapor Deposition Growth of Large-Scale Hexagonal Boron Nitride with Controllable Orientation. *Nano Res.* **2015**, *8*, 3164–3176.
- (16) Li, X.; Magnuson, C. W.; Venugopal, A.; Tromp, R. M.; Hannon, J. B.; Vogel, E. M.; Colombo, L.; Ruoff, R. S.; Ruoff, R. S. Large-Area Graphene Single Crystals Grown by Low-Pressure. *J. Am. Chem. Soc.* **2011**, *133*, 2816–2819.
- (17) Wu, Q.; Park, J.-H.; Park, S.; Jung, S. J.; Suh, H.; Park, N.; Wongwiriyan, W.; Lee, S.; Lee, Y. H.; Song, Y. J. Single Crystalline Film of Hexagonal Boron Nitride Atomic Monolayer by Controlling Nucleation Seeds and Domains. *Sci. Rep.* **2015**, *5*, 16159.
- (18) Stehle, Y.; Meyer, H. M.; Unocic, R. R.; Kidder, M.; Polizos, G.; Datskos, P. G.; Jackson, R.; Smirnov, S. N.; Vlassiuk, I. V. Synthesis of Hexagonal Boron Nitride Monolayer: Control of Nucleation and Crystal Morphology. *Chem. of Mater.* **2015**, *27*, 8041–8047.
- (19) Liu, Y.; Bhowmick, S.; Yakobson, B. I. BN White Graphene With “colorful” edges: The Energies and Morphology. *Nano Lett.* **2011**, *11*, 3113–3116.
- (20) Zhang, Z.; Liu, Y.; Yang, Y.; Yakobson, B. I. Growth Mechanism and Morphology of Hexagonal Boron Nitride. *Nano Lett.* **2016**, *16*, 1398–1403.
- (21) Tay, R. Y.; Park, H. J.; Ryu, G. H.; Tan, D.; Tsang, S. H.; Li, H.; Liu, W.; Teo, E. H. T.; Lee, Z.; Lifshitz, Y.; *et al.* Synthesis of Aligned Symmetrical Multifaceted Monolayer Hexagonal Boron Nitride Single Crystals on Resolidified Copper. *Nanoscale* **2016**, *8*, 2434–2444.

- (22) Krivanek, O. L.; Chisholm, M. F.; Nicolosi, V.; Pennycook, T. J.; Corbin, G. J.; Dellby, N.; Murfitt, M. F.; Own, C. S.; Szilagy, Z. S.; Oxley, M. P.; *et al.* Atom-by-Atom Structural and Chemical Analysis by Annular Dark-Field Electron Microscopy. *Nature* **2010**, *464*, 571–574.
- (23) Koskinen, P.; Malola, S.; Häkkinen, H. Evidence for Graphene Edges beyond Zigzag and Armchair. *Phys.Rev. B* **2009**, *80*, 16–18.
- (24) Kim, K.; Coh, S.; Kisielowski, C.; Crommie, M. F.; Louie, S. G.; Cohen, M. L.; Zettl, a. Atomically Perfect Torn Graphene Edges and Their Reversible Reconstruction. *Nat. Commun.***2013**, *4*, 2723.
- (25) Liu, L.; Siegel, D. A; Chen, W.; Liu, P.; Guo, J.; Duscher, G.; Zhao, C.; Wang, H.; Wang, W.; Bai, X.; *et al.* Unusual Role of Epilayer–substrate Interactions in Determining Orientational Relations in van Der Waals Epitaxy. *Proc. Nati. Acad. Sci. U.S.A.* **2014**, *111*, 16670–16675.
- (26) Li, X.; Cai, W.; An, J.; Kim, S.; Nah, J.; Yang, D.; Piner, R.; Velamakanni, A.; Jung, I.; Tutuc, E. *et al.* Large-Area Synthesis of High-quality and Uniform Graphene Films on Copper Foils. *Science* **2009**, *324*, 1312–1314.
- (27) Regan, W.; Alem, N.; Alemán, B.; Geng, B.; Girit, Ç.; Maserati, L.; Wang, F.; Crommie, M.; Zettl, A. A Direct Transfer of Layer-Area Graphene. *Appl. Phys. Lett.* **2010**, *96*, 11–13.
- (28) Wood, G. E.; Marsden, A. J.; Mudd, J. J.; Walker, M.; Asensio, M.; Avila, J.; Chen, K.; Bell, G. R.; Wilson, N. R. Van Der Waals Epitaxy of Monolayer Hexagonal Boron Nitride on Copper Foil: Growth, Crystallography and Electronic Band Structure. *2D Materials* **2015**, *2*, 25003.

- (29) Williams, D. B.; Carter, C. B. *Transmission Electron Microscopy: A Textbook for Materials Science*, Springer-Verlag, New York, 2009.
- (30) Jin, C.; Lin, F.; Suenaga, K.; Iijima, S. Fabrication of a Freestanding Boron Nitride Single Layer and Its Defect Assignments. *Phys. Rev. Lett.* **2009**, *102*, 195505.
- (31) Meyer, J.C.; Chuvilin, A.; Algara-Siller, G.; Biskupek, J.; Kaiser, U. *Nano Lett.* **2009**, *9*, 2683-2689.
- (32) Alem, N.; Erni, R.; Kisielowski, C.; Rossell, M.D.; Gannett, W.; Zettl, A. Atomically thin hexagonal boron nitride probed by ultrahigh-resolution transmission electron microscopy. *Phys. Rev. B* **2009**, *80*, 155425.
- (33) Zhang, Z.; Guo, W.; Yakobson, B. I. Self-modulated band gap in boron nitride nanoribbons and hydrogenated sheets. *Nanoscale* **2013**, *5*, 6381-6387.
- (34) Zhang, Z.; Guo, W. Energy-gap modulation of BN ribbons by transverse electric fields: First-principles calculations. *Phys. Rev. B* **2008**, *77*, 075403.
- (35) Meyer, J. C.; Kurasch, S.; Park, H. J.; Skakalova, V.; Künzel, D.; Grobß, A.; Chuvilin, A.; Algara-Siller, G.; Roth, S.; Iwasaki, T.; *et al.* Experimental Analysis of Charge Redistribution due to Chemical Bonding by High-Resolution Transmission Electron Microscopy. *Nat. Mater.* **2011**, *10*, 209–215.
- (36) Pennycook, S. J.; Chisholm, M. F.; Lupini, A. R.; Varela, M.; Borisevich, A. Y.; Oxley, M. P.; Luo, W. D.; van Benthem, K.; Oh, S.-H.; Sales, D. L.; *et al.* Aberration-Corrected Scanning Transmission Electron Microscopy: From Atomic Imaging and Analysis to Solving

Energy Problems. *Phil. Trans. R. Soc. A* **2009**, *367*, 3709–3733.

(37) Crewe, A.V.; Wall, J.; Langmore, J. Visibility of single atoms. *Science* **1970**, *168*, 1338-1340.

(38) LeBeau, J. M.; Findlay, S. D.; Stemmer, S. Quantitative Atomic Resolution Scanning Transmission Electron Microscopy. *Phys. Rev. Lett.* **2008**, *100*, 206101.

(39) Wang, Z. W.; Li, Y. Z.; Palmer, R. E. Quantitative Z-contrast imaging in the scanning transmission electron microscope with size-selected clusters. *Phys. Rev. B* **2011**, *84*, 073408.

(40) Richardson, W.H. Bayesian-Based Iterative Method of Image Restoration. *JOSA*. **1972**, *62*, 55-59.

(41) Lucy, L.B. An iterative technique for the rectification of observed distributions. *Astron. J.* **1974**, *79*, 745-754.

CHAPTER 5

MAPPING THE LAYER COUNT OF FEW-LAYER HEXAGONAL BORON NITRIDE AT HIGH LATERAL SPATIAL RESOLUTIONS

This chapter is a slightly modified version of the paper with the same title published in 2D Materials in October 2017 by Ali Mohsin, Nicholas G. Cross, Lei Liu, Kenji Watanabe, Takashi Taniguchi, Gerd Duscher and Gong Gu. The introduction in this chapter has been expanded to cover literature review related to the growth of few-layer h-BN. Also, the supporting information in the published paper has been included as a part of the main text in this chapter.

All the figures and most of the text in this chapter are reproduced with permission from Mohsin, A.; Cross, N. G.; Liu, L.; Watanabe, K.; Taniguchi, T.; Duscher, G.; Gu, G. Mapping The Layer Count Of Few-Layer Hexagonal Boron Nitride At High Lateral Spatial Resolutions *2D Mater.* **2018**, 5, 015007. Copyright 2017 IOP Publishing Limited.

As a first author of the paper, I was responsible for (1) Designing of the experiments for the CVD growth of few-layer h-BN films. (2) Optimization of the growth parameters. (3) Assembling of the CVD system on which growth experiments were carried out. (4) Characterization of few-layer h-BN films by SEM. (5) Transfer of few-layer h-BN films onto the TEM grids for further characterization. N.G.C. carried out STEM characterization under the supervision of G.D. L.L. exfoliated thin flakes from the bulk h-BN crystals. K.W. and T.T. grew bulk h-BN crystals. G.D. and G.G. proposed the experimental schemes and wrote the manuscript.

5.1 Abstract

Layer count control and uniformity of 2D layered materials are critical to the investigation of their properties and to their electronic device applications, but methods to map 2D material layer count at nanometer-level lateral spatial resolutions have been lacking. Here, we demonstrate a method based on two complementary techniques widely available in transmission electron

microscopes to map the layer count of multilayer h-BN films. The mass-thickness contrast in HAADF imaging in the STEM mode allows for thickness determination in atomically clean regions with high spatial resolution (sub-nanometer) but is limited by surface contamination. To complement, another technique based on the boron K ionization edge in the EELS spectrum of h-BN is developed to quantify the layer count so that surface contamination does not cause an overestimate, albeit at a lower spatial resolution (nanometers). The two techniques agree remarkably well in atomically clean regions with discrepancies within ± 1 layer. For the first time, the layer count uniformity on the scale of nanometers is quantified for a 2D material. The methodology is applicable to layer count mapping of other 2D layered materials, paving the way toward the synthesis of multilayer 2D materials with homogeneous layer count.

5.2 Introduction

Important physical properties such as the band structure of a two-dimensional (2D) layered material may strongly depend on the layer count,¹ which must be controllable and homogeneous for electronic device applications. Furthermore, the constituent 2D materials in van der Waals heterostructures,² which have recently become an important research direction, must also have controllable uniform layer counts. Hexagonal boron nitride (h-BN) has emerged as an important ingredient of these heterostructures.^{2,3,4,5,6} As a 2D insulator, h-BN is a good choice for tunnel dielectric in 2D-to-2D tunneling devices.^{4,5,6} When used as a supporting substrate for 2D semiconductors, h-BN dramatically enhance their electrical transport.⁷ These applications of h-BN require smoothness and therefore layer count uniformity of multilayer h-BN. The application in the tunneling devices also requires control over the h-BN thickness or layer count beside the uniformity thereof.

Multilayer h-BN can be exfoliated from bulk crystals, such as those high-quality crystals grown by recrystallization of h-BN using a metal solvent.⁸ The inherent randomness of the exfoliation process, however, precludes good control of the layer count of the resulting flakes, the area of which is also limited by the exfoliation process. To achieve large area, h-BN has been grown by chemical vapor deposition (CVD).^{6,9,10,11,12,13,14,15,16} Reliable determination of the layer count and its spatial uniformity are important for the aforementioned electronics device applications of h-BN thin films. The most popular method for determining the number of layers is based on counting the layer fringes at the edges of a hole in the film,^{9,10,11,12,13,14,15} similar to the common technique used to determine the number of walls of a nanotube.¹⁷ The shortcoming of this method is that it reveals the number of layers only at the edges of a film. Atomic force microscopy provides another means to characterize thin films of h-BN,^{10,11,12,14,16} but it is incapable of mapping the layer count of an h-BN thin film because it cannot differentiate between true thickness variation and substrate roughness or surface contamination. Raman spectrum mapping overcomes this issue as the characteristic Raman signature of h-BN can differentiate between 1-3 layers of h-BN,¹⁸ but the spatial resolution is limited to hundreds of nanometers and it is not suitable for thicker films. While low-energy electron reflectivity (LEER) spectra^{19,20} provide a true “layer counting” method, the spatial resolution of layer count mapping based thereon is limited to the sub-micrometer level by low-energy electron microscopy (LEEM). Furthermore, LEEM instruments are much less widely available than TEMs.

To overcome the limitations of the above-mentioned techniques, here we employ two complementary characterization techniques, namely STEM and EELS to determine the number of layers in an h-BN thin film. With these two techniques corroborating each other, monolayer accuracy and high spatial resolution are achieved. We point out that advanced atomic-resolution

STEMs are not required; a TEM operating in the STEM mode suffices. Therefore our method can be widely adopted. HAADF imaging, a technique that relies on Rutherford scattering, resulting in intensity I that scales with atomic number Z of the scattering atom approximately as $I \propto Z^2$, and therefore elemental contrast, i.e. Z -contrast can be used to directly correlate intensity to sample thickness.^{21,22,23,24} This is because the intensity exhibits a mass thickness contrast. For a uniform single phase material with homogeneous composition and structure (e.g. h-BN in this study), the variation in intensity depends only on sample thickness. Inevitable surface contamination complicates this seemingly straightforward method, however, necessitating a complementary technique to eliminate the effect of surface contamination. To this end, EELS mapping is performed to acquire boron K ionization edge intensity maps, which are used to generate maps of the areal density of boron atoms by modeling the EELS core-loss edge using x-ray photoabsorption (XRPA) differential cross-section. A simple calculation then converts the B atom areal density to h-BN layer count. In EELS, the boron K-edge does not overlap other features. More important, surface contaminants are mostly organic adsorbates, which are unlikely to contain B. While this ‘see-through-the-junk’ technique allows for layer count mapping without being affected by surface contamination, the larger pixel size of EELS mapping as compared to that of STEM imaging reduces spatial resolution of the method. Therefore, these two techniques complement and corroborate each other. We find the two methods agree remarkably well in mapping the inhomogeneous layer count of a multilayer h-BN film grown by CVD on Cu. To gain further confidence in our methodology, we have mapped an exfoliated h-BN sample that is known to be uniform in thickness distribution, and find that indeed the two techniques combined can accurately determine the layer count. Our work reveals that the layer count of h-BN grown by CVD on Cu is inhomogeneous and that the thickness uniformity of

CVD-grown multilayer h-BN needs improvement for electronic device applications. Moreover, the methodology developed here is also applicable to thin films of other 2D materials e.g. transition metals dichalcogenides.²⁵

5.3 Results and discussion

Before the description of the STEM-based method to determine layer count, the morphology of the as-grown h-BN film on the copper foil is studied with an SEM. Fig. 5-1a is an overview SEM image, where wrinkles in the h-BN film (e.g., the one indicated by a blue arrow), which are similar to those in CVD-grown graphene on copper,²⁶ indicate full coverage of h-BN film on the foil. The wrinkles are more clearly shown in zoomed-in image Fig. 5-1b. Furthermore, there is a high density of adlayers, as indicated by red and green arrows in Fig. 5-1b. There are two types of adlayers: one consisting of very dense clusters of h-BN, having sizes of tens of nm (green arrows) and the others comprising of somewhat isolated triangles, having the dimensions of several hundreds of nm (red arrows). Further zoomed-in SEM images in Figs. 5-1(c,d) highlight both of these adlayer types. It is worth noting that the presence of these adlayers contributes to the layer count variation. Due to the small lateral dimensions of the adlayers, the variation in layer count cannot be resolved by the methods mentioned earlier in the introduction.

Next, the h-BN film was transferred onto a TEM grid, and layer count maps were derived from HAADF images acquired in the STEM mode of the TEM. Fig. 5-2 details the procedure to convert raw HAADF-STEM image of an h-BN film to a layer count map. Fig. 5-2a shows a raw image of an h-BN film. A hole in the region of interest is identified to determine the absolute value of background intensity due to the dark current, and right inset shows a zoomed-in image of the hole (vacuum). A red line is drawn along the hole in the right-inset and left inset shows an intensity profile along the red line, corresponding to the dark current. Fig. 5-2b shows the same

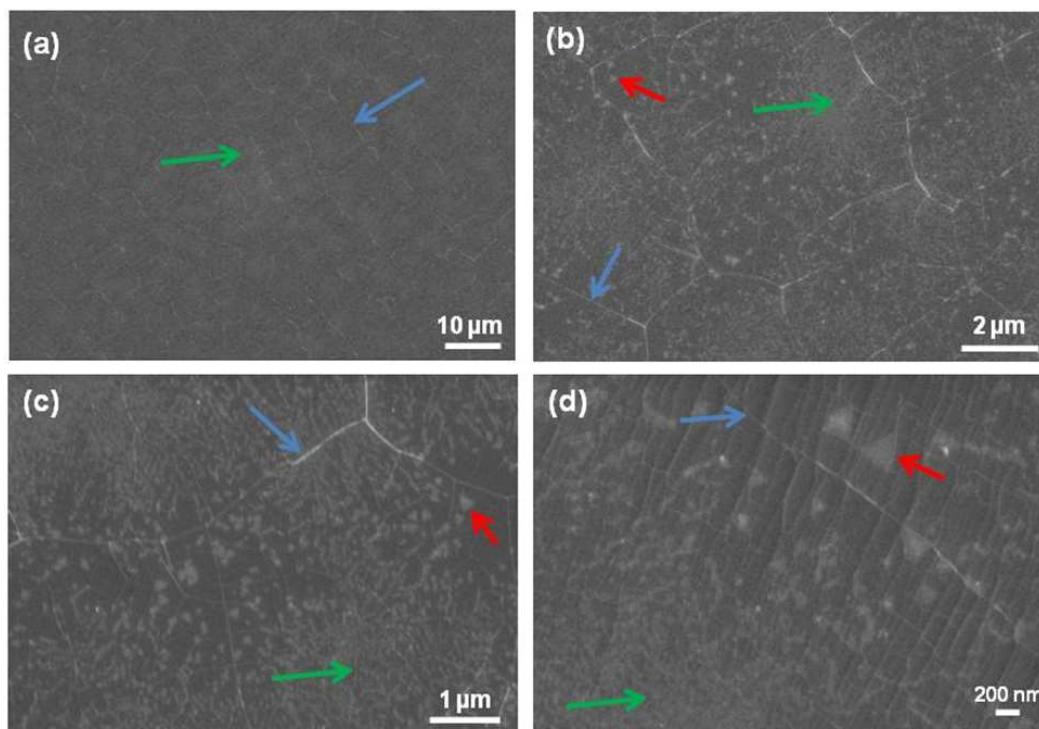


Figure 5-1. SEM images of CVD grown h-BN film on copper. (a) Overview SEM image. (b) Zoomed-in image highlighting wrinkles in the h-BN film (blue arrows). (c,d) Further zoomed-in images, showing very dense clusters of adlayers, having sizes of tens of nm (green arrows) and somewhat isolated triangles with dimensions of few several hundreds of nm (red arrows).

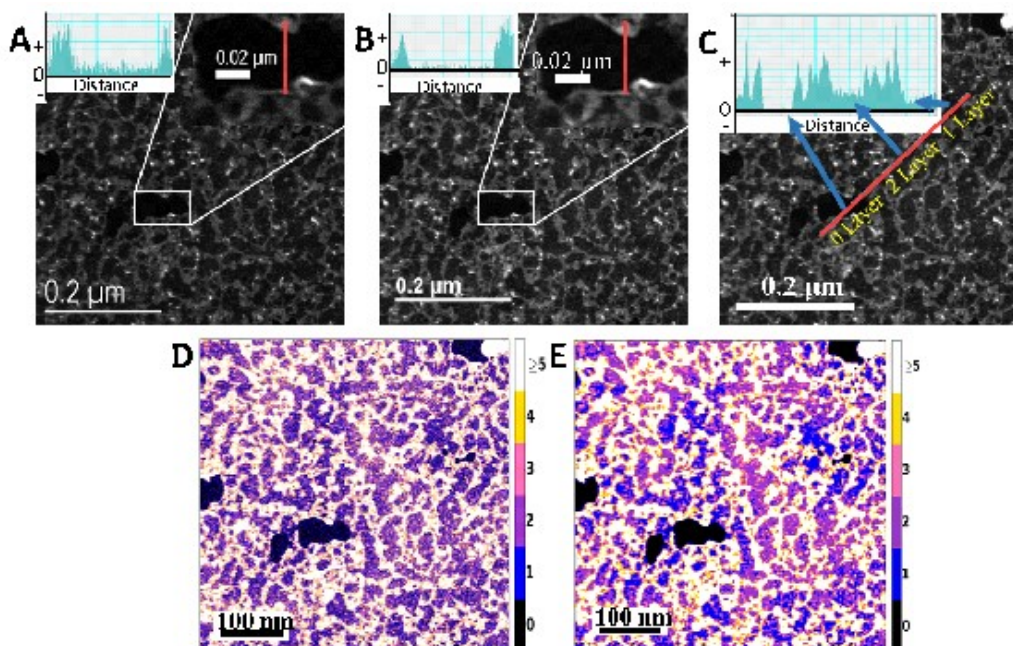


Figure 5-2. Converting HAADF STEM image to layer count map. (A) Raw HAADF-STEM image of the h-BN film. A hole is identified, and right inset shows a zoomed-in image of the hole. The left inset shows profile along the red line, where vacuum (hole) exhibits non-zero absolute intensity due to dark current. (B) Same image after the subtraction of dark current. Insets show zero intensity in the hole. (C) HAADF STEM image in panel b, after dividing every pixel by the intensity of a single layer of h-BN. Inset is an intensity profile highlighting three regions which are 0, 2 and 1 layer thick. (D) False-color layer count map directly derived from (c) by rounding each pixel value to an integer number of layers. (E) Layer count map derived from (c) by first applying a series of Gaussian filters and then rounding to an integer number of layers.

image as Fig. 5-2a, after the subtraction of background intensity from the entire image. The right-inset in Fig. 5-2b shows that the same hole identified in Fig. 5-2a now has zero intensity. Then, the smallest step size from a contamination-free area is identified, to determine the intensity of a single layer of h-BN. The presence of a single layer of h-BN at the particular pixel of HAADF image is corroborated with the corresponding pixel in the EELS map. Then, the intensity of every pixel in the HAADF image is divided by the intensity of a single layer of h-BN, to convert the entire image into a layer count map as shown in Fig. 5-2c, assuming the intensity of every pixel of the HAADF image scales linearly with the local layer count as the coherent Bragg scattering can be justifiably ignored. The map is now in the unit of h-BN layers but not yet discretized to integer layer count. The inset shows an intensity profile along the red line, corresponding to three regions which are identified as 0, 2, and 1 layer thick. Note that the spatial variation in the absolute values of intensities corresponding to 1 and 2 layers is due to the presence of surface contamination distributed randomly in the form of web throughout the image. Fig. 5-2d shows a false color layer map obtained by rounding the absolute pixel values in Fig. 5-2c, and assigning them to a discrete number of layers. Fig. 5-2e shows another false-color layer map derived from Fig. 5-2c, where the map is first smoothed by a series of four Gaussian filters to reduce the effects of high-frequency noise, before converting it into an integer number of layers, as in Fig. 5-2d. This filtering led to a slight broadening of features, especially where surface contamination layers were thick. Lastly, the values of every pixel were rounded into integers.

Fig. 5-3a shows a more detailed analysis of the layer count map shown in Fig. 5-2e. The size of this map is $529 \text{ nm} \times 529 \text{ nm}$ and the pixel size is about $0.28 \text{ nm} \times 0.28 \text{ nm}$. In the mapped area, there are atomically clean regions separated by unavoidable surface

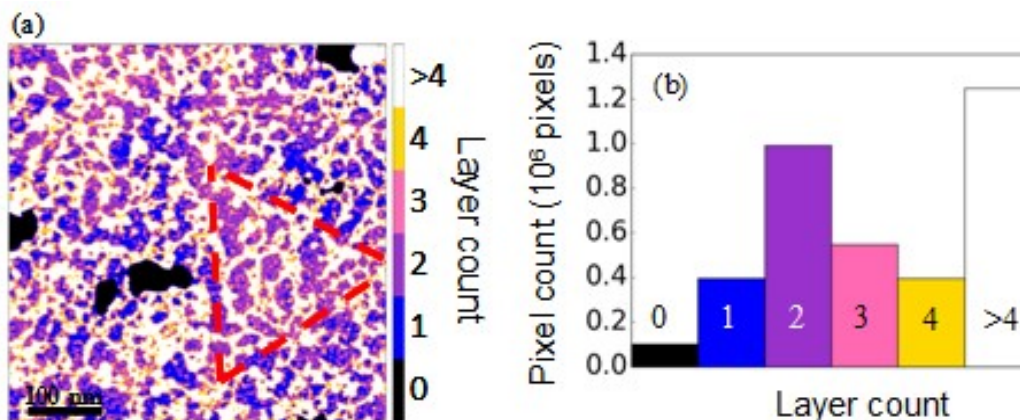


Figure 5-3. Layer count mapping of the h-BN film based on HAADF imaging in STEM mode. (a) Color-coded layer count map. Areas with significant surface contamination are saturated as white and assigned layer count > 5 . Most of the rest of the film exhibits layer counts of 1 or 2. Small adlayers at a length scale of tens of nm are observed (light pink and purple regions with total layer counts of 2 and 3, respectively). Red dashed triangular contour shows an adlayer with lateral dimensions of roughly 200 nm. The small, cluster-like and the big, triangular adlayers are respectively consistent with those observed in SEM images (Fig. 5-1). Black regions represent holes in the film. (b) Bar graph showing frequency of occurrence for pixels values in (a).

contamination. Since the surface contamination results in artificially large thickness variation, such regions are assigned a unique color code of white and labeled as layer count > 5 . Black regions where the layer count is zero represent holes in the film, introduced during the transfer process. The majority of the h-BN film is composed of 1 to 2 layers. Fig. 5-3a shows the layer count varying between 2 and 3 (light pink and purple regions), at a length scale of several tens of nm. This variation is attributed due to the dense clusters of h-BN adlayers, shown earlier in SEM images (Fig. 5-1). A triangular region mostly comprising of 2-3 layers, delineated by the red dashed contour can also be seen. Such triangular shaped regions are attributed to the isolated triangles of h-BN, with lateral dimensions of several hundreds of nm, also shown earlier in SEM images (Fig. 5-1). Fig. 5-3b shows a histogram of the number of pixels in Fig. 5-3a for each layer count value. It shows that a large percentage of the area is covered by contamination. It is surprising that there are almost as many 4-layer pixels as single layer pixels. Closer examination reveals that 4-layer regions are mostly within or at the rims of areas of surface contamination. This highlights the importance of proper interpretation of the result and being mindful of the large influence surface contamination has on the HAADF images. To overcome the shortcoming introduced by the presence of contamination in the reliable determination of a number of layers in HAADF image, criteria will be presented later to identify contaminated areas with higher confidence.

To complement the layer count mapping by HAAD imaging, which provides high spatial resolution but suffers from corrupted layer count values in unavoidable contaminated regions, EELS mapping is performed to acquire boron K ionization edge intensity maps, which are used to generate maps of the areal density of boron atoms by modeling the EELS core-loss edge using X-ray photoabsorption differential cross-section. A simple calculation then converts the B atom

areal density to h-BN layer count, as will explained next.

A systematic model-based approach is employed to quantify EELS mapping data. A method similar in spirit to but slightly different from that described by Verbeeck and Van Aert²⁷ is applied, to calculate layer count for each pixel of the EELS map. Fig. 5-4a plots the raw EELS spectrum from a typical pixel (black curve) of an EELS map, along with fitting curves. The loss spectrum, normalized against the total beam count I_0 (without sample), is modeled as

$$\frac{C(E)/\Delta E}{I_0} = AE^{-r} + aE^2 + bE + c + P \frac{d\sigma}{dE}, \quad (1)$$

where $C(E)$ is the count at energy loss E , $\Delta E = 0.411$ eV is the energy dispersion of the energy channel, $d\sigma/dE$ is the energy-differential scattering cross-section of the concerned ionization edge, and A , r , a , b , c , and P are fitting parameters. The first four terms ($AE^{-r} + aE^2 + bE + c$) model the background as a power-law decay modified by a polynomial to capture deviations from a simple power law. To obtain values of the fitting parameters, the differential cross section $d\sigma/dE$ (dark green curve) calculated by the XRPA theory is used, without the modulation by the chemical or crystallographic environment. Therefore, least squares fitting is performed to the blue curve, which is the raw spectrum within two windows. Here, for the B K-edge, the first window is from 170 eV to 184 eV (i.e. 5 eV below the onset of the B-K-edge), and the second window is from 249 eV (where the modulation vanishes) to 279 eV (i.e. 5 eV below the carbon K-edge). The power r from fitting is in the range of 2 to 4 for all spectra, as expected. After the fitting, the actual B K-edge is obtained by subtracting the background ($AE^{-r} + aE^2 + bE + c$) from the raw spectrum and is plotted as the red curve. By subtracting the background terms i.e., ($AE^{-r} + aE^2 + bE + c$), equation 1 can be re-arranged as below.

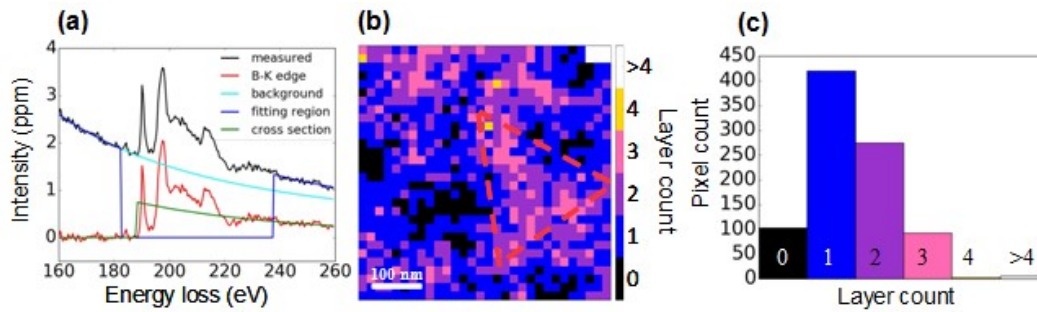


Figure 5-4. Layer count mapping by EELS. (a) Typical EELS and corresponding fitting curves. (b) Layer count map based on EELS analysis in. (c) Histogram of layer count in (b).

$$P = \frac{\frac{C(E)}{\Delta E} / I_0}{\frac{d\sigma}{dE}} \quad (2)$$

Since $[C(E)/\Delta E]/I_0$ is an inelastic scattering probability and $d\sigma/dE$ is an inelastic scattering probability for a single atom, their ratio P is the areal density of B atoms. Finally, the layer count is obtained by dividing P by the B atom areal density of a single layer of h-BN (18.2 nm^{-2}) and then rounding to the nearest integer. The B atom density of a single layer is determined using single crystal x-ray diffraction crystallographic data.²⁸

For the most accurate quantification of the layer count, the boron K ionization edge is used. The B K-edge has an onset at 189 eV, a low energy for core electron energy losses, and thus a large scattering cross section with no other features that overlap and interfere with it. K-edge cross sections are the most reliably known compared to other ionization edges for all elements.²⁹ The nitrogen K-ionization edge is not used in the determination of layer count because surface contaminations may contain nitrogen.³⁰ Additionally, nitrogen has a smaller cross-section which results in a less reliable ionization edge.

Fig. 5-4b is a layer count map derived from the EELS analysis described above. Its field of view is $0.5 \mu\text{m} \times 0.5 \mu\text{m}$, identical to that of Fig.5-3a, as EELS were acquired simultaneously with the HAADF image. The much larger pixel size (about $16 \text{ nm} \times 16 \text{ nm}$, each made of 64×64 HAADF image pixels) of EELS mapping, however, limits the spatial resolution of this technique. By using the boron K ionization as a signature of the h-BN material to quantify the layer count, the EELS map in Fig. 5-4b is unaffected by surface contamination, thus providing a see-through-the-dirt technique. As in Fig. 5-3a, black regions here in Fig. 5-4b also represent holes in the film. This map, not corrupted by surface contamination although at a lower spatial

resolution than Fig. 5-3a, clearly shows that the majority of the film in the field of view is composed of a single layer while areas comprising of 2 and 3 layers are also present. As in Fig. 5-3a, the same triangular adlayer can be discerned and is also delineated by red dashed lines. Also, a region of unusually high layer count at the top right corner of Fig. 5-4b is present, coincident to the same high layer count region in Fig. 5-3a with larger lateral dimensions than typical contaminated areas. Its h-BN equivalent mass thickness is 35 layers. This region is attributed to a nanoparticle of poly-aminoborane and its partially dehydrogenated derivatives, which are by-products of the precursor ($\text{H}_3\text{B-NH}_3$) decomposition, as reported in the literature.³¹ The histogram of the pixels of EELS map in Fig. 5-4b shows that the h-BN film is dominated by monolayer regions, with bi- and trilayer regions also present. The model-based analysis has an error of about $\pm 10\%$ in mass thickness, mostly arising from the uncertainty in the energy-differential cross-section. This error is insignificant when the mass thickness is discretized to layer count. Interpreting the EELS-derived layer count map in conjunction (Fig. 5-4b) with the HAADF imaging-derived map (Fig. 5-3a), we conclude that the film is composed of one continuous monolayer of h-BN with randomly distributed discontinuous adlayers consisting of 1 to 2 layers in addition to the continuous monolayer.

Worth mentioning is an alternative EELS-based technique used to estimate sample thickness values, the log-ratio method.³² This method has larger errors ($\sim \pm 20\%$), and does not differentiate surface contamination from the true h-BN film. At a low spatial resolution, as our B K-edge analysis, it does not provide any merit to complement the HAADF imaging.

The comparison of the layer count measured by the two techniques is presented next. Fig. 5-5a maps the absolute value of layer count difference between Figs. 5-3a and 5-4b. The EELS map in Fig. 5-4b is re-pixelated without loss of information to match the pixel density of the

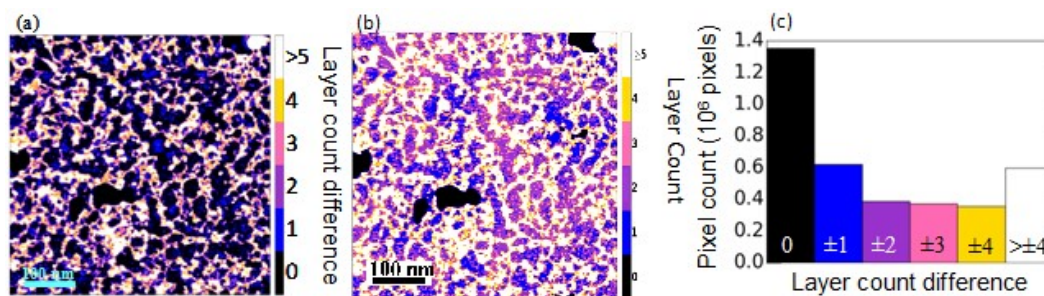


Fig. 5-5. Comparison of layer count distributions determined by HAADF imaging and EELS mapping. (a) Map of the absolute value of layer count difference between Figs. 5-3a and Figs. 5-4b. (b) Layer count map derived from HAADF imaging in Fig. 5-3a (c) Histogram of layer count discrepancy. A side-by-side comparison of Figs. 5-5(a,b) indicates remarkable agreement between the two techniques, with discrepancies > 1 layers only in contaminated regions.

HAADF image Fig. 5-3a. Zero layer count difference (coded black in Fig. 5-5a) represents a perfect agreement between the two techniques. Fig. 5-5c is the histogram of pixel values Fig. 5-5a (i.e. layer count differences between Figs. 5-3a and 5-4b). HAADF imaging derived layer count map in Fig. 5-3a is also shown in Fig. 5-5b for side-by-side comparison, which indicates that regions with layer count discrepancy of 3 and above in Fig. 5-4a largely match those with layer count ≥ 4 ; these are the contaminated regions. Layer count discrepancies of 2 are seen essentially within or at the rims of the contaminated regions, attributed to the effects of smoothing (Gaussian filtering), discretizing, and pixelating. In the clean regions, the remarkable agreement between the two techniques is attested by the dominance of zero layer count difference regions. There is also an appreciable fraction of the contamination-free regions exhibiting layer count differences of ± 1 , attributable to errors in both methods redistributed by the combined effects of smoothing, discretizing, and pixelating.

In order to clearly map out the layer count in the clean areas, it is important to first identify them. Figure 5-6a maps out the contaminated areas according to the following criterion:

$$(\text{Layer count by imaging} \geq 5) \text{ OR } (\text{discrepancy between imaging and EELS} \geq 3), \quad (3)$$

All pixels satisfying this criterion are considered contaminated and colored red, while the rest are represented by gray levels proportional to the imaging-derived mass thicknesses before rounding to integer layer counts. High intensities are clearly seen surrounding the red areas, indicating that this criterion misses the rims of the contaminated areas. In order to include the rims of the contaminated areas, a simple criterion is employed:

$$(\text{discrepancy between imaging and EELS} \geq t), \quad (4)$$

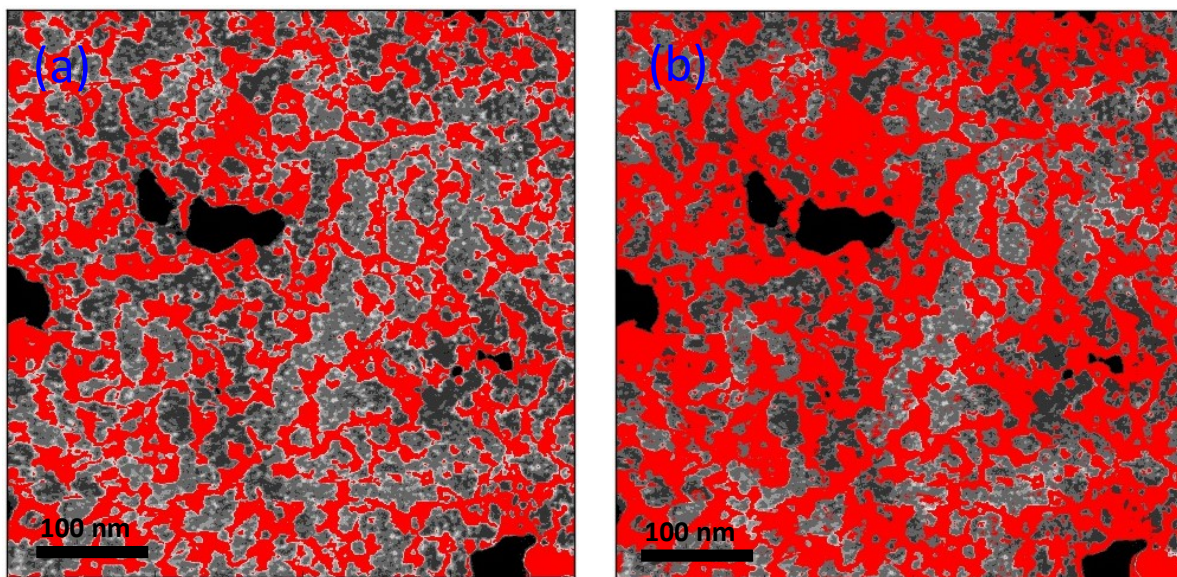


Figure 5-6. Identifying the contaminated areas. (a) Contaminated areas identified by criterion (1) colored in red, with rest of map in grayscale proportional to mass thickness derived from HAADF imaging. (b) Contaminated areas colored in red, identified by criterion (4) with $t = 1.5$.

where t is a threshold. Here, the discrepancy is calculated from mass thickness values before rounding to integers, thus the threshold does not need to be an integer. After trying a series of decreasing values for t , Fig. 5-6b identifies the contaminated areas with $t = 1.5$. Visually, the contaminated areas are well represented. It is worth mentioning here that the contaminated areas by criterion (3) are identified first, and then expanded to include the rims, instead of arbitrarily setting t in order to claim discrepancies are not larger than 1 in clean areas.

Fig. 5-7 and Table 5-1 below show details of the layer count mapping and statistics in the clean areas. Since the criterion used in Fig. 5-7a identifies contaminated areas with high confidence as discussed above (Fig. 5-6b), Fig. 5-7b represents the layer count statistics of the h-BN film. For comparison, Fig. 5-7(c,d) shows the layer count map and histogram of the same region excluding contaminated areas using criterion (3) alone. For better comparison, the pixel count values in histograms Figs. 5-7(b,d) are listed in Table 5-1. Significant differences are only seen for layer counts 3 and 4, because criterion (3) fails to identify rims of contaminated areas as such. The established criterion results in a visually excellent discrimination of contaminated areas, indicating the reliability of the method. Once again, layer count map in Fig. 5-7a shows a triangle-shaped, large adlayer region (see dashed contour in Fig. 5-3a) along with numerous irregularly shaped, smaller adlayer regions on a monolayer background, consistent with the SEM pictures in Fig. 5-1.

The above results, with a remarkable agreement between the two techniques, reveal that the CVD-grown h-BN on Cu under study is non-uniform in layer count. To gain further confidence of the finding, the two methods are applied to determine layer count of exfoliated h-BN from a bulk crystal,⁸ a sample known to be spatially uniform in terms of thickness. Data on this sample were collected using an UltraSTEM 100 operated at 60 kV. The $128 \text{ nm} \times 128 \text{ nm}$

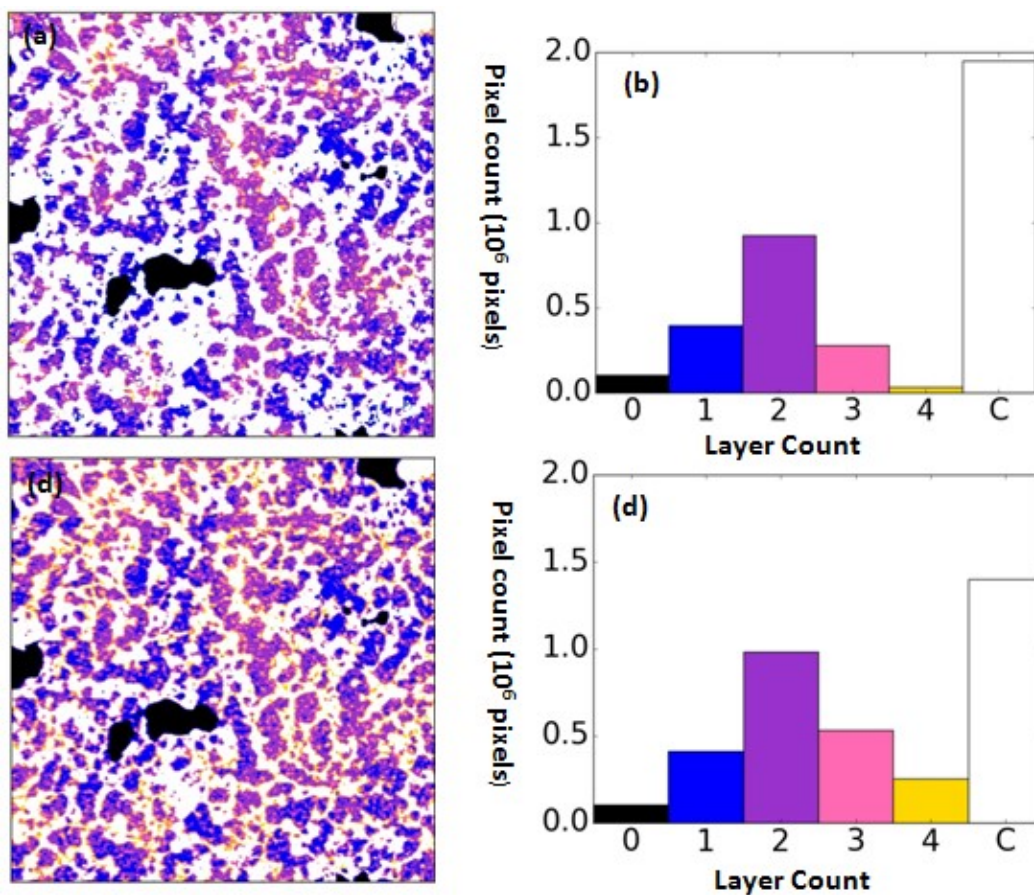


Figure 5-7. Layer count mapping and statistics of CVD-grown h-BN excluding contaminated areas. (a) Layer count map of the same region as in Fig. 6-3a with contaminated areas colored coded white (labeled “C” in color code bar), with contaminated areas identified by the criterion (4) with $t = 1.5$. (b) Histogram of (a). (c) Layer count map of the same region with contaminated areas identified by criterion (3). (d) Histogram of (c).

Table 5-1. Layer count statistics

| Layer count | Pixel count (10^6 pixels) | | Pixel count difference between the two criteria |
|--------------|---|--------------------------------|--|
| | Criterion (4) with $t = 1.5$ (Fig. 6-7a,b) | Criterion (3) (Fig. 6-7c,d) | |
| 0 | 0.1023 | 0.1036 | 1.2% |
| 1 | 0.3952 | 0.4117 | 4.2% |
| 2 | 0.9271 | 0.9838 | 6.1% |
| 3 | 0.2784 | 0.5353 | 92% |
| 4 | 0.0324 | 0.2524 | 678% |
| Contaminated | 1.9506 | 1.3996 | -28% |

EELS map consisting of 25×25 pixels, each $5.12 \text{ nm} \times 5.12 \text{ nm}$, was acquired with a post-column spectrometer (Enfina by Gatan, Inc.). The energy dispersion was 0.3 eV and the acquisition time was 1.5 s/pixel. The HAADF STEM image was acquired simultaneously by subdividing each EELS map pixel into 16×16 imaging pixels, each $0.32 \text{ nm} \times 0.32 \text{ nm}$. Figs. 5-8(a,b) show the layer count maps derived from HAADF imaging and EELS mapping, respectively. The upper left half of the field of view is a 4-layer thick, as determined by both techniques. To the lower right is a belt where the layer count is determined to be 8 by HAADF imaging but 9 by EELS mapping. The bottom right corner is a vacuum region. A natural explanation is that the 4-layer flake folded onto itself, resulting in a doubled layer count (8 layers). The +1 layer error in the folded region by EELS mapping can be attributed to solid-state effects in the crystalline sample not accounted for in our layer count quantification procedure. Additionally, this technique is only accurate to 10% of sample thickness so the discrepancy is expected.

5.4 Conclusion

For few-layer 2D materials, the thickness is represented by an integer layer count. Uniformity of the layer count and in some cases control over its exact value is critical to their electronic device applications. Accurate and high spatial resolution (nanometer level) measurement of layer count for few-layer 2D materials has been lacking. Two complementary techniques, both based on TEM, to accurately map the layer count of few-layer h-BN at high spatial resolution are demonstrated. By HAADF imaging in the STEM mode, layer count mapping at a 0.25 nm lateral spatial resolution is achieved. Unavoidable surface contamination, however, corrupts the layer count measurement in the contaminated areas. To overcome this difficulty, a “see-through-the junk” technique based on EELS takes advantage of the absence of B in surface contamination to

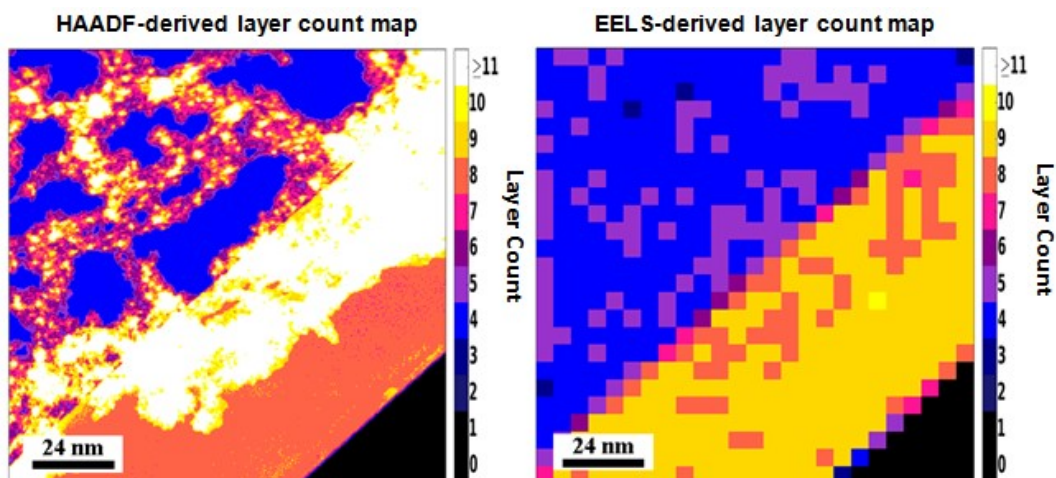


Figure 5-8. Layer count maps of an h-BN flake exfoliated from bulk. (a) From HAADF imaging. (b) From EELS mapping. These maps indicate that a 4 layer flake folds onto itself, resulting in the 8-layer region, which is slightly overestimated to be 9 layers by EELS.

map the true layer count of h-BN by quantitatively analyzing the B K-edge spectrum of each pixel of the EELS map. Limited by the spatial resolution of EELS mapping, the pixel size is 16 nm. In contamination-free areas, the two methods highly agree with each other. The nonuniformity in layer count of the h-BN grown by CVD on Cu under study is revealed. The method to determine layer count and its spatial variation provide a measurement tool for developing h-BN growth methods that result in controlled thickness and uniformity thereof. The method is applicable to other 2D materials. For transition metal dichalcogenides, for example, the influence of the organic contamination on the first technique based on HAADF imaging will be negligibly small due to the large atomic numbers of the constituent elements compared to C and other elements in usual organic contaminants, while the second techniques may yield less reliable results for reasons that have been discussed. The demonstrated method paves the way towards the synthesis of multilayer 2D materials with homogeneous layer count.

5.5 Experimental methods

5.5.1 CVD growth of h-BN films

Commercial copper foils (99.9%, 20 μm thick, Nilaco) were used for the growth of h-BN thin films. The growth was performed with a commercial CVD system (OTF-1200X-80-II-4CV-PE-SL, MTI) with a 2 in. diameter quartz tube. The Ar and H_2 were ultra-high purity (UHP) grade gases, supplied by Airgas. Before growth, copper foils were first electropolished for 90 sec in a solution containing 20 mL of D.I. water, 10 mL of orthophosphoric acid, 10 mL of ethanol, 1 mL of isopropyl alcohol and 0.2 g of urea.³³ The electropolished foils were then loaded into a quartz tube (2'' diameter), which was first pumped down to the base pressure and then back-filled with Ar. This process was repeated three times. Copper foils were then annealed for 1 hr at

1050 °C under 200 sccm of H₂ and 1000 sccm of Ar, at atmospheric pressure. After annealing, the furnace was opened for cooling down without changing gas flows. Foils were unloaded at room temperature. For h-BN synthesis, the annealed copper foils were loaded again into a separate quartz tube (2'' diameter), which was first pumped down to the base pressure and then back-filled with Ar. This process was repeated three times. At atmospheric pressure, H₂ and Ar flows were adjusted to 100 and 900 sccm, respectively. The temperature was first ramped up to 1000 °C in 50 minutes and then to 1040 °C in 10 minutes. Then H₂ and Ar flows were adjusted to 100 and 400 sccm, respectively. To initiate h-BN growth, 20 mg of ammonia-borane^{10,12,13} was sublimed for 20 minutes at ~120°C, using an external heating belt. After the h-BN growth, the furnace was opened for rapid cooling without changing gas flows. Foils were unloaded around 50°C under Ar ambient.

5.5.2 Transfer of h-BN films onto TEM Grids

The h-BN films need to be transferred onto TEM grids for STEM imaging and EELS analysis. To reduce carbon contamination, a direct-transfer technique³⁴ was used to transfer h-BN films onto the transmission electron microscopy (TEM) grids. Briefly, a holey carbon membrane-covered Au TEM grid was placed facing down onto the h-BN covered copper foil. A few drops of isopropyl alcohol were then placed on the TEM grids and allowed to dry naturally for ~ 15 minutes. Afterward, to enhance the adhesion between the holey carbon and h-BN films, the TEM grids were heated on a hot plate at 120 °C for 20 minutes. The underlying Cu foil was etched away by a commercial etchant (CE-100, Transene). The etching time was ~ 60 minutes. The TEM grids were then floated for ~12 hours on the surface of a solution of commercial hydrochloric acid 1:1 diluted in de-ionized (DI) water.³⁵ The TEM grid was then further floated on three D.I. water baths and allowed to dry. In order to reduce organic contamination, the TEM

grids were briefly annealed in the air (200 °C for 30 min), prior to inserting into the TEM.³⁵

5.5.3 Microscopy and microanalysis

Scanning electron microscope (SEM) images of h-BN on Cu were acquired with an LEO 1525 SEM operated at 5kV before being transferred to TEM grids. After the transfer, TEM characterization was performed with a Libra MC 200 TEM with an electron monochromator, capable of sub-200 meV energy resolution, and a Kohler illumination system. The TEM was operated at 200 kV in STEM mode. The in-column 90° filter was used with an energy dispersion of 0.411 eV when collecting EELS data. The collection semi-angle (β) was 20.6 mrad, and the convergence semi-angle (α) was 9 mrad. For HAADF imaging, the camera length was chosen to be 1200 mm which results in an inner angle of the HAADF detector to be about 100 mrad (corresponding to $\sim 40 \text{ nm}^{-1}$ reciprocal distance) and the outer angle was 300 mrad. The HAADF images were acquired simultaneously with the EELS map but at different spatial resolutions. For the CVD grown h-BN, the $529 \text{ nm} \times 529 \text{ nm}$ field of view contains 1920×1920 HAADF image pixels, each roughly $0.28 \text{ nm} \times 0.28 \text{ nm}$. To ensure sufficient signal-to-noise ratio for EELS mapping, 64×64 HAADF image pixels are binned into one EELS map pixel, roughly $17.6 \text{ nm} \times 17.6 \text{ nm}$ in size. Therefore the EELS map is a 30×30 array. A raster scan is performed within each 64×64 array of HAADF image pixels. Each EELS spectrum had a dwell time of 1.5 s, corresponding to a dwell time of 366 μs for each HAADF pixel. The extended dwell time of EELS acquisition yields high count values and signal-to-noise ratios.

5.5.4 EELS data analysis

The basis for the analysis of EELS data is:

$$N = \frac{\frac{\Delta I_K(E)}{\Delta E} / I_0}{\frac{d\sigma}{dE}}, \quad (1)$$

where N is the areal density of atoms of the element to be analyzed, $\Delta I_K(E)$ the intensity (counts) at energy loss E of the core-loss edge corresponding to the element to be analyzed, ΔE the energy dispersion of the energy channel, I_0 the intensity (total counts) of the incident electron beam, and $d\sigma/dE$ the energy-differential scattering cross-section of the element. A core-loss edge in an EELS spectrum gives the inelastic scattering probability by electrons occupying, in this case, the boron K-shell. Here, $\Delta I_K(E)$ is the core-loss spectra after background removal, the procedure of which is discussed in detail in Results and Discussion. The total current of the probe is found by a Ronchigram in a vacuum and having the CCD camera of the TEM calibrated for conversion between counts and electrons. The ionization edge energy-differential scattering cross-section $d\sigma/dE$ is modeled by the x-ray photoabsorption (XRPA) theory, which is very reliable.³⁶ Collection angle correction according to the cross-section of Egerton was used.³⁷ In this work, we do not account for plural scattering, because the film thickness is significantly less than 10 nm.²⁹ However, if this experiment is to be replicated with thicker samples, this effect would be accounted for by convoluting the low-loss spectrum with modeled ionization edge. The inelastic scattering probability $[\Delta I_K(E)/\Delta E]/I_0$ is divided by the cross-section $d\sigma/dE$ (i.e., inelastic scattering probability for a single atom) to obtain the areal density of B atoms, which is then converted to h-BN layer count, with the known areal density of B atoms in an h-BN monolayer. EELS maps were analyzed with Quantifit, a Python program for EELS data analysis.³⁸

5.6 References

- (1) Splendiani, A.; Sun, L.; Zhang, Y.; Li, T.; Kim, J.; Chim, C.-Y.; Galli, G.; Wang, F. Emerging Photoluminescence in Monolayer MoS₂. *Nano Lett.* **2010**, *10*, 1271–1275.
- (2) Geim, A. K.; Grigorieva, I. V. Van der Waals Heterostructures. *Nature* **2013**, *499*, 419 - 425.
- (3) Dean, C. R.; Young, A F.; Meric, I.; Lee, C.; Wang, L.; Sorgenfrei, S.; Watanabe, K.; Taniguchi, T.; Kim, P.; Shepard, K. L.; *et al.* Boron Nitride Substrates for High-Quality Graphene Electronics. *Nat. Nanotech.* **2010**, *5*, 722–726
- (4) Britnell, L.; Gorbachev, R. V.; Geim, A. K.; Ponomarenko, L. A.; Mishchenko, A.; Greenaway, M. T.; Fromhold, T. M.; Novoselov, K. S.; Eaves, L. Resonant Tunnelling and Negative Differential Conductance in Graphene Transistors. *Nat. Comm.* **2013**, *4*, 1794.
- (5) Britnell, L.; Gorbachev, R. V.; Jalil, R.; Belle, B. D.; Schedin, F.; Mishchenko, A.; Georgiou, T.; Katsnelson, M. I.; Eaves, L.; Morozov, S. V.; Peres, N. M. R.; Leist, J.; Geim, A. K.; Novoselov, K. S.; Ponomarenko, L. A. Field-Effect Tunneling Transistor Based on Vertical Graphene Heterostructures *Science* **2012**, *335*, 947–950.
- (6) Roy, T.; Liu, L.; Chakrabarti, B.; Hesabi, Z. R.; Joiner, C. A.; Feenstra, R. M.; Gu, G.; Vogel, E. M. Tunneling characteristics in chemical vapor deposited graphene–hexagonal boron nitride–graphene junctions. *Appl. Phys. Lett.* **2014**, *104*, 123506.
- (7) Dean, C. R.; Young, A F.; Meric, I.; Lee, C.; Wang, L.; Sorgenfrei, S.; Watanabe, K.; Taniguchi, T.; Kim, P.; Shepard, K. L.; *et al.* Boron Nitride Substrates for High-Quality

Graphene Electronics. *Nat. Nanotech.* **2010**, *5*, 722–726.

(8) Kubota, Y.; Watanabe, K.; Tsuda, O.; Taniguchi, T. Deep Ultraviolet Light-Emitting Hexagonal Boron Nitride Synthesized at Atmospheric Pressure. *Science* **2007**, *317*, 932–935.

(9) Shi, Y.; Hamsen, C.; Jia, X.; Kim, K. K.; Reina, A.; Hofmann, M.; Hsu, A. L.; Zhang, K.; Li, H.; Juang, Z. Y.; Dresselhaus, M. S.; Li, L. J.; Kong, J. Synthesis of Few-Layer Hexagonal Boron Nitride Thin Film by Chemical Vapor Deposition. *Nano Lett.* **2010**, *10*, 4134–4139.

(10) Song, L.; Ci, L.; Lu, H.; Sorokin, P. B.; Jin, C.; Ni, J.; Kvashnin, A. G.; Kvashnin, D. G.; Lou, J.; Yakobson, B. I.; Ajayan, P. M. Large Scale Growth and Characterization of Atomic Hexagonal Boron Nitride Layers. *Nano Lett.* **2010**, *10*, 3209–3215.

(11) Ismach, A.; Chou, H.; Ferrer, D. A.; Wu, Y.; McDonnell, S.; Floresca, H. C.; Covacevich, A.; Pope, C.; Piner, R.; Kim, M. J.; Wallace, R. M.; Colombo, L.; Ruoff, R.S. Toward the Controlled Synthesis of Hexagonal Boron Nitride Films. *ACS Nano* **2012**, *6*, 6378–6385.

(12) Lee, K. H.; Shin, H.; Lee, J.; Lee, I.; Kim, G.; Choi, J.; Kim, S. Large-Scale Synthesis of High-Quality Hexagonal Boron Nitride Nanosheets for Large-Area Graphene Electronics. *Nano Lett.* **2012**, *12*, 714–718.

(13) Kim, K. K.; Hsu, A.; Jia, X.; Kim, S. M.; Shi, Y.; Dresselhaus, M.; Palacios, T.; Kong, J. Synthesis and Characterization of Hexagonal Boron Nitride Film as a Dielectric Layer for Graphene Devices. *ACS Nano* **2012**, *6*, 8583–8590.

(14) Gao, Y.; Ren, W.; Ma, T.; Liu, Z.; Zhang, Y.; Liu, W.; Ma, L-P.; Ma, X.; Cheng, H. Repeated and Controlled Growth of Monolayer, Bilayer and Few-Layer Hexagonal Boron

Nitride on Pt Foils. *ACS Nano* **2013**, 7, 5199–5206

- (15) Song, Y.; Zhang, C.; Li, B.; Jiang, D.; Ding, G.; Wang, H.; Xie, X. Triggering the Atomic Layers Control of Hexagonal Boron Nitride Films. *Appl. Surf. Sci.* **2014**, 313, 647–653.
- (16) Kim, S. M.; Hsu, A.; Park, M. H.; Chae, S. H.; Yun, S. J.; Lee, J. S.; Cho, D.-H.; Fang, W.; Lee, C.; Palacios, T.; Dresselhaus, M.; Kim, K. K.; Lee, Y. H.; Kong, J. Synthesis of Large-Area Multilayer Hexagonal Boron Nitride for High Material Performance. *Nat. Commun.* **2015**, 6, 8662.
- (17) Chopra, N.G.; Luyken, R.J.; Cherrey, K.; Crespi, V.H.; Cohen, M.L.; Louie, S. G.; Zettl, A. Boron Nitride Nanotubes. *Science* **1995**, 269, 966-967.
- (18) Gorbachev, R. V.; Riaz, I.; Nair, R. R.; Jalil, R.; Britnell, L.; Belle, B. D.; Hill, E. W.; Novoselov, K. S.; Watanabe, K.; Taniguchi, T.; Geim, A. K.; Blake, P. Hunting for Monolayer Boron Nitride: Optical and Raman Signatures. *Small* **2011**, 7, 465–468.
- (19) Srivastava, N.; Gao, Q.; Widom, M.; Feenstra, R. M.; Nie, S.; McCarty, K. F.; Vlassiounk, I. V. Low-energy electron reflectivity of graphene on copper and other substrates. *Phys. Rev. B* **2013**, 87, 245414.
- (20) Ismach, A.; Chou, H.; Mende, P.; Dolocan, A.; Addou, R.; Aloni, S.; Wallace, R.; Feenstra, R.; Ruoff, R.S.; Colombo, L. Carbon-assisted chemical vapor deposition of hexagonal boron nitride *2D Mater.* **2017**, 4, 025117.
- (21) Crewe, A. V.; Wall, J.; Langmore, J. Visibility of Single Atoms. *Science* **1970**, 168, 1338-1340.

- (22) LeBeau, J. M.; Findlay, S. D.; Stemmer, S. Quantitative Atomic Resolution Scanning Transmission Electron Microscopy. *Phys. Rev. Lett.* **2008**, *100*, 206101.
- (23) Wang, Z. W.; Li, Z. Y.; Palmer, R. E. Quatitative Z-Contrast Imaging in the Scanning Transmission Electron Microscope with Size-Selected Clusters. *Phys. Rev. B* **2011**, *84*, 073408.
- (24) Pennycook, S.J. Z-Contrast STEM for Materials Science. *Ultramicroscopy* **1989**, *30*, 58-69.
- (25) Zhan, Y.; Liu, Z.; Najmaei, S.; Ajayan, P. M.; Lou, J. Large-Area Vapor-Phase Growth and Characterization of MoS₂ Atomic Layers on a SiO₂ Substrate. *Small* **2012**, *8*, 966–971.
- (26) Li, X.; Cai, W.; An, J.; Kim, S.; Nah, J.; Yang, D.; Piner, R.; Velamakanni, A.; Jung, I.; Tutuc, E.; Banerjee, S. K.; Colombo, L.; Ruoff, R. S. Large-Area Synthesis of High-Quality and Uniform Graphene Films on Copper Foils. *Science* **2009**, *324*, 1312–1314.
- (27) Verbeeck, J.; Van Aert, S. Model Based Quantification of EELS Spectra. *Ultramicroscopy* **2004**, *101*, 207–224.
- (28) Pease, R.S. An X-ray Study of Boron Nitride. *Acta Cryst.* **1952**, *5*, 356-361.
- (29) Egerton, R.F. Electron energy-loss spectroscopy in the TEM. *Rep. Prog. Phys.* **2009**, *72*, 016502.
- (30) Graboski, M.S.; McCormick, R.L. Combustion of Fat and Vegetable Oil Derived Fuels in Diesel Engines. *Prog. Energy Combust. Sci.* **1998**, *24*, 125-164.
- (31) Lu, G.; Wu, T.; Yuan, Q.; Wang, H.; Wang, H.; Ding, F.; Xie, X.; Jiang, M. Synthesis of

Large Single-Crystal Hexagonal Boron Nitride Grains on Cu-Ni Alloy. *Nature Commun.* **2015**, *6*, 6160.

(32) Malis, T.; Cheng, S. C.; Egerton, R. F. EELS Log-Ratio Technique for Specimen-Thickness Measurement in the TEM. *J. Electron Microsc. Tech.* **1988**, *8*, 193–200.

(33) Zhang, B.; Lee, W. H.; Piner, R.; Kholmanov, I.; Wu, Y.; Li, H.; Ji, H.; Ruoff, R.S. Low-Temperature Chemical Vapor Deposition Growth of Graphene from Toluene on Electropolished Copper Foils. *ACS Nano* **2012**, *6*, 2471–2476.

(34) Regan, W.; Alem, N.; Alemán, B.; Geng, B.; Girit, Ç.; Maserati, L.; Wang, F.; Crommie, M.; Zettl, A. Direct Transfer of Layer-Area Graphene. *Appl. Phys. Lett.* **2010**, *96*, 11–13.

(35) Meyer, J. C.; Kurasch, S.; Park, H. J.; Skakalova, V.; Künzel, D.; Groß, A.; Chuvilin, A.; Algara-Siller, G.; Roth, S.; Iwasaki, T.; Starke, U.; Smet, J. H.; Kaiser, U.; Gross, A. Experimental Analysis of Charge Redistribution due to Chemical Bonding by High-Resolution Transmission Electron Microscopy. *Nat. Mater.* **2011**, *10*, 209–215.

(36) Henke, B.L.; Gullikson, E.M.; Davis, J.C. X-ray interactions: Photoabsorption, scattering, transmission, and reflection at E=50-30000 eV, Z=1-92. *At. Data Nucl. Data Tables* **1993**, *54*, 181-342.

(37) Egerton, R.F. Oscillator-strength parameterization of inner-shell cross sections. *Ultramicroscopy* **1993**, *50*, 13-28.

(38) Duscher, G. Quantifit. <http://web.utk.edu/~gduscher/Quantifit/> (Accessed June 22, 2018).

CHAPTER 6

STUDY OF THE INTRINSIC BEHAVIOR OF PALLADIUM DISELENIDE FIELD-EFFECT TRANSISTORS

6.1 Abstract

The overall behavior of an FET device is determined not only by the electron or hole-dominant nature of the channel, but also by the effect of contacts. Very often in device studies, both of these factors are entangled. In this work, we untangle these factors to show that few-layer palladium diselenide based FET has an *intrinsic* n-type conduction. Control set of devices reveal that when the channel is fully encapsulated and the channel:contact interface is kept intrinsic during device fabrication, the as-fabricated PdSe₂ FET shows dominant n-type conduction, and this device behavior is not due to the preferred electron-injection behavior of the contacts, rather it is the intrinsic behavior of the channel itself. Further it is revealed that by engineering the metal:semiconductor interface alone, it is possible to shift the overall FET device behavior from ambipolar to n-type conduction, without changing the intrinsic nature of the channel itself

6.2 Introduction

Graphene is the most widely studied two-dimensional (2D) material,¹ but the absence of bandgap makes it less attractive for the applications that require a finite bandgap e.g. FET device for logic applications.² Apart from graphene, another extensively studied 2D semiconducting material is molybdenum disulfide (MoS₂),³ which belongs to a family of layered- materials known as transition metal dichalcogenides: MX₂, where M represents a transition element and X is a halogen.⁴ In transition metal dichalcogenides, a layer of transition metal atoms is sandwiched between a layer of halogen atoms through strong covalent bonds.^{3,4} This stack of three layers is held together by weak van der Waals forces, thus allowing for the exfoliation of these materials.^{3,4} Recently, research has expanded into other less-studied members of this family.⁵ One of the new members of this family with crystal structure deviating from the conventional

transition metal dichalcogenides is palladium diselenide (PdSe_2).^{6,7} The monolayer PdSe_2 is predicted to have a bandgap of 1.1 eV, and a high electron mobility of $\sim 42000 \text{ cm}^2/\text{Vsec}$.⁶ PdSe_2 has a layered structure consisting of PdSe_4 tetragons that are held together by strong covalent bonds, forming a wavy structure.⁷ There is no covalent bonding in between the layers, which is a characteristic of layered transition metal dichalcogenides.⁷ The key difference, however, between a conventional MX_2 and PdSe_2 is that palladium atoms in later are four-fold coordinated, while M atoms in MX_2 are six-fold coordinated.⁷ PdSe_2 exhibits layer dependent bandgap,⁸ like the other semiconducting transition metal dichalcogenides,⁹ but with an important difference that bulk PdSe_2 has an almost negligible bandgap,^{8,10} while few-layer PdSe_2 forms a narrow-bandgap semiconductor.^{7,8}

Very recently, bulk crystals of PdSe_2 have been synthesized, and subsequently exfoliated down to few-layers by Chow *et al.*⁷ Early FET devices based on few-layers PdSe_2 with Ti/Au top-contacts revealed ambipolar characteristics at room temperature.^{7,8} After low-temperature vacuum-annealing at 450K, Chow *et al.* observed that the PdSe_2 FET devices showed a predominant n-type conduction, with an increased electron mobility.⁷ Similar improvement in the n-type conduction has been observed by low-temperature vacuum-annealing in case of WSe_2 FETs with Ti as top-contacts.¹¹ Qiu *et al.* argued that oxygen preferentially binds to the defect sites in the basal plane of MoS_2 , leading to the p-doping of the later. After low-temperature vacuum-annealing, such oxygen is desorbed, resulting in the recovery of n-type device conduction.¹² Chow *et al.* also argued that the desorption of surface adsorbates after vacuum annealing was responsible in a shift of their FET device behavior from ambipolar to n-type conduction.⁷ Since the early results on PdSe_2 based FET devices were affected by the extrinsic factors,^{7,8} the intrinsic behavior of the FET devices based on this newly discovered material is

not known, thus requiring further investigation.

The overall FET device behavior is determined not only by the intrinsic nature of the channel material but also by the contacts as well, and quite often these factors are enmeshed. In this chapter, control devices are designed to untangle the effect of contamination on the channel and contact properties in determining the overall device behavior of PdSe₂-based FET. The PdSe₂ FET device in which channel is fully encapsulated during device fabrication shows a dominant n-type conduction in the as-fabricated state, and at ambient temperature. In a control device, when only the PdSe₂ channel is purposely contaminated during device fabrication while keeping the rest of the fabrication steps constant, the device behavior becomes p-type pointing to the fact that the observed n-type conduction of the fully encapsulated device was not due to the preferred electron-injection behavior of the contacts rather it is the intrinsic behavior of the channel itself. Further, it is revealed that by changing the electronic properties of Ti:PdSe₂ interface by performing Ar⁺ ion bombardment on the later, it is possible to change the overall device behavior from ambipolar to n-type conduction, without changing the channel behavior.

6.3 Results and discussion

To clarify the origin of the observed ambipolar device behavior of the as-fabricated PdSe₂ FET in earlier reports, four types of devices were studied in this report as shown by the schematics in Fig. 6-1. Fig. 6-1a shows a graphic representation of the side-view of fully encapsulated (type 1) device. The important characteristic of this architecture is that the top surface of PdSe₂ channel, and the PdSe₂: few-layer graphene (FLG) interface, never see any extrinsic contamination during the device processing,^{13,14} as will be shown later. Thus, an intrinsic van der Waals interface exists between PdSe₂ and FLG. Also, due to the inherent 2D nature of FLG and PdSe₂ flakes, the

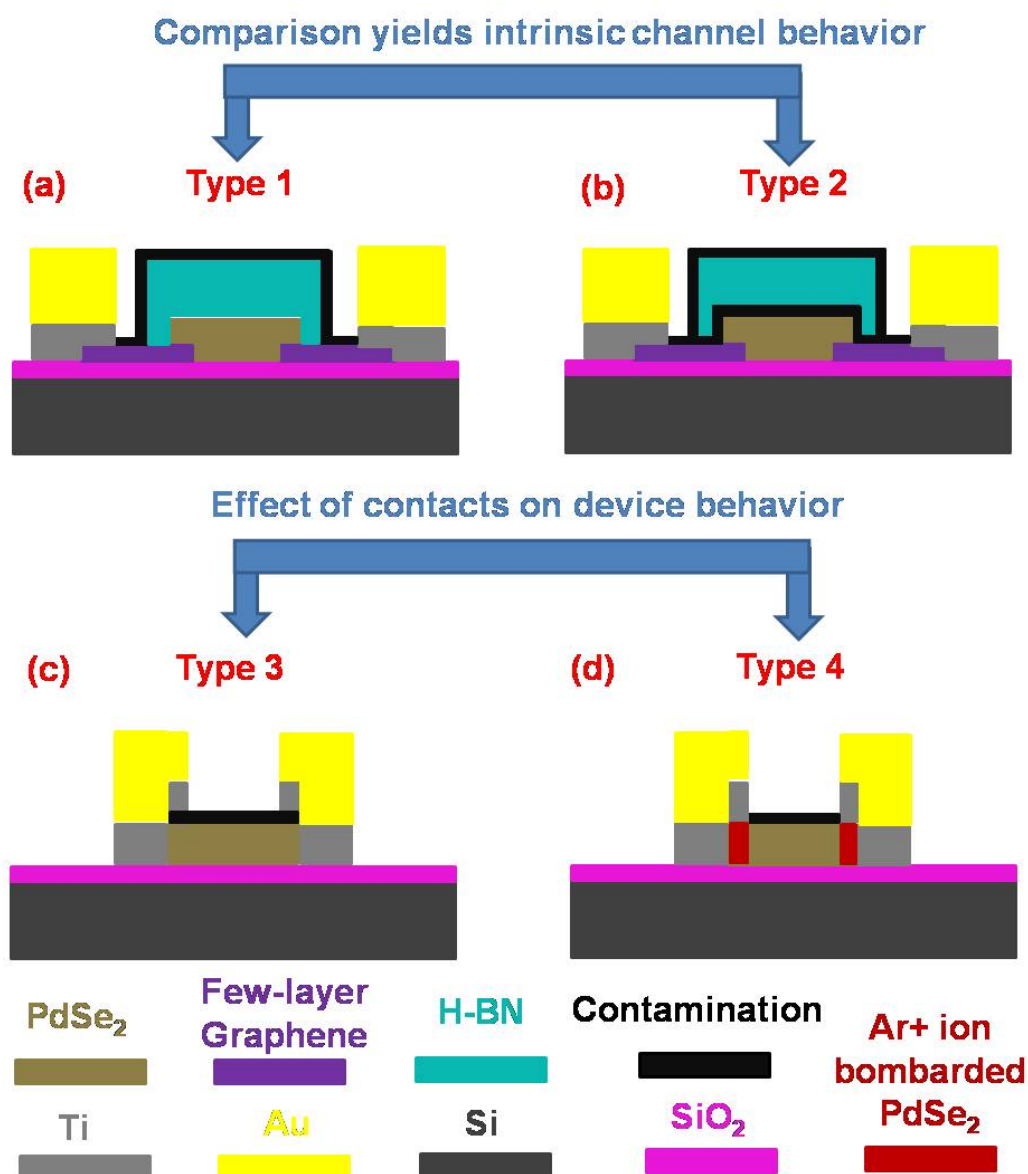


Figure 6-1. Type of FET devices studied to understand the origin of ambipolar conduction in PdSe₂ based FET. (a) Fully encapsulated (type 1) device. (b) Type 2 device, which is very similar to the type 1 device except that the top surface of PdSe₂ channel was purposely contaminated during device processing. (c) Ti/Au top-contacted (type 3) device (d) Type 4 device where the contact region between Ti and PdSe₂ is cleaned by successive oxygen plasma, and Ar⁺ ion bombardment, before metal deposition.

possibility of Fermi-level pinning, as in the case of transition metal dichalcogenides and 3D metal contacts¹⁵ is also precluded.¹⁶

To rule out the effect of FLG-contacts in introducing any asymmetry in the device characteristics due to preferred electron or hole injection into PdSe₂ channel, a type 2 device was studied as shown by the schematics in Fig. 6-1b. Compared to the type 1 device, the key difference here is that the top surface of PdSe₂ was first purposely processed by a dummy photolithography step, and then later by the polycarbonate (PC) processing. The dummy photolithography step was performed first to mimic the device fabrication procedure in ref. 7, where the channel sees the photolithography residue during device processing, while the PC was used to pick-up the PdSe₂ flake from the source substrate onto the pre-exfoliated FLG flakes on the target substrate.¹⁷ The device characteristics to be presented later will reveal that this processing strongly suppresses the dominant n-type conduction of PdSe₂ device that was observed in case of type 1 device. It is worth noting here the contact region between PdSe₂ and FLG in this device is also intrinsic, similar to type 1 device, so by comparing the device behavior of these two type of devices, we can deduce the intrinsic behavior of PdSe₂ channel. The contaminated PdSe₂ flake in type 2 device was also encapsulated by a top BN flake. This step was included to preserve the effect of contamination on the channel during the rest of the device processing while making electrical contacts to the FLG electrodes.

Fig. 6-1c shows a schematic of Ti/Au top-contacted PdSe₂ (type 3) device, having the same architecture as the one studied by Chow *et al.*⁷ It is worth mentioning here that the interface between PdSe₂ and Ti in this device may be contaminated with photoresist residue, which is introduced during photolithography step before the deposition of Ti/Au as top contacts. To mitigate the effect of such contamination on device characteristics, a type 4 device was studied

as well as shown by the schematic in Fig. 6-1d, where the contact region between PdSe₂ and the metal electrode was cleaned by the successive oxygen plasma,¹⁸ and Ar⁺ ion bombardment,¹⁹ with photoresist acting as a mask to protect the channel region. It is worth emphasizing here that the channel region of both type 3 and 4 devices, see the same effect of photolithography processing, while the only difference is between the Ti: PdSe₂ interface. Thus by comparing, the behavior of these two type of device we can deduce the effect of contacts in determining the overall device behavior.

Next, we detail the fabrication steps for the four type of devices. Fig. 6-2 shows the steps involved in the fabrication of type 1 device. Fig. 6-2a shows the first step, where the FLG flakes are exfoliated on a 285 nm SiO₂/Si substrates by a scotch-tape.²⁰ Since the FLG flakes are exfoliated from the bulk graphite flakes on the scotch tape, the top surface of FLG is clean and does not require any solvent cleaning step to remove any tape residues.²¹ Next, the PdSe₂ flakes are exfoliated on another 285 nm SiO₂/Si substrates, as shown in Fig. 6-2b. It is worth mentioning here that before the exfoliation of FLG, PdSe₂, and h-BN flakes in this study, all the starting 285 nm SiO₂/Si substrates in this study were treated with oxygen plasma, following the solvent cleaning step. This treatment which is well known to leave SiO₂ surface hydrophilic, due to the presence of OH-terminated functional groups,¹⁸ and is different compared to the refs. 7 and 8, where no such treatment was performed on SiO₂/Si substrates, prior to the exfoliation of PdSe₂.²² Fig. 6-2c shows the h-BN flake after it is picked by a PDMS/PC stamp.¹⁷ It is worth noting here that the bottom side of h-BN, that was originally in contact with the clean SiO₂ surface will make contact with thin PdSe₂ flakes in the next step, and only the top side of h-BN gets contaminated by the PC processing. Fig. 6-2d, shows the PC/h-BN/PdSe₂ stack, landed on the pre-exfoliated FLG flakes from the first step. Only the part of PdSe₂, outlined by a red

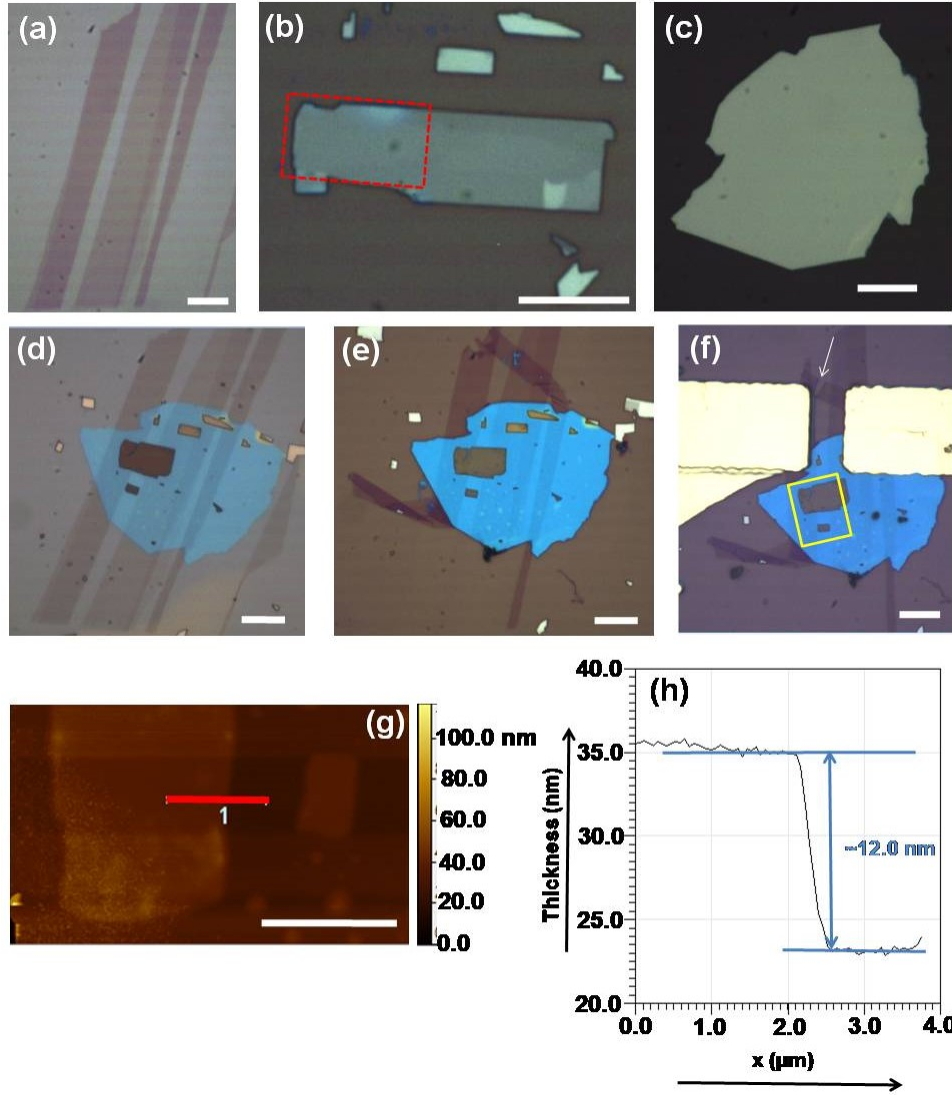


Figure 6-2. Fabrication procedure for the fully encapsulated (type 1) device. (a) As-exfoliated FLG flakes on an oxygen plasma cleaned 285 nm SiO₂/Si substrate. (b) As-exfoliated PdSe₂ flakes on an oxygen plasma cleaned 285 nm SiO₂/Si substrate (c) H-BN flake picked up by a PC/PDMS stamp. (d) PC/h-BN/PdSe₂ stack landed onto FLG from Fig. 6-2a. (e) Stack after the removal of PC by solvents. (f) Ti/Au contacts are made to FLG by standard photolithography and metal lift-off procedure. (g) AFM height mapping of the PdSe₂ flake, highlighted by the yellow-boxed region in Fig. 6-2f. (h) Line profile taken across the red line in Fig. 6g. Scale bars are 10 μm in panels a-f, and 5 μm in panel g.

contour in Fig. 6-2b was picked up by the PDMS/PC/h-BN stamp. Also, the bottom side of PdSe₂ that was originally in contact with the clean SiO₂ surface on the source substrate, makes contact with the top clean surface of FLG. Fig. 6-2e shows the stack after the removal of PC by solvents. Some part of FLG was lifted-off after this step, due to the stronger interaction between thick PC and FLG, and folded onto the other FLG-electrode. The device structure was completed by a standard photolithography and metal lift-off procedure to make Ti/Au contacts with FLG, as shown in Fig. 6-2f. The portion of FLG that had folded-over in the previous step was burnt by Joule heating,²³ before the device measurement, as shown by the white arrow in Fig. 6-2f. Fig. 6-2g shows the AFM height mapping of the encapsulated PdSe₂ flake, which is highlighted by the yellow-boxed region in Fig. 6-2f. Fig. 6-2h shows the height profile taken across the red line in Fig. 6-2g. The thickness of this PdSe₂ flake is ~ 12.0 nm, with an estimated bandgap of ~ 0.2 eV⁸

Next, we show the steps involved in the fabrication of type 2 device in Fig. 6-3. Fig. 6-3a shows the starting FLG flakes exfoliated on an oxygen plasma cleaned 285 nm SiO₂/Si substrates by a scotch-tape. Next, the PdSe₂ flakes are exfoliated on another oxygen plasma cleaned 285 nm SiO₂/Si substrates, as shown in Fig. 6-3b. Now a dummy photolithography step was performed on the as-exfoliated PdSe₂ flake in Fig. 6-3b, where a photoresist was spin-coated, flood-exposed and developed subsequently. Then the PdSe₂ flake was picked-up by a PDMS/PC stamp and landed on the FLG flakes, which is shown in Fig. 6-3c after PC removal. Only the part of PdSe₂ flake, outlined by a red contour in Fig. 6-3b was picked-up by the PDMS/PC stamp. Fig. 6-3d shows the as-exfoliated h-BN flake on another oxygen plasma cleaned 285 nm SiO₂/Si substrate. This h-BN flake was picked-up by another PDMS/PC stamp and landed on the PdSe₂/FLG stack from Fig. 6-3c. Fig. 6-3e shows the h-BN/PdSe₂/FLG stack after PC removal. Fig. 6-3f shows the final device after making Ti/Au contacts with FLG using photolithography

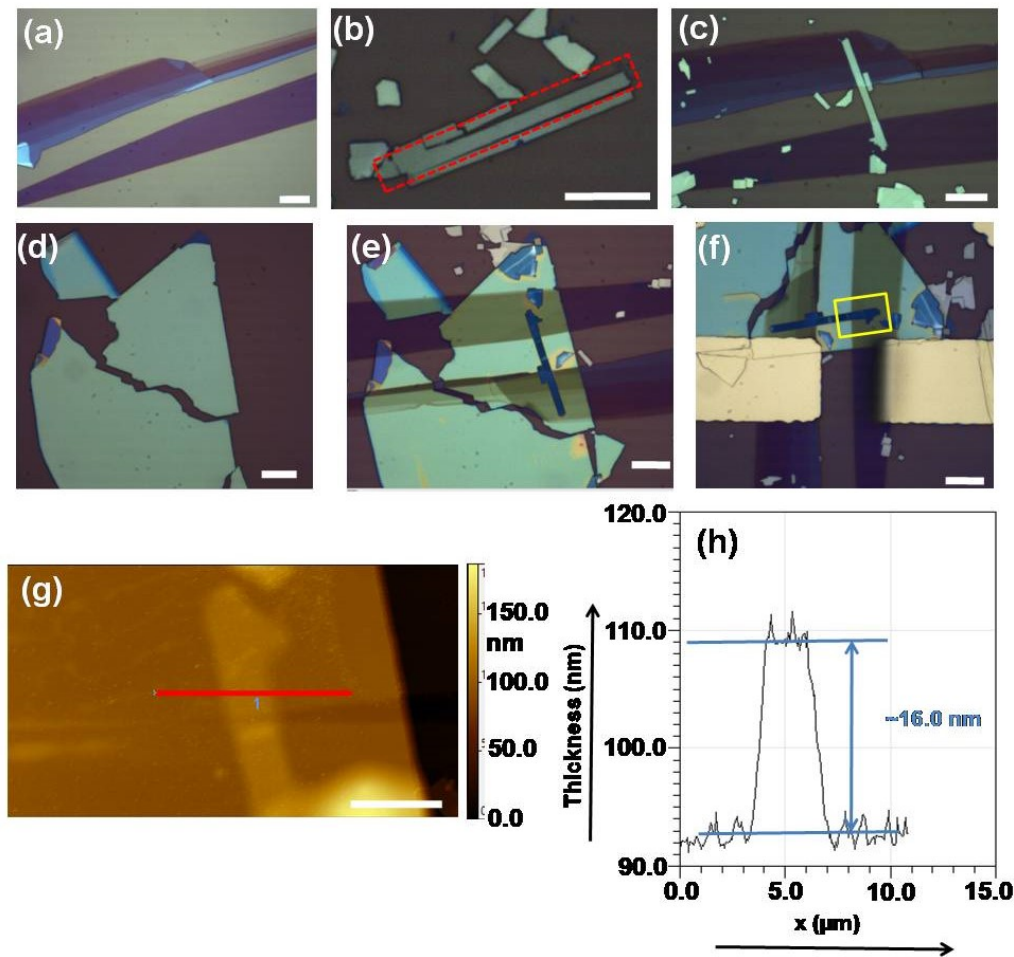


Figure 6-3. Fabrication procedure for purposely contaminated type 2 device. (a) As-exfoliated FLG flakes on an oxygen plasma treated 285 nm SiO₂/Si substrate. (b) As-exfoliated PdSe₂ flakes on an oxygen plasma cleaned 285 nm SiO₂/Si substrate. (c) A dummy photolithography step is first performed on the PdSe₂ flake in Fig. 6-3b, and then landed on the FLG flakes from Fig. 6-3a, using a PDMS/PC stamp. PdSe₂/FLG stack after PC removal by solvents. (d) As-exfoliated h-BN flake on an oxygen plasma cleaned 285 nm SiO₂/Si substrate. (e) H-BN flake transferred onto the PdSe₂/FLG stack in Fig. 6-3c. (f) Ti/Au contacts are made to the FLG by standard photolithography and metal lift-off procedure. (g) AFM height mapping of the PdSe₂ flake, highlighted by the yellow-boxed region in Fig. 6-3f. (h) Line profile taken across the red line in Fig. 6-3g. Scale bars are 10 μm in panels a-f, and 5 μm in panel g.

and metal lift-off procedure. Fig. 6-3g shows the AFM height mapping of the encapsulated PdSe₂ flake, which is highlighted by the yellow-boxed region in Fig. 6-3f. Fig. 6-3h shows the height profile taken across the red line in Fig. 6-3g. The thickness of this PdSe₂ flake is ~ 16.0 nm. It is worth mentioning here that there might be some residues on this PdSe₂ flake due to the processing steps introduced purposely before the h-BN encapsulation, therefore, the thickness of the PdSe₂ flake as measured by AFM may not be very accurate.

Next, we detail the fabrication of type 3 device in Fig. 6-4. Fig. 6-4a shows the starting PdSe₂ flakes exfoliated on an oxygen plasma cleaned 285 nm SiO₂/Si substrate. Fig. 6-4b shows the device structure after making Ti/Au top contacts to PdSe₂ using photolithography and metal lift-off procedure. Fig. 6-4c shows the AFM height mapping of the PdSe₂ flake, which is highlighted by the yellow-boxed region in Fig. 6-4b. Fig. 6-4d shows the height profile taken across the red line in Fig. 6-4b. The thickness of this PdSe₂ flake is ~ 18.0 nm, but since this PdSe₂ flake had seen photolithography process, this thickness may not be accurate due to the presence of possible photolithography residues.

Fig. 6-5 shows the steps involved in the fabrication of type 4 device. Fig. 6-5a shows the starting as-exfoliated PdSe₂ flakes on an oxygen plasma cleaned 285 nm SiO₂/Si substrate. Next, a photoresist was used as a mask to define the contacts regions on the PdSe₂ channel, as shown in Fig. 6-5b. Fig. 6-5c shows the contact areas of PdSe₂ after successive oxygen plasma, and Ar⁺ ion bombardment. Finally, the device structure is completed by depositing Ti/Au as top contacts to the bombarded PdSe₂ region, using photolithography and metal lift-off procedure, as shown in Fig. 6-5d.

As mentioned earlier, low-temperature annealing has been reported to change the device

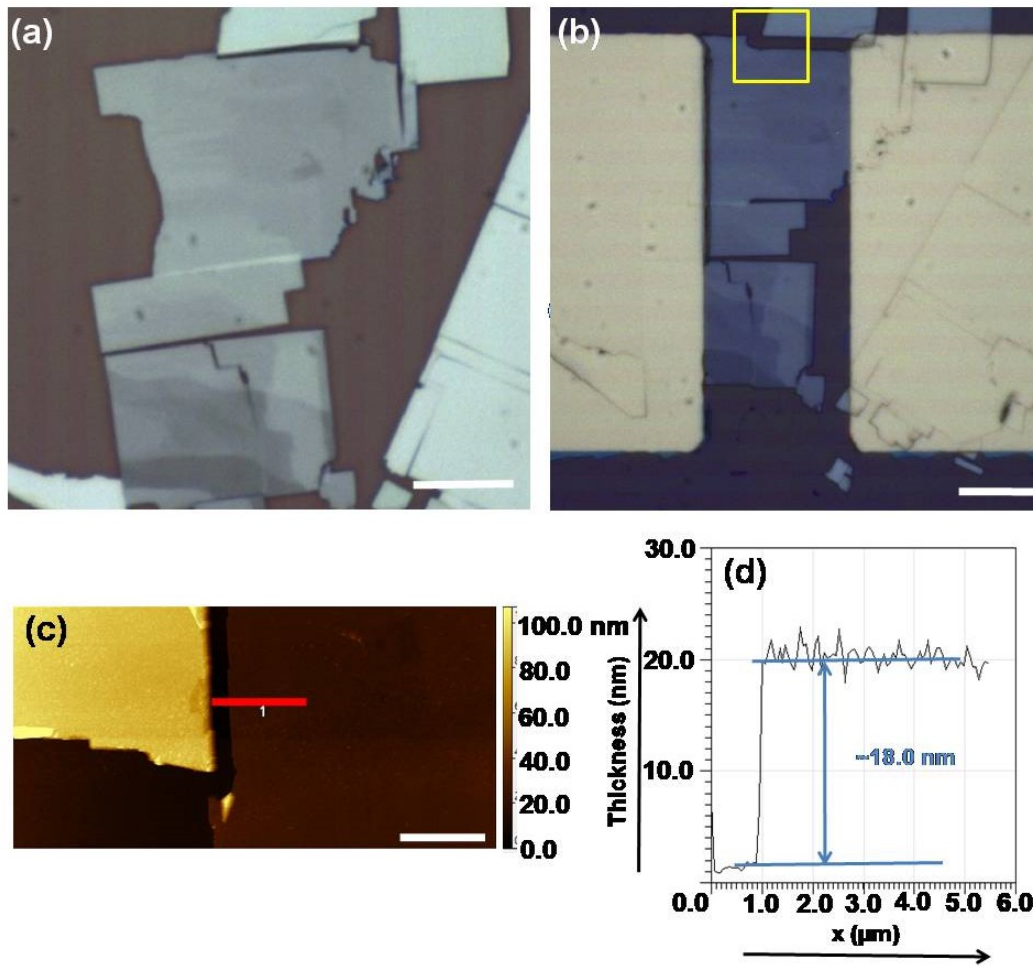


Figure 6-4. Fabrication procedure for the type 3 device with Ti/Au as top contacts (a) As-exfoliated PdSe₂ flakes on an oxygen plasma treated 285 nm SiO₂/Si substrate (b) Completed device with Ti/Au as top contacts to the PdSe₂ channel by a standard photolithography and metal lift-off procedure. (c) AFM height mapping of the PdSe₂ flake, highlighted by the yellow-boxed region in Fig. 6-4b. (d) Line profile taken across the red line in Fig. 6-4c. Scale bars are 10 μm in panels a-b, and 5 μm in panel c.

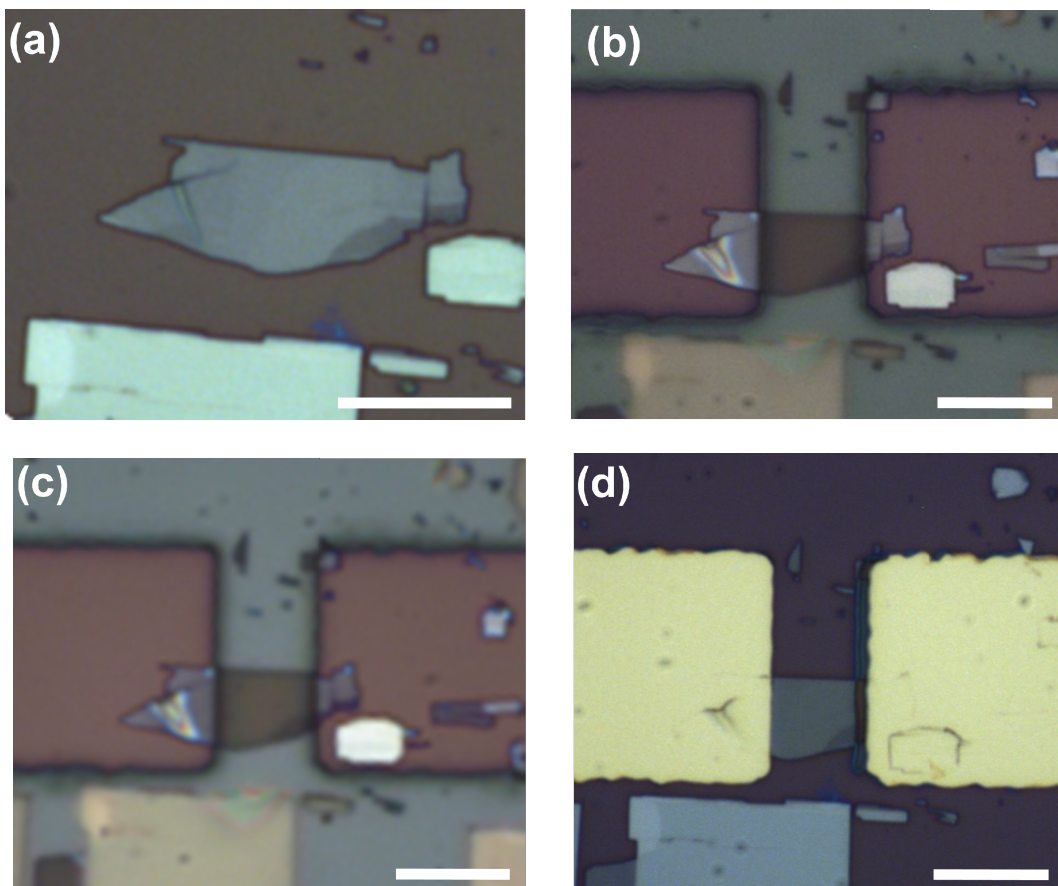


Figure 6-5. Fabrication procedure for the type 4 device. (a) As-exfoliated PdSe₂ flakes on an oxygen plasma treated 285 nm SiO₂/Si substrate. (b) The photoresist used as a mask to define contact regions on the PdSe₂ channel. (c) The contact regions of PdSe₂ after cleaning with an oxygen plasma, and an Ar⁺ ion bombardment treatment. (d) Final device with Ti/Au as top contacts to the bombarded PdSe₂ region. Scale bars are 10 μm in panels a-d.

behavior of PdSe₂ FET devices from ambipolar to n-type conduction.⁷ To understand the effect of annealing, all the four type of devices in this study were annealed for 2 hrs at 180°C under the constant flow of N₂ in a glovebox, and the device measurements were taken before and after annealing, in the air.

Next, we show the output characteristics of all the four devices. Figs. 6-6a and 6-6b show the output characteristics of the as-fabricated type 1 device depicting an electron dominant conduction. The linearity of the output curves in Figs 6-6a and 6-6b indicates that the device characteristics are not contact-limited.^{24,25,26,27} After annealing, the output curves remain linear, while the hole-conduction is suppressed and the electron-conduction is enhanced further, as shown by the Figs. 6-6c and 6-6d, respectively and will be discussed later in the transfer characteristics.

The output characteristics of the as-fabricated type 2 device are shown in Figs. 6-7a and 6-7b, indicating a suppression of the n-type conduction, compared to the type 1 device. This behavior is attributed to the surface contamination introduced by the dummy photolithography step, and PC processing during the device fabrication, as mentioned earlier. The linearity of the output curves in Figs 6-7a and 6-7b confirms that FLG-contacts can inject holes into p-doped PdSe₂ channel as well, and the observed dominant n-type conduction behavior of the as-fabricated type 1 device is due to the *intrinsic* n-doping of the PdSe₂ channel, and not an *extrinsic* effect caused by the possible favorable electron-injection of the FLG-contacts into the PdSe₂ channel. After annealing, the output curves of type 2 device remain linear, while the device behavior become nearly symmetric ambipolar, as depicted by Figs. 6-7c and 6-7d, respectively. This behavior will be discussed later in the transfer characteristics.

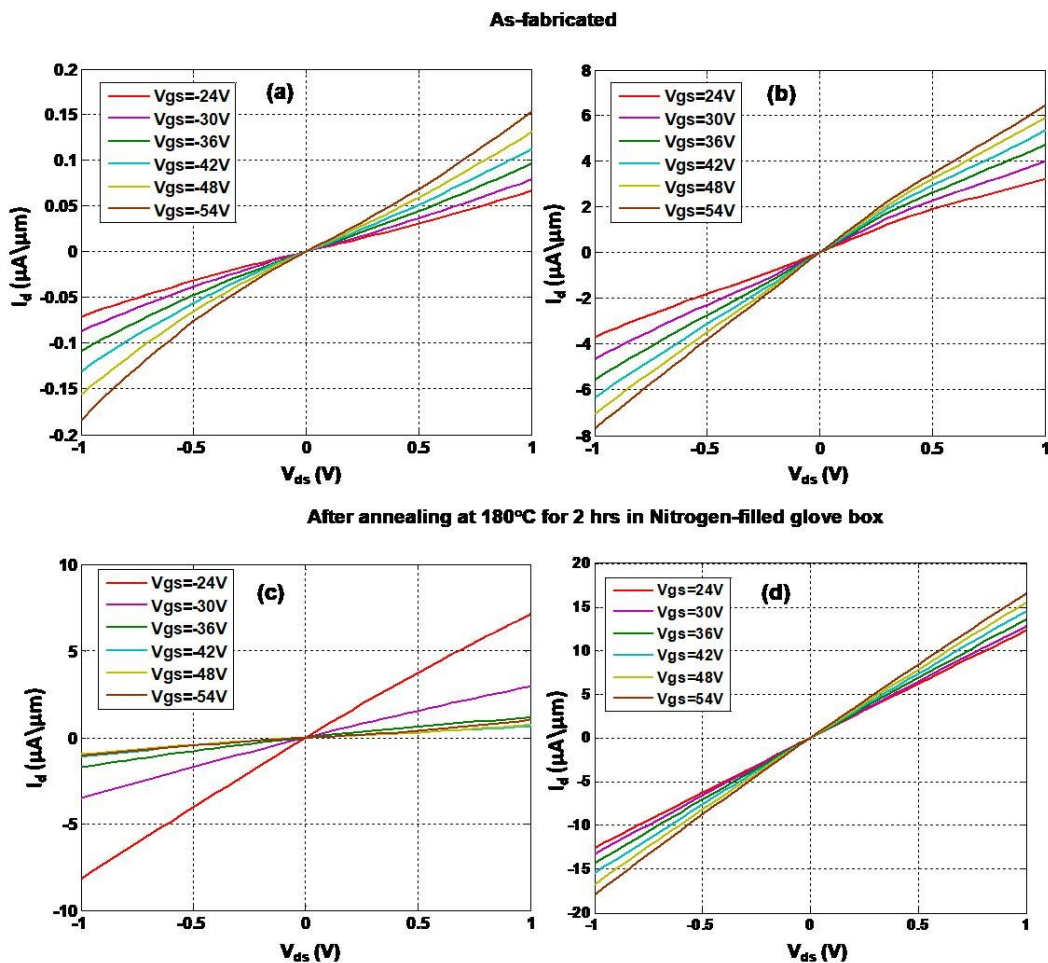


Figure 6-6. Output characteristics of fully encapsulated type 1 device. (a,b) Linear output curves showing that the device behavior is not limited by the contacts, while the electron-conduction behavior is dominant. (c,d) Output curves remain linear after annealing, while the hole-conduction is suppressed, and the electron-conduction is enhanced.

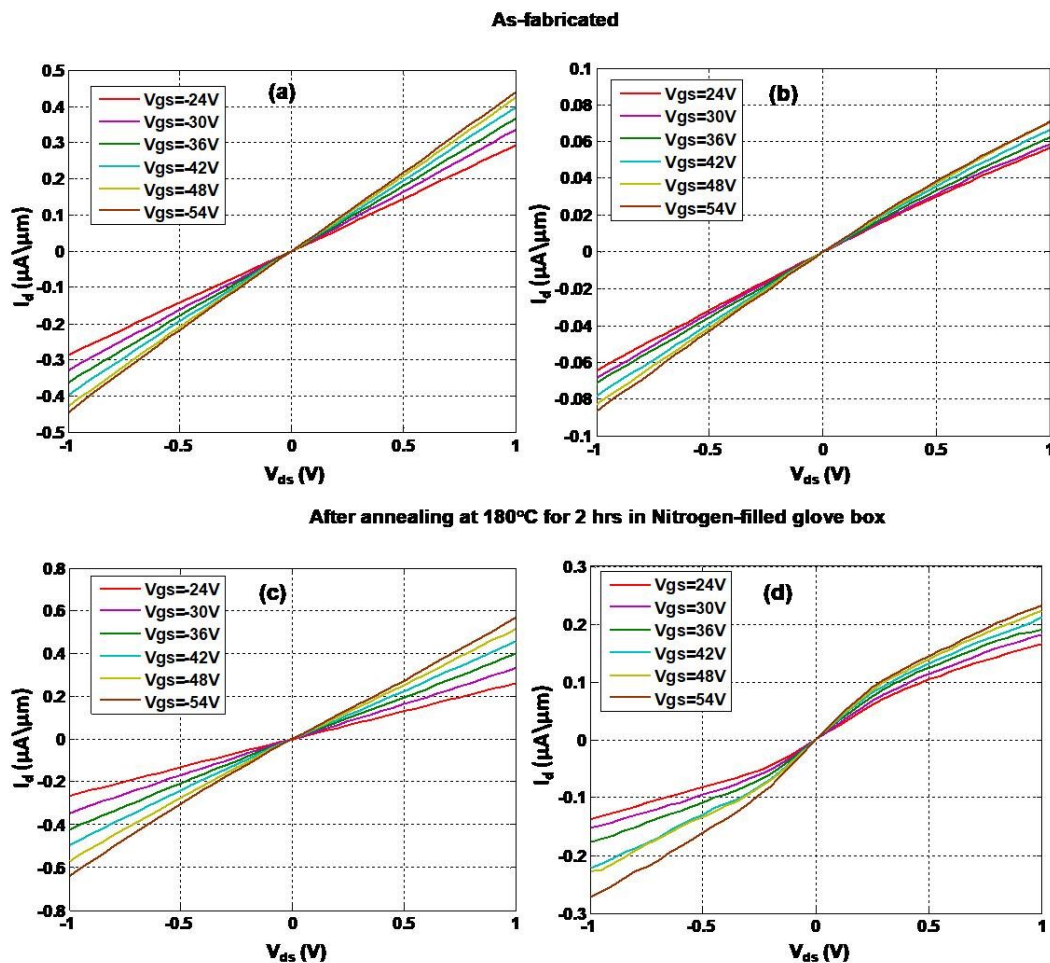


Figure 6-7. Output characteristics of type 2 device. (a,b) Hole-dominant conduction with linear output curves indicates that FLG-contacts can inject holes into the p-doped PdSe₂ channel as well (c,d) Output curves remain linear after annealing, while the overall device behavior becomes more ambipolar.

Figs. 6-8a and 6-8b show the output characteristics of the as-fabricated nearly symmetric ambipolar conduction. The output curves for both hole and electron conduction show Schottky-like behavior,^{25,27} which is more pronounced in the case of electron conduction. Figs. 6-8c and 6-8d show that the output curves for both hole and electron-conduction become linear at low- V_{ds} , after low-temperature annealing, indicating an improvement in the contact resistance between Ti and PdSe₂, while the electron-conduction is enhanced markedly. This enhancement in the electron-conduction of type 3 device after glove box annealing is very similar to the device behavior reported by Chow *et al.*, after low-temperature vacuum annealing.⁷ It is worth mentioning here that the hole-conduction in type 3 device is not suppressed after glove box annealing, unlike the results reported by Chow *et al.*⁷ The possible reason will be discussed in the context of transfer characteristics, to be presented later.

The output characteristics of the as-fabricated type 4 device are shown in Figs. 6-9a and 6-9b. The device behavior clearly shows an electron-dominant conduction. The reason for this enhancement in the n-type conduction will be presented later in the context of transfer characteristics. After annealing, the output curves for the electron-conduction become more linear even for higher V_{ds} , along with a further enhancement in the electron-conduction, as shown by Figs. 6-9c and 6-9d, respectively.

Next, we compare the transfer characteristics of all four types of devices before and after glove box annealing in Figs. 6-10a and 6-10b, respectively. The as-fabricated type 1 device clearly depicts an electron-dominant conduction as shown by the red curve in Fig. 6-10a with the maximum electron-conductivity of $\sim 29.5 \mu S/\square$ at $V_{gs} = 54V$, and the maximum hole-conductivity of $\sim 0.3 \mu S/\square$ at $V_{gs} = -54V$. The transfer characteristics of the as-fabricated type 2 device are shown by the purple curve in Fig. 6-10a, which depict a hole-dominant conduction,

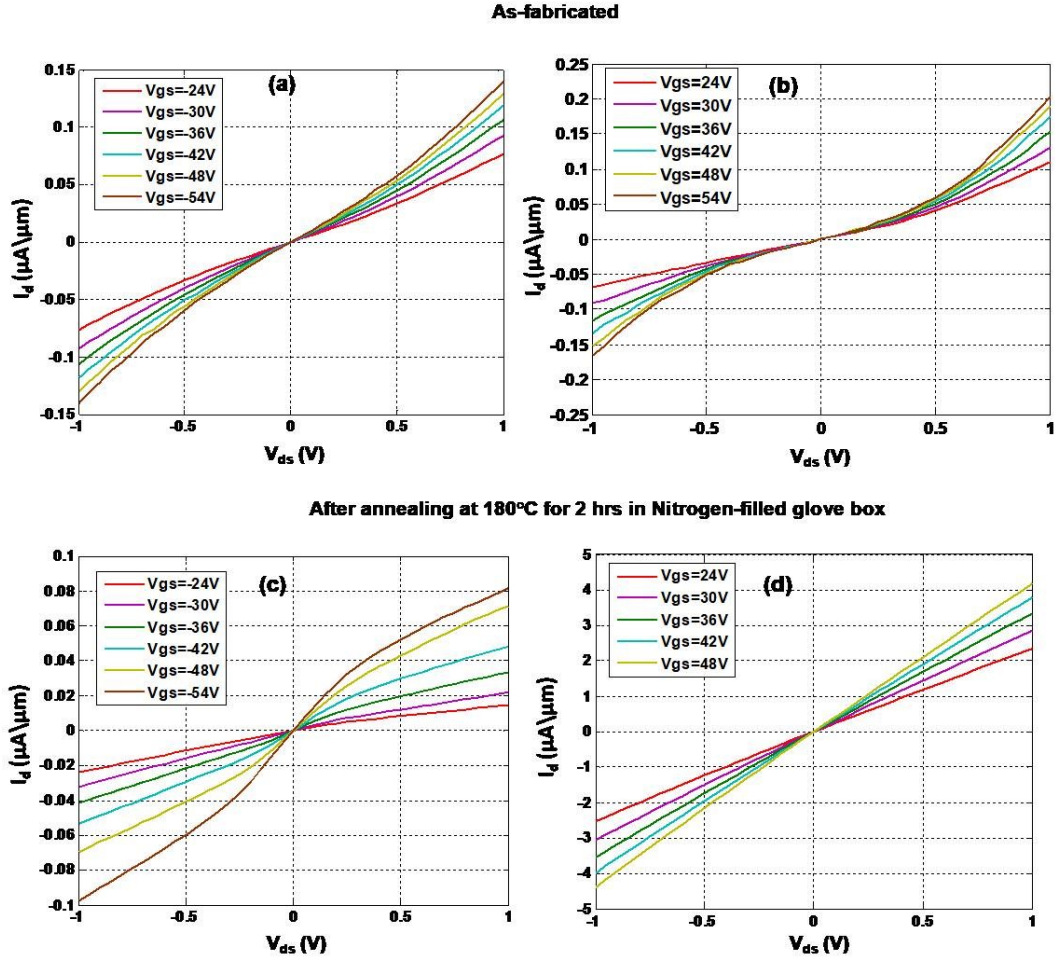


Figure 6-8. Output characteristics of type 3 device with Ti/Au as top contacts. (a,b) Both the hole and electron-conduction are Schottky-limited which is more pronounced for the later. (c,d) Output curves become linear for both hole and electron-conduction after annealing, while the overall device behavior becomes n-type.

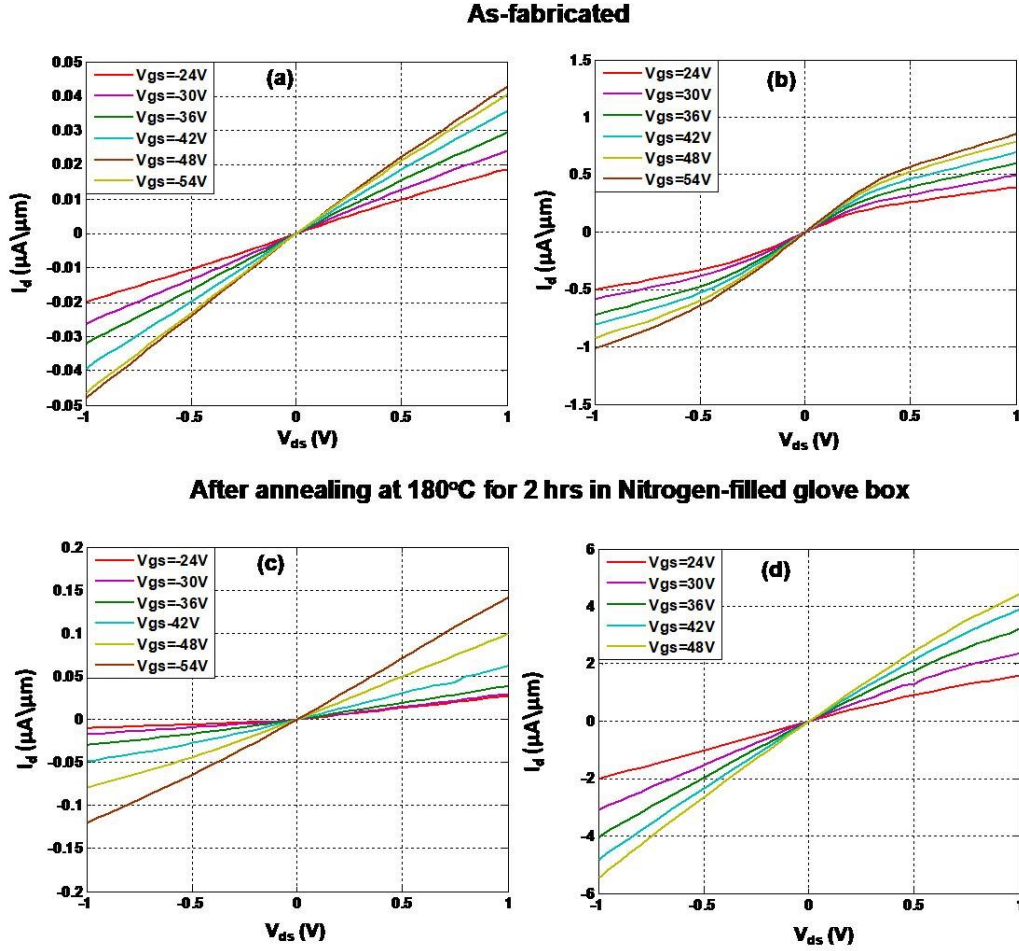


Figure 6-9. Output characteristics of type 4 device, where the contact regions between Ti and PdSe₂ are cleaned before metal deposition. (a,b) The output curves are linear for both hole and electron injection, while the n-type device behavior is dominant (c,d) After annealing, electron-conduction is enhanced further, along with a slight increase in hole-conduction as well.

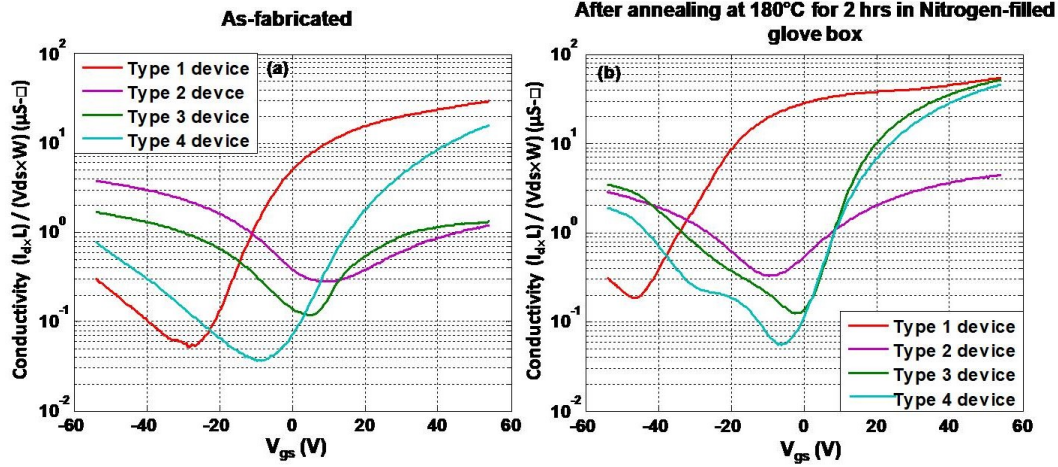


Figure 6-10. Transfer characteristics of the four type of devices before and after annealing at $V_{ds} = 0.1V$ (a) As-fabricated type 1 device show an electron-dominant conduction. Type 2 device show a hole-dominant conduction before annealing. As-fabricated type 3 device show nearly symmetric ambipolar conduction, while type 4 device shows an n-type behavior before annealing. (b) N-type behavior becomes more pronounced for type 1 device after annealing. Type 2 device shows a more symmetric ambipolar conduction after annealing. Both type 3 and type 4 devices exhibit a dominant n-type conduction behavior after annealing.

with the maximum hole-conductivity of $\sim 3.8 \mu\text{S}/\square$ at $V_{\text{gs}} = -54\text{V}$, and a maximum electron-conductivity of $\sim 1.2 \mu\text{S}/\square$ at $V_{\text{gs}} = 54\text{V}$. The electron-conductivity in the as-fabricated type 2 device is suppressed by a factor of ~ 24 , compared to the type 1 device, while the hole-conductivity is increased by a factor of ~ 13 . Although the PdSe_2 :FLG interface is intrinsic in both type of devices, but the main difference is in the channel region which is intrinsic in type 1 device and contaminated in type 2 device. A more than an order of magnitude increase in the hole-conductivity of type 2 device, compared to the type 1 device indicates that the FLG-contacts can inject holes into purposely contaminated PdSe_2 channel as well, and the observed n-type conduction of type 1 device is not due to the preferred electron-injection behavior of FLG-contacts into the PdSe_2 channel, rather later is the intrinsic behavior of few-layer PdSe_2 channel itself, most likely due to the presence of Se vacancies,¹⁹ and the ambipolar device behavior observed in the earlier reports was *extrinsic*.^{7,8} It is worth mentioning here that the slope of the hole-conduction in the type 1 device is more steep, compared to the results by Chow *et al.*⁷ The possible reason for this behavior will be presented later.

The transfer characteristics of the as-fabricated type 3 device show nearly symmetric ambipolar conduction, as indicated by the green curve in Fig. 6-10a. The maximum electron-conductivity of the as-fabricated type 3 device is $\sim 1.3 \mu\text{S}/\square$ at $V_{\text{gs}} = 54\text{V}$, while the maximum hole-conductivity is $1.7 \mu\text{S}/\square$ at $V_{\text{gs}} = -54\text{V}$. This device behaviour is consistent with ref. 7. The as-fabricated type 4 depicts an electron-dominant conduction as shown by the blue curve in Fig. 6-10a, with the maximum electron-conductivity of $\sim 16 \mu\text{S}/\square$ at $V_{\text{gs}} = 54\text{V}$, and a maximum hole-conductivity of $\sim 0.8 \mu\text{S}/\square$ at $V_{\text{gs}} = -54\text{V}$. The maximum hole-conductivity of type 4 device is suppressed by a factor ~ 2.1 compared to the maximum hole-conductivity of type 3 device, while the maximum electron-conductivity of type 4 device is increased by a factor of \sim

12.3 compared to the maximum electron-conductivity of type 3 device. Since the PdSe₂ channel region of both type 3 and 4 devices see the similar effect of photolithography processing, the observed difference in the device behavior is due to the Ti: PdSe₂, which is different in both type of devices. Since Ar⁺ ion bombardment is known to change the electronic properties of transition metal dichalcogenides,¹⁹ and given that the maximum hole-conductivity of type 4 device is suppressed compared to the type 3 device leads to the conclusion that the observed dominant n-type conduction of type 4 device is due to the preferred electron injection behavior of the Ti and Ar⁺ ion bombarded PdSe₂ interface.

The red curve in Fig. 6-10b shows the transfer characteristics of type 1 device after glove box annealing. The maximum electron-conductivity of the annealed device increased by a factor of 1.7, compared to the as-fabricated state, reaching a value of $\sim 52 \mu\text{S}/\square$ at $V_{\text{gs}} = 54\text{V}$, while the maximum hole-conductivity remains at the same value of $\sim 0.3 \mu\text{S}/\square$ $V_{\text{gs}} = -54\text{V}$. Comparing the transfer characteristics of the type 1 device before and after annealing reveals that the entire transfer characteristics are shifted to the left after annealing, but the slope of the hole-conduction remains the same. We attribute this finite hole conduction to be the intrinsic nature of the PdSe₂ flakes used in this study, possibly due to differences in the synthesis method for the bulk PdSe₂ crystals, compared to bulk crystals synthesized in ref. 7.

From the purple curve in Fig. 6-10b, the maximum electron-conductivity of type 2 device after annealing is increased by a factor of 3.6, compared to the as-fabricated state, reaching a value of $\sim 4.4 \mu\text{S}/\square$ at $V_{\text{gs}} = 54\text{V}$, while the maximum hole-conductivity is decreased by a factor of 1.3 reaching a value of $\sim 2.9 \mu\text{S}/\square$ $V_{\text{gs}} = -54\text{V}$. For type 1 device, the improvement in the electron-conduction after annealing is attributed to an improved van der Waals contact²⁸ between PdSe₂ and FLG, while for type 2 device, the enhancement in the electron-conduction, and the

simultaneous suppression of the hole-conduction is associated with the combined effect of improved van der Waals contact between PdSe₂ and FLG, and the reduction in the p-doping of the channel due to the surface contamination introduced on channel intentionally during device fabrication. The latter conjecture is plausible because surface contamination would be mobile at the annealing temperature of 180°C.²⁹ Since type 2 device was encapsulated by a top h-BN cover just like type 1 device, the effect of intentional channel doping could not be reverted completely, after annealing the device at low temperature for 2 hrs only.

Type 3 device after annealing shows a marked increase in the electron-conduction by a factor of ~ 40 , compared to the as-fabricated state, reaching a maximum value of $\sim 52 \mu\text{S}/\square$ at $V_{\text{gs}} = 54\text{V}$ as shown by the green curve in Fig. 6-10b. This behavior is consistent with the result reported by Chow *et al.*⁷ The maximum hole-conductivity is nearly doubled after annealing, reaching a value of $\sim 3.5 \mu\text{S}/\square$ at $V_{\text{gs}} = -54\text{V}$. This trend is opposite to the result reported by Chow *et al.*, who found that after vacuum annealing, the hole-conduction was actually suppressed by a factor of ~ 7 compared to the as-fabricated device.⁷ Comparing the transfer characteristics for type 1 and 3 devices after annealing reveals that they have nearly identical slopes for the hole-conduction, which is attributed to the intrinsic nature of the PdSe₂ flakes used in this study, as mentioned earlier, but the point of minimum conductivity for type 1 device is shifted towards large negative gate voltage, while for the type 3 device the point of minimum conductivity is centered around $V_{\text{g}}=0$, that is why hole-conduction is apparently higher for type 3 devices compared to the type 1 device. Since the type 3 device has seen the photolithography process, it may leave some residues on the PdSe₂ flakes which cannot be removed by low-temperature glove-box annealing. This conjecture is further corroborated by the fact while the ON/OFF ratios of type 1 and type 3 devices after annealing are nearly identical, but the thickness

of the PdSe₂ flake in type 3 device, as measured by AFM was higher compared to the thickness of PdSe₂ flake in type 1 device. While the point of minimum conductivity for fully-encapsulated type 1 device is located at large negative V_{gs} , which is typical for n-type conduction, but due to the presence of photolithography residues on the PdSe₂ flake in type 3 device, which acts as a weak p-dopant, the point of minimum conductivity is located at $\sim V_{gs} = 0V$ for type 3 device. The improvement in the maximum hole-conductivity for type 3 device after annealing, is due to the improvement in the contact resistance, but since the hole-conduction is weaker compared to the electron-conduction, that is why the improvement in hole-conductivity is smaller compared to the improvement in the electron-conductivity.

Type 4 device after annealing shows a further increase in the electron-conduction by a factor of ~ 2.8 reaching a maximum value of $\sim 45.7 \mu S/\square$ at $V_{gs} = 54V$, as shown by the blue curve in Fig. 5-10b. The hole-conduction, on the other hand, is increased by a factor of ~ 2.4 as well after annealing reaching a maximum value of $\sim 1.9 \mu S/\square$ at $V_{gs} = -54V$. This finite hole-conduction of type 4 device after annealing is consistent with the device behavior of type 3 device and is attributed to the intrinsic behavior of PdSe₂ flakes used in this study, as mentioned earlier.

Table 6-1 summarizes the behavior of all four type of devices before and after annealing, based on the transfer characteristics discussed above. As-fabricated type 1 device shows an electron-dominant conduction, due to the intrinsic n-doping of the PdSe₂ channel, which was preserved during device fabrication. This was confirmed by the behavior of the as-fabricated type 2 device, which like type 1 device also had FLG as bottom-contacts, but showed a pronounced hole-conduction due to the intentional contamination introduced on the PdSe₂ channel during the device fabrication, which led to the p-doping of the later. After annealing,

both type 1 and 2 devices show an improvement in the electron-conduction due to the improved van der Waals contact between PdSe₂ and FLG. Additionally, hole conduction in type 2 device was slightly suppressed after annealing that also accounted for the partial recovery of the intrinsic electron- conduction of the PdSe₂ channel. As-fabricated type 3 shows nearly symmetric ambipolar behavior, due to the contact limited electron-injection, which is overcome by the glove box annealing, leading to a pronounced n-type behavior. Type 4 device before annealing shows an electron-dominant conduction due to the preferred electron injection behavior of Ti: Ar⁺ ion bombarded PdSe₂ interface. This electron-dominant conduction behavior was enhanced further after low-temperature annealing, due to a reduced contact resistance of Ti: Ar⁺ ion bombarded PdSe₂ interface. Both type 3 and 4 devices, shows a finite hole-conduction after annealing, and this behavior is attributed to the intrinsic nature of the PdSe₂ flakes used in this study.

The field-effect mobilities are extracted from the linear region of the transfer characteristics using the equation: $\mu = \frac{dI_d}{dV_{gs}} \times \frac{L}{W} \times \frac{1}{C_{ox}} \times \frac{1}{V_{ds}}$ ²⁵ and are also listed in table 6-1, where $C_{ox} = \frac{\epsilon_0 \epsilon_r}{d}$ is the gate-oxide capacitance per unit area, and $d = 285$ nm is the thickness of the SiO₂ gate oxide. As-fabricated type 1 device shows a high electron mobility of ~ 43 cm²/Vsec, which increases further to ~ 85.0 cm²/Vsec after annealing, due to an improved van der Waals contact between PdSe₂ and FLG, as mentioned earlier. Type 2 device shows an improvement in the electron-mobility by a factor of ~ 3.5 after annealing, due to an improved van der Waals contact, and a partial decrease in the p-doping of the channel. The hole mobility is only slightly decreased after annealing, as the later was insufficient to completely eliminate the effect of the intentional p-doping of the PdSe₂ channel. Type 3 device shows a marked increase in the electron mobility after annealing, which is attributed to the reduction in the contact

Table 6-1. Summary of the device characteristics.

| Before Annealing | | | | After Annealing | | |
|------------------|--|-----------------------------------|-------------------------------|--|-----------------------------------|-------------------------------|
| Type of device | Ratio of electron-to-hole conductivity at $V_{gs} = \pm 54V$ | Electron mobility ($cm^2/Vsec$) | Hole mobility ($cm^2/Vsec$) | Ratio of electron-to-hole conductivity at $V_{gs} = \pm 54V$ | Electron mobility ($cm^2/Vsec$) | Hole mobility ($cm^2/Vsec$) |
| Type 1 | ~ 98.3 | ~ 43.0 | - | ~ 173.3 | ~ 85.0 | - |
| Type 2 | ~ 0.3 | ~ 2.0 | ~ 5.6 | ~ 1.5 | ~ 7.0 | ~ 5.5 |
| Type 3 | ~ 0.8 | ~ 3.0 | ~ 2.6 | ~ 14.8 | ~ 115.0 | - |
| Type 4 | ~ 20.3 | ~ 40.1 | - | ~ 24.1 | ~ 100.1 | ~ 5.5 |

resistance of Ti:PdSe₂ interface. Type 4 device had a higher electron-mobility compared to type 3 device in the as-fabricated state. After annealing, electron-mobility of type 4 device enhanced further due to the reduction of Ti:Ar⁺ ion bombarded PdSe₂ interface resistance after annealing.

6.4 Conclusion

In summary, we have untangled the effect of channel behavior and the effect of contacts to show that PdSe₂-based FET has an intrinsic n-type conduction. When the PdSe₂ channel and PdSe₂:contact interface do not see the effect of any extrinsic contamination during device processing, the as-fabricated and fully-encapsulated PdSe₂ device shows dominant n-type conduction. Comparison with a control device in which channel is purposely contaminated while keeping the channel:contact interface intrinsic reveals that the observed dominant n-type conduction of the fully-encapsulated device is not due to the preferred electron-injection behavior of the contacts rather it is the intrinsic behavior of the channel itself. Further it is revealed that by engineering the metal and PdSe₂ interface, it is possible to shift the device behavior from ambipolar to n-type, without changing the intrinsic behavior of the PdSe₂ channel.

6.5 Experimental methods

6.5.1 FET device fabrication and characterization

Before the exfoliation of 2D flakes, the 285 nm SiO₂/Si substrates used in this study were cleaned with acetone and isopropanol, followed by an oxygen plasma cleaning step. For transferring 2D flakes from one substrate to another, PDMS/PC stack attached to a glass-slide was used as a stamp.¹⁷ The entire flake-transfer procedure was carried out by using a custom-made aligned transfer setup.³⁰ To make PC stamps, an 8% w/w solution of PC in chloroform was spin-coated on a dummy oxygen plasma cleaned SiO₂/Si substrates at 4000 rpm for 60 sec. The

PC film was further dried by heating at 150°C¹⁷ for 10 minutes. After this step, a PC stamp in the form of the small piece can be lifted-off the SiO₂/Si substrates to be further attached to a PDMS stamp on a glass slide. For picking up a 2D flake, a PDMS/PC stack was brought in contact with a target flake held around 145°C. When the temperature cools down to 90°C, the flake is picked up by the PDMS/PC stamp. For landing a 2D flake onto a target substrate, the PDMS/PC/flake stack was pressed onto a target substrate, and the later was quickly heated to melt the PC film around 145°C, while the PDMS stamp was lifted up. This procedure leaves the PC/flake stack on the desired substrate. Finally, to improve the adhesion of 2D flake on the target substrate, the later was heated at 150°C for 10 min. After cooling down, the PC film was first dissolved in N-Methyl-2-pyrrolidone (NMP) for 30 min. and then in chloroform for another 30 min. Finally, the substrates were rinsed with isopropanol and dried with N₂. FET devices were fabricated with standard photolithography process using S1813 as a photoresist. The electrical contacts for probing were made with the electron-beam deposition of 15 nm thick Ti, and 50 nm thick Au. All the devices were tested in air using Keithley 4200 parameter analyzer. Type 4 device in this study with photoresist as a mask was exposed to 5 min. of oxygen plasma at 200 mTorr, followed by 15 min. of Argon plasma at 1Torr, before metal deposition. The RF power for both the processes was 30W.

6.6 References

- (1) Geim, A.K. Novoselov, K.S. The rise of graphene. *Nat. Mater.* **2007**, 6, 183–191.
- (2) Schwierz, F. Graphene Transistors. *Nat. Nanotech.* **2010**, 5, 487–496.
- (3) Radisavljevic, B.; Radenovic, A.; Brivio, J.; Giacometti, V.; Kis, A. Single-Layer MoS₂ transistors. *Nat. Nanotech.* **2011**, 6, 147–150.
- (4) Wang, Q. H.; Kalantar-Zadeh, K.; Kis, A.; Coleman, J. N.; Strano, M. S. Electronics and Optoelectronics of Two-Dimensional Transition Metal Dichalcogenides. *Nat. Nanotech.* **2012**, 7, 699–712.
- (5) Gong, C.; Zhang, H.; Wang, W.; Colombo, L.; Wallace, R. M.; Cho, K. Band Alignment of Two-Dimensional Transition Metal Dichalcogenides: Application in Tunnel Field Effect Transistors. *Appl. Phys. Lett.* **2013**, 103, 053513.
- (6) Liu, X.; Zhou, H.; Yang, B.; Qu, Y.; Zhao, M. Strain-Modulated Electronic Structure and Infrared Light Adsorption in Palladium Diselenide Monolayer. *Sci. Rep.* **2017**, 7, 3–8.
- (7) Chow, W. L.; Yu, P.; Liu, F.; Hong, J.; Wang, X.; Zeng, Q.; Hsu, C. H.; Zhu, C.; Zhou, J.; Wang, X.; *et al.* High Mobility 2D Palladium Diselenide Field-Effect Transistors with Tunable Ambipolar Characteristics. *Adv. Mater.* **2017**, 29, 1–8.
- (8) Oyedele, A. D.; Yang, S.; Liang, L.; Puretzky, A. A.; Wang, K.; Zhang, J.; Yu, P.; Pudasaini, P. R.; Ghosh, A. W.; Liu, Z.; *et al.* PdSe₂: Pentagonal Two-Dimensional Layers with High Air Stability for Electronics. *J. Am. Chem. Soc.* **2017**, 139, 14090–14097.

- (9) Zhang, Y.; Chang, T. R.; Zhou, B.; Cui, Y. T.; Yan, H.; Liu, Z.; Schmitt, F.; Lee, J.; Moore, R.; Chen, Y.; *et al.* Direct Observation of the Transition from Indirect to Direct Bandgap in Atomically Thin Epitaxial MoSe₂. *Nat. Nanotech.* **2014**, *9*, 111–115
- (10) Sun, J.; Shi, H.; Siegrist, T.; Singh, D. J. Electronic, Transport, and Optical Properties of Bulk and Mono-Layer PdSe₂. *Appl. Phys. Lett.* **2015**, *107*, 2–6.
- (11) Liu, W.; Kang, J.; Sarkar, D.; Khatami, Y.; Jena, D.; Banerjee, K. Role of Metal Contacts in Designing High-Performance Monolayer N-Type WSe₂ field Effect Transistors. *Nano Lett.* **2013**, *13*, 1983–1990.
- (12) Qiu, H.; Pan, L.; Yao, Z.; Li, J.; Shi, Y.; Wang, X. Electrical Characterization of Back-Gated Bi-Layer MoS₂ Field-Effect Transistors and the Effect of Ambient on Their Performances. *Appl. Phys. Lett.* **2012**, *100*, 123104.
- (13) Wang, L.; Meric, I.; Huang, P. Y.; Gao, Q.; Gao, Y.; Tran, H.; Taniguchi, T.; Watanabe, K.; Campos, L. M.; Muller, D. A.; *et al.* One-Dimensional Electrical Contact to a Two-Dimensional Material. *Science* **2013**, *342*, 614–617.
- (14) Cui, X.; Lee, G.-H.; Kim, Y. D.; Arefe, G.; Huang, P. Y.; Lee, C.-H.; Chenet, D. A.; Zhang, X.; Wang, L.; Ye, F.; *et al.* Multi-Terminal Transport Measurements of MoS₂ Using a van Der Waals Heterostructure Device Platform. *Nat. Nanotech.* **2015**, *10*, 534–540.
- (15) Das, S.; Chen, H.-Y.; Penumatcha, A. V.; Appenzeller, J. High Performance Multilayer MoS₂ Transistors with Scandium Contacts. **2013**, *13*, 100–105.
- (16) Liu, Y.; Stradins, P.; Wei, S. Van Der Waals Metal – Semiconductor Junction : Weak

Fermi Level Pinning Enables Effective Tuning of Schottky Barrier. *Sci. Adv.* **2016**, *2*, e1600069.

(17) Zomer, P. J.; Guimares, M. H. D.; Brant, J. C.; Tombros, N.; Van Wees, B. J. Fast Pick up Technique for High Quality Heterostructures of Bilayer Graphene and Hexagonal Boron Nitride. *Appl. Phys. Lett.* **2014**, *105*.

(18) Plummer, J.D.; Deal, M.; Griffin, P.D. *Silicon VLSI Technology Fundamentals, Practice, and Modeling*. Prentice Hall-New Jersey, 2000.

(19) Kim, D.; Du, H.; Kim, T.; Shin, S.; Kim, S.; Song, M.; Lee, C.; Lee, J.; Cheong, H.; Seo, D. H.; *et al.* The Enhanced Low Resistance Contacts and Boosted Mobility in Two-Dimensional P-Type WSe₂ transistors through Ar⁺ion-Beam Generated Surface Defects. *AIP Adv.* **2016**, *6*, 49966049.

(20) Huang, Y.; Sutter, E.; Shi, N. N.; Zheng, J.; Yang, T.; Englund, D.; Gao, H. J.; Sutter, P. Reliable Exfoliation of Large-Area High-Quality Flakes of Graphene and Other Two-Dimensional Materials. *ACS Nano* **2015**, *9*, 10612–10620.

(21) Haigh, S. J.; Gholinia, A.; Jalil, R.; Romani, S.; Britnell, L.; Elias, D. C.; Novoselov, K. S.; Ponomarenko, L. A.; Geim, A. K.; Gorbachev, R. Cross-Sectional Imaging of Individual Layers and Buried Interfaces of Graphene-Based Heterostructures and Superlattices. *Nat. Mater.* **2012**, *11*, 764–767.

(22) Private communication.

(23) Durkan, C.; Xiao, Z. On the Failure of Graphene Devices by Joule Heating under Current Stressing Conditions. *Appl. Phys. Lett.* **2015**, *107*, 4936993

- (24) Fang, H.; Chuang, S.; Chang, T. C.; Takei, K.; Takahashi, T.; Javey, A. High-Performance Single Layered WSe₂ P-FETs with Chemically Doped Contacts. *Nano Letters* **2012**, *12*, 3788–3792.
- (25) Liu, W.; Kang, J.; Sarkar, D.; Khatami, Y.; Jena, D.; Banerjee, K. Role of Metal Contacts in Designing High-Performance Monolayer N-Type WSe₂ field Effect Transistors. *Nano Letters* **2013**, *13*, 1983–1990.
- (26) Yu, L.; Lee, Y. H.; Ling, X.; Santos, E. J. G.; Shin, Y. C.; Lin, Y.; Dubey, M.; Kaxiras, E.; Kong, J.; Wang, H.; *et al.* Graphene/MoS₂ Hybrid Technology for Large-Scale Two-Dimensional Electronics. *Nano Letters* **2014**, *14*, 3055–3063.
- (27) Roy, T.; Tosun, M.; Kang, J. S.; Sachid, A. B.; Desai, S. B.; Hettick, M.; Hu, C. C.; Javey, A. Field-Effect Transistors Built from All Two-Dimensional Material Components. *ACS Nano* **2014**, *8*, 6259–6264.
- (28) Chiu, M. H.; Li, M. Y.; Zhang, W.; Hsu, W. T.; Chang, W. H.; Terrones, M.; Terrones, H.; Li, L. J. Spectroscopic Signatures for Interlayer Coupling in MoS₂-WSe₂ van Der Waals Stacking. *ACS Nano* **2014**, *8*, 9649–9656.
- (29) Pizzocchero, F.; Gammelgaard, L.; Jessen, B. S.; Caridad, J. M.; Wang, L.; Hone, J.; Bøggild, P.; Booth, T. J. The Hot Pick-up Technique for Batch Assembly of van Der Waals Heterostructures. *Nat. Commun.* **2016**, *7*, 11894.

- (30) Castellanos-Gomez, A.; Buscema, M.; Molenaar, R.; Singh, V.; Janssen, L.; van der Zant, H.S.J.; Steele, G.A. Deterministic transfer of two-dimensional materials by all-dry viscoelastic stamping. *2D Mater.* **2014**, *1*, 011002.

CHAPTER 7

SUMMARY AND FUTURE WORK

7.1 Summary

Following are the original contributions of this thesis to the emerging field of 2D materials:

- 1) A facile APCVD based method for graphene growth is presented that involves melting and re-solidification of copper on tungsten foil before the graphene growth process. This pre-treatment results in a smooth copper surface that enables the growth of mm-sized graphene single crystals. Characterizations by SAED in TEM and Raman spectroscopy revealed that the synthesized graphene crystals are monolayer thick, and single crystalline.
- 2) A STEM-based scheme is presented in this thesis to experimentally determine the edge orientations of CVD-grown triangular crystals of h-BN on Cu,¹ for the first time. The edge-orientation turned out to be zigzag-oriented and N-terminated, as predicted by the theory.² The demonstrated method consists of determining a macroscopic edge direction of an edge obtained from an overview STEM image of a 2D crystal, combined with the lattice orientation information determined from the atomic resolution STEM image acquired in 2D bulk, to deduce the macroscopic edge orientation. This scheme is general and is applicable to other 2D materials that lack mirror-symmetry e.g. transition metal dichalcogenides.
- 3) Two electron microscopy based corroborating techniques have been developed in this thesis to map out the layer count of CVD grown few-layer h-BN films at a much higher spatial resolution, compared to the state-of-the-art techniques known in the literature. The first method that involves STEM-HAADF imaging is based on mass-thickness contrast which is normalized to the intensity of monolayer h-BN to determine the layer count. This method although having a very higher spatial resolution of 0.25 nm, however, is insensitive to the carbon contamination introduced on a 2D film during transfer. Hence, layer count by STEM-HAADF imaging can only

be determined reliably in the atomically clean regions. To overcome this limitation, the boron K-edge in the EELS spectrum of h-BN has been used as a marker to detect h-BN even in the presence of organic contamination. The overall density of boron atoms in a given pixel is determined from the EELS spectrum of h-BN, and by knowing the density of boron atoms in monolayer h-BN, layer count has been derived. The spatial resolution of this method is low i.e., 16 nm compared to STEM-HAADF imaging, hence the two techniques complement each other.

4) In this thesis, control field-effect transistor (FET) devices have been fabricated and measured out to show the recently synthesized and exfoliated palladium diselenide is an intrinsic n-type semiconductor. The as-fabricated h-BN encapsulated PdSe₂ FET with few-layer graphene (FLG) as bottom-contacts showed predominant electron-conduction. The as-fabricated control device with purposely p-doped PdSe₂ channel showed dominant hole-conduction, indicating that the observed n-type behavior of the fully encapsulated clean PdSe₂ device is not due to the favorable electron-injection of FLG-contacts, rather it is the intrinsic behavior of the PdSe₂ channel. Un-encapsulated PdSe₂ devices with Ti/Au-top contacts showed nearly symmetric ambipolar conduction, consistent with the earlier studies. When the contact region between Ti and PdSe₂ was cleaned by successive oxygen plasma and Ar⁺ ion bombardment before metal deposition during device fabrication, the as-fabricated PdSe₂ FET showed n-type behavior indicating that the observed ambipolar behavior of the as-fabricated Ti/Au-top contacted PdSe₂ FET was due to the contact-limited electron-injection.

7.2 Future work

Based on the research carried out in this thesis, following further studies are recommended.

1) Graphene crystals grow on resolidified copper in this study nucleate at random locations.

From FET device processing point of view, crystals grown in a periodic array would be more beneficial because in that case, the location of potential grain-boundaries can be known after the graphene growth, and such regions can be avoided for making useful devices. Yu *et al.* demonstrated such an array of CVD grown graphene crystals by using PMMA as seeds, but the size of graphene crystals was limited to ten microns only.³ This seeding-approach can be extended to grow an array of mm-sized graphene crystals. Also recently, dry transfer technique has been demonstrated to pick-up CVD grown graphene crystals on copper by exfoliated h-BN flakes as stamps.⁴ Also, this approach can be applied to an array of mm-sized graphene crystals mentioned earlier, such that a PMMA-capped high-quality CVD grown thin film of h-BN, can be first used to pick-up an array of mm-sized graphene crystals from resolidified copper surface. Then, this stack of PMMA/h-BN/graphene can be transferred to another thin film of CVD grown h-BN on Ni to create a PMMA/h-BN/graphene/h-BN/Ni stack. The bottom Ni can be etched away, and the top PMMA can be removed in a solvent. Finally, the FET devices can be made by making 1D-contacts to graphene.⁵

2) Recently h-BN crystals with shapes other than the commonly observed triangles have been synthesized.⁶ The developed method in this thesis can be systematically applied to study the edge orientation of those crystals.^{7,8,9} Also, the recent theoretical study suggested that triangular crystals of h-BN grown on Ni catalyst will have zigzag oriented and B-terminated edges.¹⁰ The method developed in this thesis can be used to experimentally verify this conjecture.

3) The two electron microscopy-based methods developed in this thesis revealed that the CVD grown film of few-layer h-BN on copper was highly non-uniform in terms of layer count. Recently single crystal Ni (111) has been demonstrated to grow large area spatially uniform two-layer thick film of h-BN.¹¹ The two methods developed here will be used to characterize and

optimize the CVD growth of spatially uniform 6-9 layer of h-BN on Ni (111), for tunnel-dielectric applications.¹²

4) During the course of FET device fabrication based on few-layer PdSe₂, it was observed that gentle Ar⁺ ion plasma can change the electrical conductivity of intrinsic PdSe₂ by three orders of magnitude. By using this highly conductive phase of PdSe₂ as source-drain contacts, a FET device with self-aligned gates needs can be demonstrated.¹³ Also, this conducting phase needs to be studied by electron microscopy to understand the underlying for its conducting nature.

7.3 References

- (1) Kim, K. K.; Hsu, A.; Jia, X.; Kim, S. M.; Shi, Y.; Hofmann, M.; Nezich, D.; Rodriguez-Nieva, J. F.; Dresselhaus, M.; Palacios, T.; *et al.* Synthesis of Monolayer Boron Nitride on Cu Foil Using Chemical Vapor Deposition. *Nano Lett.* **2011**, *12*, 161-166.
- (2) Zhang, Z.; Liu, Y.; Yang, Y.; Yakobson, B. I. Growth Mechanism and Morphology of Hexagonal Boron Nitride. *Nano Lett.* **2016**, *16*, 1398–1403.
- (3) Yu, Q.; Jauregui, L. A.; Wu, W.; Colby, R.; Tian, J.; Su, Z.; Cao, H.; Liu, Z.; Pandey, D.; Wei, D. *et al.* Control and Characterization of Individual Grains and Grain Boundaries in Graphene Grown by Chemical Vapour Deposition. *Nat. Mater.* **2011**, *10*, 443–449.
- (4) Banszerus, L.; Schmitz, M.; Engels, S.; Dauber, J.; Oellers, M.; Gr, P. Ultra-High Mobility Graphene Devices from Chemical Vapor Deposition on Reusable Copper. *Science* **2015**, *1*, e1500222.
- (5) Wang, L.; Meric, I.; Huang, P. Y.; Gao, Q.; Gao, Y.; Tran, H.; Taniguchi, T.; Watanabe, K.; Campos, L. M.; Muller, D. A.; *et al.* One-Dimensional Electrical Contact to a Two-Dimensional Material. *Science* **2013**, *342*, 614-617.
- (6) Kim, K. K.; Hsu, A.; Jia, X.; Kim, S. M.; Shi, Y.; Hofmann, M.; Nezich, D.; Rodriguez-Nieva, J. F.; Dresselhaus, M.; Palacios, T.; *et al.* Synthesis of Monolayer Boron Nitride on Cu Foil Using Chemical Vapor Deposition. *Nano Lett.* **2011**, *12*, 161-166.
- (7) Tay, R. Y.; Griep, M. H.; Mallick, G.; Tsang, S. H.; Singh, R. S.; Tumlin, T.; Teo, E. H. T.; Karna, S. P. Growth of Large Single-Crystalline Two-Dimensional Boron Nitride Hexagons

on Electropolished Copper. *Nano Lett.* **2014**, *14*, 839–846.

(8) Stehle, Y.; Meyer, H. M.; Unocic, R. R.; Kidder, M.; Polizos, G.; Datskos, P. G.; Jackson, R.; Smirnov, S. N.; Vlassiouk, I. V. Synthesis of Hexagonal Boron Nitride Monolayer: Control of Nucleation and Crystal Morphology. *Chem. of Mater.* **2015**, *27*, 8041–8047.

(9) Tay, R. Y.; Park, H. J.; Ryu, G. H.; Tan, D.; Tsang, S. H.; Li, H.; Liu, W.; Teo, E. H. T.; Lee, Z.; Lifshitz, Y.; *et al.* Synthesis of Aligned Symmetrical Multifaceted Monolayer Hexagonal Boron Nitride Single Crystals on Resolidified Copper. *Nanoscale* **2016**, *8*, 2434–2444.

(10) Zhang, Z.; Liu, Y.; Yang, Y.; Yakobson, B. I. Growth Mechanism and Morphology of Hexagonal Boron Nitride. *Nano Lett.* **2016**, *16*, 1398–1403.

(11) Oh, H.; Jo, J.; Tchae, Y.; Yoon, H.; Hwi Lee, H.; Kim, S.-S.; Kim, M.; Sohn, B.-H.; Yi, G.-C. Centimeter-Sized Epitaxial H-BN Films. *NPG Asia Materials* **2016**, *8*, e330.

(12) Roy, T.; Liu, L.; Chakrabarti, B.; Hesabi, Z. R.; Joiner, C. A.; Feenstra, R. M.; Gu, G.; Vogel, E. M. Tunneling characteristics in chemical vapor deposited graphene–hexagonal boron nitride–graphene junctions. *Appl. Phys. Lett.* **2014**, *104*, 123506.

(13) Plummer, J.D.; Deal, M.; Griffin, P.D. Silicon VLSI Technology Fundamentals, Practice, and Modeling. Prentice Hall-New Jersey, 2000.

VITA

Mr. Ali Mohsin was born in Sargodha, a city of the Punjab Province in Pakistan. He earned his Bachelor's degree in electrical engineering, from the University of Engineering and Technology, Lahore in September 2008. Then he served as a lecturer/lab engineer in the department of electrical engineering at UET, from September 2008 until July 2010. He later obtained master's degree in electrical engineering, from the University of Iowa, Iowa City in August 2012, under the supervision of Dr. Hassan Raza. Ali's research in Dr. Raza's lab was focused on the applications of graphene and carbon nanotubes in field-effect transistors.

In August 2012, Ali moved to the University of Tennessee, Knoxville (UTK) where he enrolled in a Ph.D. program in the department of electrical engineering and computer science, under the supervision of Dr. Gong Gu. Mr. Ali's research in Dr. Gu's lab was focused on the synthesis, characterization, and applications of two-dimensional materials. During his graduate studies at UTK, Mr. Ali collaborated with electron microscopy and surface science research groups and was able to publish three first-authored papers in peer-reviewed journals.